High Intensity Focussed Ultrasound Treatment Planning for Renal Tumour Ablation

Magda Abbas

Wolfson College
University of Oxford

A thesis submitted for the degree of
Doctor of Philosophy

Trinity 2019

Abstract

The use of High Intensity Focussed Ultrasound for the thermal ablation of renal tumours provides a completely non-invasive method for treatment, which is advantageous for patients who are not eligible for surgery due to co-morbidity issues. However, clinical trials have shown variable results with challenges to the delivery of the ultrasound beam related to the intervening tissue layers. The use of patient-specific models is investigated as a means to provide a treatment planning step to aid clinicians in the choice of the transducer's position and ultrasound power for the treatment.

CT scans from patients treated in a clinical trial were segmented into bone, muscle and fat. Then patient-specific acoustic simulations were undertaken using the time domain acoustic solver software k-Wave. Patient-to-patient anatomical variability yielded differences of up to 154 W in the acoustic powers required for successful renal tumour ablation.

To find an optimal placement for the transducer, back-propagation acoustic simulations were undertaken. A virtual source was placed within the tumour with the receiver surface representing the potential transducer locations. The complex pressure received over the transducer surface was used to predict the optimal placement.

The present thesis also considers the sensitivity of the model to speed of sound variations. There was a significant impact on the focal pressure due to the relative change in speed of sound between fat and muscle. For the patient model tested there was a $> 20\%$ change in maximum pressure for variations of 4% and 7% in the speed of sound of muscle and fat respectively.

In conclusion, patient-specific acoustic modelling was successfully used to evidence the patient to patient variability in power requirements for renal tumour ablation as well as the significance of transducer placement for the individual patient. This in turn explains the significant variability in ablation outcomes achieved in clinical studies to date, and emphasizes the need for careful patient-specific treatment planning if renal ablation is to be adopted clinically.

High Intensity Focussed Ultrasound Treatment Planning for Renal Tumour Ablation

Magda Abbas

Wolfson College

University of Oxford

A thesis submitted for the degree of

Doctor of Philosophy

Trinity 2019

This thesis is dedicated to
my family
for their encouragement and support.
and to
the revolutionaries of Sudan
for their peaceful stance in the face of a brutal regime and their demand of
Freedom, Peace and Justice.

Statement of Originality

I hereby declare that this submission is my own work and to the best of my knowledge it contains no materials previously published or written by another person, or substantial proportions of work which have been accepted for the award of any other degree or diploma at the University of Oxford or any other educational institution, except where due acknowledgements is made in the thesis. Any contribution made to the research by others, with whom I have worked at the University of Oxford or elsewhere is explicitly acknowledged in this manuscript. I also declare that the intellectual content of this thesis is the product of my own work, except to the extent that assistance from others in the project's design and conception or in style, presentation and linguistic expression is acknowledged.

Magda Abbas
October 2019

Acknowledgements

I would like to express my gratitude to my supervisors. Prof. Cleveland has been extremely supportive and provided me with guidance through the difficulties in my DPhil. I have learned from him to be more precise in my work. Prof. Coussios for his guidance and helping me to look at the big picture. They have both inspired and encouraged me throughout my DPhil.

I would like to thank the members of the BUBBL lab for the support and encouragement during my time there. I would especially like to thank Dr. Michael Gray who has been a great help with advice and technical support. His help with the experiment to characterise the clinical transducer was invaluable. My thanks go to James Fisk and David Salisbury who built the platform I used in this experiment and helped me in other experimental setups.

Dr. Paul Lyon helped immeasurably by finding the relevant CT scans for the models included in the thesis without which I would not have had one. My gratitude goes to Visa Suomi who also worked on patient modelling and set up the run environment in the cluster to run the k-Wave models, and to Joseph Blackmore for his technical help. Thanks also to Cameron Smith for the discussions that cleared-up those hazy ideas. Many thanks to Daphne Cunningham and Jo Armitage for being so friendly and dealing with any administrative issues I encountered so easily.

I would like to acknowledge the support of my funding from the RCUK Digital Economy Programme Grant number EP/G036861/1 (Oxford Centre for Doctoral Training in Healthcare Innovation).

I would not have been able to finish this thesis had it not been for the help and support that I have received from my friends and family. I extend my thanks to my friends in BUBBL, in the CDT in Healthcare Innovation and in Wolfson. To Hebattalah Ibrahim for her kindness and support, for helping me stay positive and focussed, and for hosting me whenever I needed to come to Oxford. Rachel Hopkins and Estelle Beguin for the constant support in Oxford and remotely from the US. Yanting Shen and Niyati Sharma for the shared good times. To the members of the Wolfson College Choir and the Wolfson Table Tennis club for the enjoyable times free of studies. My parents for their support and patience, Sarah for hosting me when I was writing up and her help and support through that stressful time. My niece Suzanne for wakening me up daily with her beautiful smile and the joyful

time I have playing with her. Younus and Shyma for their encouragement and my nephew Sami and niece Yassamine for the joy they bring to my life.

My parents for their support and patience, Sarah for hosting me when I was writing up and her help and support through that stressful time. My niece Suzanne for wakening me up daily with her beautiful smile and the joyful time I have playing with her. Younus and Shyma for their encouragement and my nephew Sami and niece Yasmine for the joy they bring to my life and the happiness I find in their company.

Dissemination

Journal Publications

M. A. Abbas, C.-C. Coussios, and R. O. Cleveland, "Patient-Specific Models for the Retrospective Prediction of the Efficacy of HIFU Renal Tumour Ablation," (in preparation)

Conference Publications

M. A. Abbas, C.-C. Coussios, and R. O. Cleveland, "Patient Specific Simulation of HIFU Kidney Tumour Ablation," in 2018 40th Annual International Conference of the IEEE Engineering in Medicine and Biology Society (EMBC), 2018, pp. 5709–5712.

M. Abbas, C. Coussios, and R. Cleveland, "Focusing ultrasound into the kidney using 3D patient models," J. Acoust. Soc. Am., vol. 144, no. 3, pp. 1924–1925, 2018.

Abstract

The use of High Intensity Focussed Ultrasound for the thermal ablation of renal tumours provides a completely non-invasive method for treatment, which is advantageous for patients who are not eligible for surgery due to co-morbidity issues. However, clinical trials have shown variable results with challenges to the delivery of the ultrasound beam related to the intervening tissue layers. The use of patient-specific models is investigated as a means to provide a treatment planning step to aid clinicians in the choice of the transducer's position and ultrasound power for the treatment.

CT scans from patients treated in a clinical trial were segmented into bone, muscle and fat. Then patient-specific acoustic simulations were undertaken using the time domain acoustic solver software k-Wave. Patient-to-patient anatomical variability yielded differences of up to 154 W in the acoustic powers required for successful renal tumour ablation.

To find an optimal placement for the transducer, back-propagation acoustic simulations were undertaken. A virtual source was placed within the tumour with the receiver surface representing the potential transducer locations. The complex pressure received over the transducer surface was used to predict the optimal placement.

The present thesis also considers the sensitivity of the model to speed of sound variations. There was a significant impact on the focal pressure due to the relative change in speed of sound between fat and muscle. For the patient model tested there was a $> 20\%$ change in maximum pressure for variations of 4% and 7% in the speed of sound of muscle and fat respectively.

In conclusion, patient-specific acoustic modelling was successfully used to evidence the patient to patient variability in power requirements for renal tumour ablation as well as the significance of transducer placement for the individual patient. This in turn explains the significant variability in ablation outcomes achieved in clinical studies to date, and emphasizes the need for careful patient-specific treatment planning if renal ablation is to be adopted clinically.

Contents

List of Figures

List of Tables

List of Abbreviations

1D, 2D, 3D . . One-, two- or three- dimensional.

3DCRT . . . . Three dimensional conformal radiotherapy.

ARC . . . . . Advanced Research Computing.

AS . . . . . Angular Spectrum.

ASM . . . . . Angular Spectrum Method.

BPAP . . . . . Back propagated average pressure.

BPPD . . . . . Back propagated phase deviation.

CT . . . . . Computational tomography.

FDA . . . . . Food and Drug Administration.

FEM . . . . . Finite Element Modelling.

FFT . . . . . Fast Fourier transform.

FDTD . . . . . Finite-Difference Time-Domain.

HCC . . . . . Hepatocellular carcinoma.

HIFU . . . . . High intensity focussed ultrasound.

HU . . . . . Hounsfield Units.

MI . . . . . Mechanical Index.

MPI . . . . . Message Passing Interface.

MRI . . . . . Magnetic Resonance Imaging.

PML . . . . . Perfectly Matched Layer.

PPW . . . . . Points per wavelength.

PVE . . . . . Portal Vein Chemoembolisation.

PRF . . . . . Pulse Repetition Frequency.

RF . . . . . Radio Frequency.

RMSD . . . . . Root Mean Square Deviation.

SD . . . . . Standard Deviation.

TACE . . . . . Transarterial chemo-embolisation.

UCL . . . . . University College London.

USgHIFU . . . Ultrasound guided HIFU

US . . . . . United States

1 Introduction

High intensity focussed ultrasound (HIFU) is a noninvasive treatment that uses focussed ultrasound waves to create targeted well defined regions of coagulative necrosis, or lesions in tissue. It provides several advantages in terms of reduced morbidity and faster recovery times for patients. Although it has gradually gained acceptance for treatment of prostate and liver malignancies, its use for kidney ablation is still under investigation. Challenges to the treatment include the impact of the tissue layers in the propagation path of the ultrasound beam causing the defocussing of the beam and resulting in focal point fragmentation. There is an increased interest in the use of patient specific computer models to simulate the propagation of the ultrasound field within the patient to help HIFU surgeons in specifying the treatment conditions that would give the best outcome. This thesis uses patient specific computer models to guide the choice of HIFU power level and position for the transducer. It also looks at the importance of the accurate specification of the speed of sound for the soft tissue layers so that the treatment planning stage is a good representation of the treatment outcome. An overview of the layout of the thesis is as follows:

Chapter 2 is a review of the clinical trials that used HIFU for abdominal tumour ablation and highlights the challenges facing the technology. It describes

other simulation models from the literature that were devised and implemented to understand the effects of heterogeneous tissue on HIFU applications.

Chapter 3 follows with a description of the physical underpinnings of the k-Wave simulation package for acoustic and thermal simulations. Chapter 4 looks at the ability to characterise a HIFU transducer by using a pre-focal scan of a radial line across the face of the transducer. Two transducers were characterised, one a research transducer, the other a clinical transducer in an ultrasound guided HIFU (USgHIFU) system, that is used clinically at the Churchill Hospital, part of the Oxford University Hospitals NHS Trust.

Chapter 5,6 and 7 deal with the applicability of the patient specific model using k-Wave to help in the treatment planning for HIFU ablation of kidney tumours. Chapter 5 describes simulations undertaken using CT scans from 5 patients that were treated with HIFU as part of a kidney ablation clinical trial. It highlights the problems facing the treatment with lack of monitoring for ablation onset and the need for the use of patient specific transducer power levels. A method to select an optimal position for the transducer that can be used to guide the clinician for transducer placement is described in Chapter 6. The sensitivity of the model to the variation in the speed of sound is investigated in Chapter 7. A range of values are selected from the literature for muscle, fat and bone.

The final chapter, Chapter 8, gives the main conclusions for the thesis and looks at possible future improvements for the model to make it more automated and more relevant for the treatment.

The aim of this work is to ascertain whether a computational model would be able to predict the outcomes of HIFU ablation in kidney tumours. This is undertaken by using segmented CT data from patients who underwent kidney tumour ablation integrated in an ultrasound propagation model that uses the k-Wave toolbox. This patient model is then used to identify the best location to position the transducer for the treatment from a set of possible positions surrounding the patient.

In order to use the patient specific models as a treatment planning tool the pressure values used for the simulations have to be compared to the power input for

the transducer used in the treatment, therefore a calibration has to be undertaken. This calibration would enable the clinicians to use the appropriate power setting for each patient and allow them to anticipate the power level at which ablation onset would occur.

Representing the propagation path of the ultrasound beam through tissue would give the clinician a better understanding of the difficulties in achieving a complete tumour response. The ability to give guidance on transducer positioning would also help in treatment preparation. Therefore, providing a computer model that is able to characterise the effects of patient specific tissue heterogeneity would be a valuable treatment planning tool.

In summary the objectives of this thesis are:

- Characterise the transducer on the model JC200 USgHIFU clinical system.
- Retrospectively predict and understand the outcomes of a kidney ablation clinical trial by using patient specific models derived from the CT scans from 5 of the patients treated in the trial.
- Devise a method to find an optimal acoustic window for the positioning of the transducer around the patient's abdomen to treat kidney tumours.
- Analyse the "sensitivity" of the derived patient models to the change in the speed of sound for three classes of tissue: muscle, fat and bone.

2
Literature Review

The use of ultrasound as a tissue ablation technique dates back to the mid twentieth century. High Intensity Focussed Ultrasound (HIFU) was studied for its ability to create lesions in tissue in the 1940s by Lynn et al. on ex-vivo tissue samples [1]. Pioneering in-vivo work was then carried out by Fry et al [2, 3], where they induced lesions in mammalian brains. The use of ultrasound to induce hyperthermia grew in the 1980s and early 1990s [4–6]. Research widened into the investigation for the use of HIFU for tissue ablation application using higher pressures [7–10]. Focussed ultrasound is also being investigated with the use of bubbles for their mechanical effects for drug delivery [11, 12], blood brain barrier opening [13, 14] and thrombolysis [15–17] among other applications. Recently hyperthermia has been demonstrated to be effective in the delivery to tumours of drugs encapsulated within temperature-sensitive liposomes [18–21].

HIFU ablation has been tested in the clinic on various tumour types with varying degrees of success. This variation in results has prompted the exploration of the effects that heterogeneous tissue structures and patient variation has on the treatment with the need to provide more patient specific solutions. The recent advances in computer processing and the availability of structural medical images have driven this effort by encouraging the use of patient specific models for treatment planning.

2.1 Overview of Cancer Treatment Modalities

Cancer is the second largest cause of death worldwide with an estimated 9.6 million deaths in 2018. Low and middle income countries contribute to 70% of deaths from cancer, since they do not have the adequate health services to provide timely diagnosis and treatment [22]. Cancer cases in the UK averaged approximately 363 thousand annually between 2014-2016, with 163 thousand deaths recorded in 2016. The incidence rate has increased by 12% since the early 1990s, predominantly because of an increasingly ageing population [23].

Cancer is a term used to describe a set of diseases that affect multiple organs. It is characterised by the growth of abnormal cells that proliferate uncontrollably and can then invade other parts of the body through metastasis. Hanahan and Weinberg [24] identified changes in six cell physiologies as the common factors in most cancerous cell genotypes. They are: an independence in growth signals, evasion of inhibitory growth signals, evasion of programmed cell death, angiogenesis, unlimited replication, invasion and metastasis to other tissue regions. The study also highlighted the contribution of the tumour microenvironement which is composed of normal cells that are actively participating in the tumourigenesis by aiding the expression of certain hallmarks. In a subsequent work the same authors added two other hallmarks, exhibited by cancer cells, that describe the modification of cellular metabolism in order to support neoplastic activity and the evasion of destruction by the immune system [25].

Early diagnosis of cancer mostly results in successful treatment in localised easy to access cancer such as melanoma and thyroid cancer [26]. Surgical resection is the treatment of choice for localised tumours [27]. Radiotherapy can also be used on its own to treat early cancers in the skin, prostate, lung, lymph, head and neck [28].

Bigger tumours that are located near other sensitive organs create a challenge for surgical resection, and require preoperative treatments. Chemotherapy [27, 29], radiotherapy [28] or a combination of both [27, 28] are used as preoperative therapies as a means to shrink the tumour size and move it into the resectable

category and improve survival rates. Chemotherapy is also used as a postoperative treatment to ensure metastasis suppression [30].

For patients with local or locoregional disease who are not suitable for or unwilling to consent to resection, a combination of chemotherapy and radiotherapy is most commonly used. [27]. Alternative localised treatments would provide a good option for these patients. Minimally invasive techniques have been studied for localised tumour treatment, they include radio-frequency (RF) ablation and cryoablation [31–33]. However, HIFU enables a fully non-invasive treatment.

The treatment options for late stage cancer are limited and concentrate on improving quality of life and prolonging survival time. Chemotherapy is largely used to treat this group as a palliative treatment [27]. HIFU is also used clinically as a palliative treatment for bone metastases [34, 35].

2.2 Biomedical Ultrasound

Ultrasound waves have seen widespread adoption in the medical field by virtue of their use in diagnostic imaging. The therapeutic use of ultrasound has lagged behind, with the United States (US) Food and Drug Administration (FDA) giving approval for the treatment of uterine fibroids only in 2004. Within the last decade the FDA has approved the use of HIFU for prostate cancer and benign prostatic hyperplasia [36, 37], bone metastases and other musculoskeletal conditions [34, 35], uterine fibroids [38], and essential tremor [39] and tremor dominant Parkinson's disease [39, 40]. All these treatments use ultrasound to ablate targeted tissue regions. This section and the next will give an overview of the underlying principles that make ultrasound able to deliver such high energy to the target noninvasively.

2.2.1 Linear Ultrasound Propagation

Acoustic waves travel in an elastic medium as longitudinal waves in alternating compressional and rarefactional perturbations that cause local variations in the density due to the particles in the medium oscillating. It is a longitudinal wave because the movement of the particles is parallel to the propagation path of the

wave [41]. Ultrasound is defined as the range of frequencies above 20 kHz which are higher than the threshold for human hearing.

The ultrasound wave travelling in a medium can be described using a linear model if the amplitude of the wave is small [42]. The small signal model is valid when the speed of sound in the medium is much bigger than the experienced particle velocity and the fluctuation in density is smaller compared to the static density [43], with the propagation distance much smaller than the shock formation distance [44].

A small signal model is able to describe many important sound wave properties, like refraction, reflection, scattering and absorption. These are sufficient for many applications where the ultrasound wave is small and does not affect the medium properties [43].

The wave in the small signal model maintains its shape and frequency components. However, amplitude losses arise due to attenuation resulting from scattering and absorption. The rate of attenuation increases with increasing frequency and is described using an attenuation coefficient that is a power law of frequency. This makes the propagation depth for the ultrasound wave frequency dependent [45]. Thermoviscous absorption of the ultrasound waves will generate heating, which has therapeutic uses as described in section 2.3.1. The lower frequency waves will be more likely to propagate further resulting in the ability to treat tissue structures at depth [45].

2.2.2 Nonlinear Ultrasound Propagation

For higher amplitudes the effect of the wave's propagation on the media cannot be ignored and nonlinear terms become important to describe the wave propagation. Higher pressure fluctuations result in local changes in particle velocity which cause a shift in the frequency components of the signal. As the density in the compression cycle becomes much bigger than the ambient density due to the increased pressure the local particle velocity also increases. In the rarefaction cycle the reverse occurs with the local velocity decreasing with the density. For a progressive plane wave

this can be described by the following equation:

$$v = c_0 + (1 + \frac{B}{2A})u \tag{2.1}$$

where v is the phase velocity of the acoustic wave, u the particle velocity, $\frac{B}{A}$ is the parameter of nonlinearity and $1 + \frac{B}{2A}$ represents the coefficient of nonlinearity β [42].

The difference in velocity for the compression and rarefaction cycles results in the distortion of the waveform, which translates into a shift in the energy from the fundamental frequency into the harmonic components [42].

2.3 HIFU as a Therapeutic Modality

Two main effects define the use of HIFU for therapeutic applications, thermal and mechanical (cavitation activity).

Experiments conducted across a range of intensity levels and time durations found a difference in the type of lesions created. In experiments by Frizzell using a frequency of 3 MHz to find intensity thresholds for lesion creation in cat liver a change in the linear graph of intensity vs exposure time was noted at peak intensity values above 1000 W/cm^2 for exposure durations < 0.1 s. This change was attributed to a shift in the damage mechanisms towards a cavitation dominated mechanism, and was corroborated through histological evidence. The lesions created at higher intensities at these lower exposure durations showed irregular boundaries, destructive damage amounting to complete homogenisation of the tissue. Below 1000 W/cm^2 the lesions had smooth boundaries and were positioned in the centre of the focal region [46].

Fry et al. used a range of intensity values and time durations to create lesions in cat brain and observed different manifestation of damage, either thermal or mechanical according to the exposure parameters [47].

Effects of cavitation in enhanced heating was shown by Hynynen [48], who observed increased heating that was correlated with the onset of subharmonic signals detected by a passive detector. This was followed by the temperature time relationship deviating from linear theory. The emphasis for the use of focussed

ultrasound for therapy was to try to avoid cavitation by optimising the exposure conditions to induce only thermal effects [48].

Holt and Roy tested the effects of enhanced heating with cavitation on a tissue mimicking phantom using 0.5 -10 s exposure times and multiple pressures. A set of thermocouples recorded the increase in temperature rise above the anticipated values from the linear model. The onset of this temperature increase coincided with subharmonic and broadband signals indicating that it was driven by cavitation. They argued for the use of controlled cavitation as a means to enhance the heating from HIFU and improve the efficacy of the treatment [49].

2.3.1 Thermal effects

The mechanical energy of the focussed acoustic wave is converted to heat, through thermoviscous absorption and if it's applied for long enough the temperature will increase until the cells are killed through thermal necrosis. A tightly focussed beam can thus result in a well defined lesion of necrotic tissue leaving the surrounding tissue unaffected. The size of the lesion depends on the dimensions of the transducer and frequency of the acoustic wave, but in HIFU it normally ranges from 1-3 mm laterally and 8-15 mm axially [50]. The rate of heating will depend on the acoustic intensity, frequency and type of tissue being heated. The mechanism of cell death will depend on the temperature achieved and the duration for which it is maintained. Cell death by coagulative necrosis occurs in as little as 1 second if the temperature achieved is above 56°C [50].

The relationship of attenuation and absorption as a power law of frequency means that higher frequency results in higher attenuation and absorption of the ultrasound wave by tissue. Therefore a balance in choosing the frequency has to be found between focal depth and rate of heating achieved [51]. Using higher frequencies could result in rapid heating at the focal point but reduced penetration depth [52].

2.3.2 Mechanical Effects

The mechanical effects that can occur from focussed ultrasound are predominately due to cavitation. High rarefactional pressures in the acoustic wave can form cavities that draw in gas and vapour to create bubbles. This acoustically induced nucleation is then followed by the bubbles created oscillating in the acoustic field in what is termed acoustic cavitation [49, 53, 54].

Cavitation can be divided into two broad categories: non-inertial cavitation and inertial cavitation [51]. Non-inertial cavitation is the oscillation of the bubble about an equilibrium radius. The mechanical movement of the bubble is defined by the compressibility of the gas phase. The associated physical effects include sound scattering, subharmonic generation [55], microstreaming [56] and heating [57, 58].

Inertial cavitation arises when the rarefactional phase of the ultrasound cycle grows the bubble unstably to a size that is mostly filled with vapour with a small amount of gas. The collapse that follows in the compressional cycle is dominated by the inertia of the surrounding fluid and can result in supersonic bubble wall velocities [51]. The associated physical phenomena include microstreaming, fluid jetting near boundaries, light generation, sonoluminescence, and sonochemistry [59]. The high acceleration of the bubble wall results in broadband acoustic emissions [49].

Enhanced heating caused by cavitation was noted by groups working on HIFU ablation and has been studied as a promising mechanism that could increase localised focal heating improving the efficacy of the HIFU treatment [49, 51]. The thermal enhancement induced by cavitation has been attributed mainly to two effects with varying levels of contribution: the absorption of secondary emissions radiated by inertial bubble collapse and viscous damping from bubble oscillations. [57].

The mechanical effects associated with cavitation such as microstreaming and fluid jetting near boundaries have been studied for use in applications including drug delivery [60], blood brain barrier opening [61] and sonothrombolysis [15–17]. Cavitation is the main mechanism for stone fragmentation in shock wave lithotripsy [62, 63].

2.3.3 Advantages and Limitations of HIFU Therapy

The advantages of HIFU as a treatment modality are: it is non-invasive and will therefore provide faster recovery after its application; treatment is localised and non-ionising, targeting the required area and minimising damage to surrounding healthy tissue; and the treatment can be repeated, since there is no tissue tolerance level to repeated acoustic exposure.

HIFU also exhibits several limitations. Ablative transducers typically exhibit a small focal region, which means that a treatment for a standard tumour of 3 cm^3 would take hours to complete [9]. The use of enhanced heating using cavitation could result in reflections from bubbles which would increase the acoustic intensity pre-focally resulting in the migration of the cloud towards the transducer. Lesions of unpredictable shape could arise from that [53, 64].

Treating in or behind air filled organs such as the lungs and bowels is not possible due to the reflection of the acoustic energy at the air interface. Bone also presents a challenge for HIFU due to its high acoustic attenuation and beam distortion, due to the nearly two fold increase in sound speed. However, distortion from the skull has been overcome by phase correction and ultrasound has been delivered to the brain [8]. For single element transducers aberration correction using acoustic lenses is being studied [65].

In order to treat tumours in the upper abdomen the ultrasound beam passes through the rib cage, resulting in burning of the tissue at the rib locations [66]. Multi-element arrays have been investigated to reduce this challenge by shutting down the elements that are in front of the ribs [67]. The use of acoustic lens methods for transcostal ablation treatments using single element transducers would require building a lens that is configured to remain stationary relative to the patient's ribs instead of relative to the transducer, because of the requirement to scan the transducer to cover the tumour volume.

Deep targets are difficult to treat even if only behind soft tissue layers. Aberration in the sound field has also been observed due to the refraction resulting from different speed of sound values of muscle and fat layers. This aberration was also noted

in ultrasound image distortion [68–70]. The aberration in focussed ultrasound applications results in a shift in the focal point and reduction in the acoustic pressure which changes depending on aperture size and frequency used [71, 72]. Experiments with fat layers showed that there is a significant change in the focal region due to attenuation and aberration from fat layers [73]. This is particularly challenging when treating the kidney due to the layer of fat, typically 2-4 cm deep, surrounding it. HIFU kidney ablation trials have shown evidence of necrosis within this peri-nephric fat layer [9, 74].

Figure 2.1 shows a sketch of a HIFU transducer used to target a kidney tumour. The sketch shows that the HIFU beam has to pass through multiple tissue layers before arriving at the target. These layers vary in thickness and structure from one patient to another creating challenges for the reproducibility of HIFU treatment outcomes.

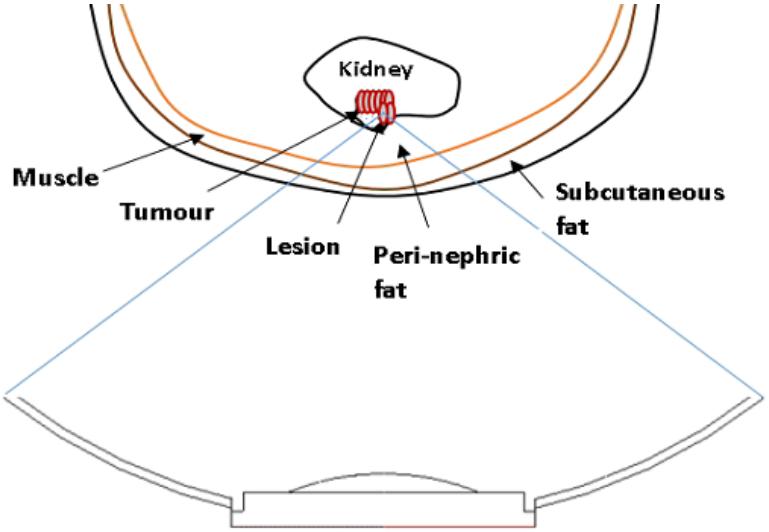

Figure 2.1: Sketch of HIFU Kidney Ablation, showing the different tissue layers in the path of the ultrasound beam.

Another challenge is motion due to breathing. The effect of lung movement was reduced in some trials by the use of endotracheal intubation, allowing single lung ventilation by isolating the lung at the side of the treatment [75, 76]. High frequency jet ventilation was also used as an anesthetic technique to minimise respiratory movement [18].

2.4 Clinical Uses of HIFU for Tumour Ablation

HIFU has found clinical success in the treatment of many benign and cancerous tumours as well as some neurological disorders. It has gained FDA approval for use in the treatment of prostate cancer and benign prostatic hyperplasia, uterine fibroids and essential tremor. It is also used for pain reduction in bone metastasis. Furthermore, it has gained wider approval outside the US with increased application in soft tumour treatment, figure 2.2 shows the regulatory approval for HIFU treatments in oncology in the United States.

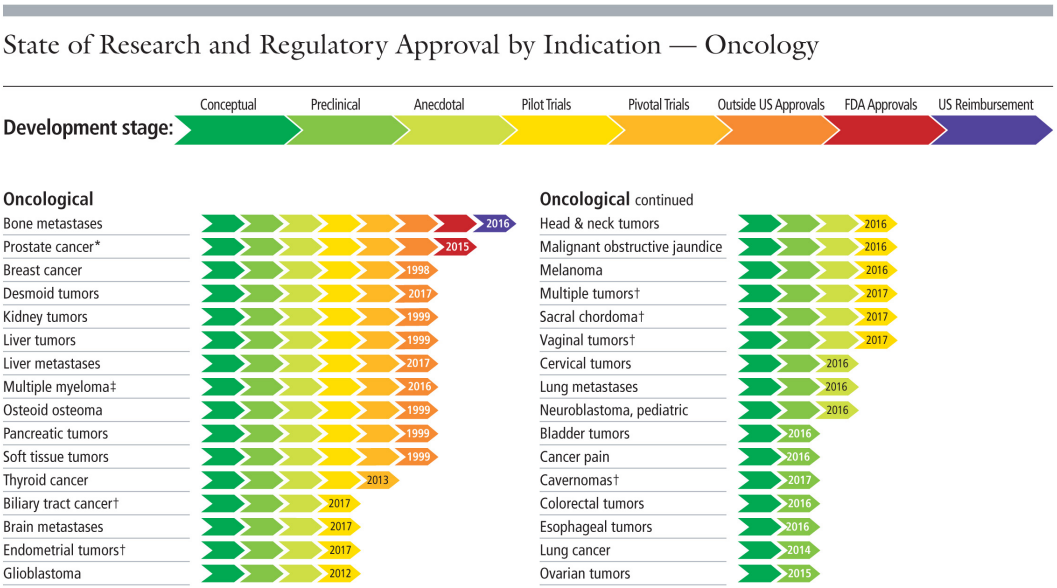

Figure 2.2: Regulatory approval in the United States for Oncology Applications of HIFU, from the Focused Ultrasound Foundation website [77]

2.4.1 Clinical Trials for Abdominal Tumour Ablation

Many clinical trials have been conducted in the use of HIFU for benign and malignant tumours. Most these trials were conducted in China with the majority published in Chinese [78]. Luo et al. and Wu et al. collated and reported many in English with an analysis of the efficacy of HIFU [66, 78]. Luo et al. reviewed and analysed clinical trials conducted in China from 1998 to 2013. 75 trials were included, with 833 cases of benign tumours and 4559 cases of malignant tumours [78]. The data

from trials for the use of HIFU for uterine fibroids, ectopic pregnancy and chyluria show no significant difference from the outcomes of surgery.

The cases included for liver cancer were 2296. For resectable tumours surgery was found to provide a significantly higher rate of complete response than HIFU combined with 3-dimensional conformal radiotherapy (3DCRT), as well as higher 5 year survival rates of 82.4% compared to 58.8%.

In advanced liver cancer, HIFU was found to improve the one year survival rate compared to supportive care from 3.6% to 50.0%. It was found to have similar survival rates to radio-frequency ablation and transarterial chemoembolisation (TACE).

The response rate differed among trials comparing the use of TACE alone vs in combination with HIFU, with one trial showing significant increase in survival rate when adding HIFU and another not. When used to manage portal vein tumour thrombosis (PVTT), the combination of HIFU and TACE improved the response rate when compared to TACE alone. HIFU increased the response rate achieved in liver cancer and PVTT when added after portal vein chemoembolisation (PVE) following TACE.

The use of HIFU in pancreatic cancer was found to increase survival rates compared to supportive care. Luo et al report clinical trials comparing the combination therapy of HIFU with chemotherapy, and with 3DCRT to the two treatments on their own. There was no significant increase in the response rates, however there was an increase in the clinical beneficial responses (CBR), used here to describe life quality indicators such as pain relief. This seems to contradict another trial reported within the review which found that HIFU plus chemotherapy had a higher response rate than chemotherapy alone. They also report that trials looking at HIFU's use in gastrointestinal cancers show disagreement. This highlights the fact that HIFU treatments are very operator and patient specific.

Another review to look at results of the treatment of pancreatic tumours using ablation techniques was conducted by Saccomandi et al [33]. The results of clinical trials for HIFU treatment were included for 17 studies with 581 patients mostly suffering from late stage pancreatic cancer. In 9 studies a post procedural evaluation

using CT, MRI and in one study post-operative colour Doppler was used. Only 6 trials reported a quantification of the tumour reduction for 120 patients. A complete reduction occurred in 17 cases, 84 cases experienced more than 75% reduction, 13 cases had a reduction between 50-75%, 6 cases had less than 50% reduction in tumour size. Pain reduction was also assessed in 9 of the studies with 123 out of 148 patients experiencing either a complete or partial (75-100%) reduction in cancer induced pain. Complications from HIFU treatment were reported in 280 cases, 45 of them were major including 35 cases of vertebral necrosis. For the minor injuries cases of first and second degree burns were the most frequently reported.

As mentioned in the review by Luo et al [78] HIFU has been tested as a treatment option for patients with hepatocellular carcinoma (HCC). More than 80% of HCC patients are unfit for surgical intervention, because of the presence of advanced cirrhosis. Therefore, minimally invasive treatments would be beneficial as an alternative [79]. Wu et al conducted a trial on 55 patients with HCC using the USgHIFU JC model HAIFU System [80]. Of these patients 26 received only HIFU during the trial, however 21 had previously received TACE. The other 29 patients received TACE two to four weeks before HIFU. HIFU treatment was repeated two or three times in 19 patients since imaging showed partial viable tumour. Rib sections overlaying the target were resected in 14 patients before the second HIFU ablation. During the follow-up period the tumour disappeared in 2 patients, reduced in size in 50, was stable in 2 and increased in size in 1.

Another trial to look at the use of HIFU in combination with TACE for liver tumours found that it was more effective than TACE alone. The survival time for the combination group was 57 months compared to 36 months in the TACE only group [81].

The ability of MRI to determine the extent of HIFU ablation in liver was tested by Leslie et al [82]. A portion of the tumour was ablated, then surgically resected to confirm the extent of ablation using histology. Their study highlights the difficulty found in predicting the size of the ablated tumour section during the HIFU treatment.

The MRI was able to detect ablation in 4 out of 6 patients [82]. In another bigger trial radiological evidence showed 93% ablation in 27 out of 29 patients [76].

HIFU ablation was also tested for its use as a bridging therapy by Chok et al [83], where it is used to sustain patients, who are not treatable with TACE, when waiting for liver transplants. HIFU was found to be successful in increasing the percentage of patients receiving bridging therapy from 39.2% to 80.4% [83].

The use of HIFU ablation for renal tumours will be considered in the following section.

2.4.2 HIFU Ablation for Renal Tumour Treatment

More than half of kidney tumours are discovered incidentally and are asymptomatic [84, 85]. Analysis of kidney tumour diagnosis found that between 1993 and 2003 there was an increase in stage I disease and reduction in stage II, III and IV disease [86]. The size of tumours detected also decreased and the results show increased relative survival [86]. Surgery is the standard treatment through partial nephrectomy or radical nephrectomy [87]. However it sometimes results in patient morbidity [87]. Since there are higher rates of kidney tumours in older patients it would be desirable to have alternative noninvasive treatments.

For use in the ablation of renal tumours HIFU has to provide an attractive alternative not only to surgery but also to minimally invasive techniques such as RF ablation, cryoablation and microwave ablation. The minimally invasive techniques are an option for the treatment of small tumours ≤ 3 cm for patients who are not good candidates for surgery due to frailty, solitary kidney, compromised renal function or bilateral tumours. [88]. As well as for patients who are undergoing treatments for other cancers. [32]. The effectiveness of RF ablation was found to be very tumour size dependent [89], whereas the tumour size was not significant for cryoablation and microwave ablation [32, 89]. Major complications have been reported for treatments using RF ablation [89, 90], cryoablation [32] and microwave ablation [89].

The use of HIFU for renal tumour ablation has had considerable interest [9, 91, 92]. A review of the first trials of HIFU for renal tumour ablation undertaken on a few patients indicated variable levels of success [93]. Wu et al [91, 93] used a USgHIFU system to treat 13 patients with renal cell carcinoma, of which one had metastasised colon cancer. Of the patients 10 had advanced stage carcinoma and were treated for palliative care. The other 3 had organ confined disease. Epidural anesthesia was used for 6 patients and 7 had general anesthesia. In 10 of 13 patients doppler sonography showed a decrease in blood supply to the tumour after HIFU treatment. Post operative imaging showed reduction in tumour size. Haematuria stopped in 7 out of 8 patients. Pain resolved in 9 out of 10 patients, but since this was not a blind trial it could be a result of placebo. Two patients with inoperable tumours because of proximity to the abdominal aorta had their tumours sufficiently reduced in size after HIFU and radical nephrectomy was performed after 8 and 11 months. In patients with lung metastasis there was neither an increase nor a decrease in the metastasis. However, the treatment time was long with a median of 5.4 hours (1.5-9 hours) [91].

In further trials conducted using an USgHIFU system Illing et al assessed the efficacy of HIFU ablation on 6 patients with renal tumours [92]. MRI was used to test for evidence of ablation 12 days post treatment with lesions detected in 4 out of 6 patients. Histological assessment showed ablation in 1 out of 4 patients. Skin toxicity and subcutaneous oedema occurred in some patients [92]. Ritchie et al conducted a trial on 15 patients with renal tumours and followed the outcomes up to 3 years after HIFU treatment [9]. Oncological outcomes were determined using contrast-enhanced MRI at 12 days, 6 months, 9 months and then yearly. Fourteen patients completed assessment to 6 months, however 4 of these had enhancement in imaging and underwent alternative therapy. Three had partial nephrectomy which showed no histological evidence of ablation. The fourth underwent RF ablation. For the remaining 10 patients imaging showed a mean decrease in tumour area of 30% in the follow-up period. Central loss of enhancement was observed in all. The 15^{th} patient on the trial had surgery due to persistent enhancement and no evidence

of ablation was found in the histology samples [9]. The evidence of ablation was through imaging in this trial, which did not show accuracy in determining the efficacy of the treatment. To provide a comparison to the standard of care another trial that included the surgical resection of the treated tumour was conducted next [75]. The trial treated 10 patients with renal tumours after which the tumours were resected. The results showed 90-99% ablation in 3 patients, 50-90% ablation in 3 patients and minimal or no ablation in 4 patients.

These trials on kidney tumour ablation demonstrate that HIFU ablation resulted in minimal impact on renal function. However, the efficacy of tumour ablation was variable. The challenges that were raised for the treatment are related to the presence of a layer of peri-nephric fat that showed signs of ablation resulting from pre-focal heating [75].

The results of all these trials show that HIFU can be effective for use in the ablation of tumours, however there is a big variation in the response rate. It highlights the challenges of delivering HIFU to deep tumours through heterogeneous tissue. There are also variations in the implementation methodology. There is no way to make a direct comparison of treatment methodologies. This shows that since HIFU is still an experimental treatment there are no standard rules on application. It highlights the need for better treatment planning and understanding of the effects of the intervening anatomy on the treatment.

2.5 Simulation of Ultrasound in Heterogeneous Tissue Models

The impact of tissue heterogeneity on the ultrasound beam and its result on the focal pressure and its location has been considered in a number of studies using simple geometries and progressing to full three-dimensional (3D) simulations based on patient geometries. Fan and Hynynen [71] built a two-dimensional (2D) model that represented the ultrasound propagation through heterogeneous media, as a layered medium where each interface acted as a secondary radiating source taking into consideration the reflection and refraction of the wave at that interface. The

simulations were compared with experimental measurements using polyethylene sheets of different thickness. The results showed a shift in the focus location as the angle of the transducer with the sheet was increased. The shift was up to 6 mm laterally for an angle of 60°, which the authors concluded would result in unacceptable uncertainty in delivery of sharply focused fields [71]. The same authors built another simulation model and set of experiments using a curved layer with a shift in the transducer's position laterally away from the centre axis of the curved layer [94]. Simulations were compared with models of water-(curved)polyethylene-water, water-polyethylene-caster oil-polyethylene-water and resulted in shifts in the focal point and a reduction in pressure as the transducer's centre point was moved laterally away from the centre axis of the curved phantom. The curved polyethylene layer generated the maximum shift when using a transducer with a radius of curvature of 350 mm and a diameter 70 mm. The polyethylene layer was a half circle with an inner radius of 30 mm and an outer diameter of 50 mm. The shift in the location of the focus was 11 mm when the transducer was moved laterally by 15 mm [94].

The previous models and experiments were based on simple geometric shapes that did not convey the complexity of the tissue interface in the human body. Mast et al undertook 2D simulations of the abdominal wall using an anatomically realistic structure that was derived from a cross section of an abdominal wall specimen [95]. The cross section was stained and scanned to give the fat, muscle and connective tissue components. Simulations and experiments used plane wave propagation to determine the aberration resulting in the transmitted wave. Amplitude fluctuations and time shift aberrations were detected in the experiment and finite-difference time-domain (FDTD) simulations undertaken.

Liu et al used patient derived models in order to address focal beam distortion in the treatment of uterine fibroids [72]. Simulations using the MRI image were conducted to check the effect of tissue heterogeneity. To demonstrate patient variability, 4 patients were selected with fibroids 4-7 cm in diameter with 1-3 cm thick superficial fatty layers. MR images were processed to increase contrast

and reduce noise at layer interfaces which enabled the use of edge detection for segmentation. The different tissues were then registered by the operator and reconstructed into a 3D mesh. Phase correction on each element of a phased array was simulated as a means to restore the beam pattern. The results showed that tissue heterogeneity has the ability to distort the focal pattern by shifting the focal point and increasing the side-lobe levels. The tilt angle of the array also made a difference in the obtained peak intensity and side-lobe levels. Higher frequency beams suffered more distortion from tissue inhomogeneity than lower frequency ones [72].

Other groups have looked at treatment planning strategies to improve the delivery of ultrasound to the target location. McGough et al developed a planning tool for phased arrays that used geometric and thermal optimisation to select the appropriate elements and power levels for the treatment [96]. Patient 3D geometry was extracted from a CT scan. Then ray tracing was used to define a 'cone of entry' that specifies the optimal acoustic windows, a path of energy that would avoid bone and air pockets. The optimisation routine searches through possible orientations of the array choosing positions that maximise the surface area, reflected in the number of useful elements. The driving signal for the selected elements is then calculated to obtain the required temperature distribution [97]. Thermal and acoustic simulations were undertaken afterwards to assess the success of the optimisation in obtaining the required pressure and thermal outcomes [96]. This work did not look at the beam refraction in soft tissue interfaces, since it assumed a homogeneous medium for the acoustic and thermal simulations [96].

White et al [98] tested the effect the change in transducer placement had on the focal field. Five ex-vivo bovine tissue samples were placed between a HIFU transducer and a hydrophone. The focal plane was scanned for pre-determined locations of the HIFU transducer. A comparison of the energy within a focal zone compared to the scan area was made for each position and sample [98].

Paulides et al presented an overview of the techniques used for hyperthermia and the available planning software [99]. The review highlights the requirement to increase the segmentation speed for CT/MRI data, the need to have reliable

and accurate acoustic properties for ultrasound simulations, and more accurate parameters for thermal simulation techniques. It lists ultrasound simulation methods that can be used for treatment planning, and points out that accurate full-wave ultrasound simulations incorporating nonlinearity and the effects of heterogeneity on the ultrasound field are computationally intensive.

Computer models can provide a means to analyse the effects of tissue heterogeneity on HIFU aberration. A recent study used the k-Wave simulation toolbox to test for the effects of refraction due to heterogeneous media on the HIFU focal volume in the kidney [100]. Nonlinear simulations were undertaken using three segmented CT scans of different sized patients with varying thickness of subcutaneous and peri-nephric fat. The results showed that refraction had a significant effect on the shape of the focal area and the temperature elevation reached. The effects were most pronounced in the patient with the thickest fat layers.

Gray et al [101] used a treatment planning model to predict the power required for hyperthermia mediated drug delivery in liver tumours as part of a clinical trial. The patient geometry for tissue surrounding the tumour was extracted from CT and MRI data and then approximated to simpler geometric forms to reduce processing time requirement. The acoustic and thermal simulations were performed using the PZFlex finite-difference time domain (FDTD) modelling software. The volumetric temperature rise was calculated by superposing the thermal profile obtained at single focussed ultrasound positions to cover the 3D volume. The model was implemented on 10 patients of whom 5 had already been treated with a thermocouple placed in the tumour for real-time temperature monitoring. The model predicted the power required to reach the drug release temperature threshold for subsequent treatments based on the data from the previously treated patients. The mean difference of model-predicted power and actual power to achieve hyperthermia mediated drug delivery was -0.1 W.

The k-Wave toolbox was also used by Grisey et al [102] to compare simulation results of HIFU delivery through tissue layers to experimental data. HIFU was propagated through excised rabbit tissue composed of skin, subcutaneous fat and

muscle placed in a holder with cooling liquid. The pressure was recorded using a hydrophone placed at the focal plane in water. The simulations were conducted using a three layer configuration of cooling liquid, fat/muscle combined layer, and water. The results obtained from the simulations showed a maximum pressure difference of $< 6\%$ for 60% of the 55 measurements. They also tested the effect of the tissue layer curvature on the resulting pressure finding a decrease in pressure and increase in the focal region size with increased curvature [102].

2.6 Gap in Knowledge

The above literature review shows that HIFU has considerable potential as a non-invasive technique for tissue ablation, with wide uptake in several oncological and benign indications, however, the variability in ablation efficacy has thus far prevented its application to the treatment of renal cancers. This variability appears to be caused by considerable variations across patients in peri-nephric fat thickness and other tissue layers, resulting in high sensitivity to transducer positioning and exposure parameters. Together, these challenges offer a unique opportunity to use patient-specific modelling to both explain the results of previous unsuccessful ablation trials, and improve the outcomes for future patients. Building on several decades of work that developed and validated HIFU propagation models through human tissue, the present thesis will consider the potential benefits of using full-3D patient-specific modelling for treatment planning in thermal ablation for renal tumours.

3 The Computer Model

In order to provide a patient specific model for ultrasound treatment planning a suitable computational model has to be chosen to compute the acoustic wave propagation within a 3D heterogeneous tissue structure. This tissue structure was derived from the patient's CT scan. The simulation was then run on the University of Oxford's Advanced Research Computing (ARC) Cluster.

3.1 Simulation of the HIFU Field

The simulations were undertaken using an open source Matlab toolbox called k-Wave, developed by Brad Treeby and Ben Cox at University College London (UCL) [103]. The k-Wave toolbox uses a time-domain simulation of the propagation of acoustic waves in 1D, 2D or 3D. It is based on a set of first order partial differential equations that describe nonlinear sound propagation within heterogeneous media and incorporate power law absorption. The equations are discretised using a k-space pseudospectral method to reduce the number of points required per wavelength, compared to finite-difference time-domain (FDTD) and finite element modelling (FEM) approaches [103]. This enables the simulation of large 3D domains of hundreds of wavelengths in each direction using computational resources available to the research group. Another advantage of k-Wave is the availability of a C++

implementation to run on computer clusters. It is well tested and is updated by the authors who regularly publish improvements and methods to manage limitations. Support is also available through a growing online community.

The underlying equations of fluid dynamics are used, with assumptions of an isotropic, inviscid medium with no net flow within it. Loss from acoustic absorption is modelled using an energy loss term, described later. The mass conservation and conservation of momentum equations, for an isotropic, inhomogeneous and inviscid fluid can be expressed as:

$$\frac{\partial \rho}{\partial t} + \nabla.(\rho_0 \mathbf{u}) = -\nabla.(\rho \mathbf{u}) \tag{3.1}$$

$$\rho_0 \frac{\partial \mathbf{u}}{\partial t} + \nabla P = -\rho \frac{\partial \mathbf{u}}{\partial t} - \frac{1}{2}\rho_0 \nabla(u^2) \tag{3.2}$$

Where ρ is the fluctuation in density due to the acoustic disturbance, ρ_0 is the ambient density, $\mathbf{u}$ is the particle velocity, $u^2 = \mathbf{u}.\mathbf{u}$ and P is the total pressure. The equations account for acoustic propagation up to second order in terms of acoustic variables. Higher order terms are discarded, since second order terms provide a sufficient representation of the nonlinear effects present in HIFU [104].

The substitution of the linearised equations allows equations 3.1 and 3.2 to be expressed as [104]:

$$\frac{\partial \rho}{\partial t} = -(2\rho + \rho_0)\nabla.\mathbf{u} - \mathbf{u}.\nabla\rho_0 \tag{3.3}$$

$$\frac{\partial \mathbf{u}}{\partial t} = -\frac{1}{\rho_0}\nabla p \tag{3.4}$$

where terms with the Lagrangian density have been dropped, as they are not relevant for cumulative nonlinearity effects [44]. The Lagrangian density represents the difference in the kinetic energy in the wave to its potential energy.

The relationship of density and pressure can be expressed using the equation of state with terms up to 2nd order included [104]:

$$p = c_0^2(\rho + \mathbf{d}.\nabla\rho_0 + \frac{B}{2A}\frac{\rho^2}{\rho_0} - L\rho) \tag{3.5}$$

Where c_0 is the speed of sound, $\mathbf{d}$ is the particle displacement vector, with the term accounting for heterogeneities in the ambient density, B/A is the nonlinearity

parameter, which represents the material nonlinearity, and L is a loss operator used to model power law absorption.

The absorption for most soft tissue is assumed to follow a power law relationship of the form [105]:

$$\alpha = \alpha_0 w^y \tag{3.6}$$

where α is the absorption coefficient in Np, α_0 is the power law prefactor in Np(rad/s)$^{-y}$ m^{-1}, with y as the power law exponent, and w is the angular frequency in rad/s.

The operator L that accounts for absorption is defined by Treeby et al [105] as:

$$L = \tau \frac{\partial}{\partial t}(-\nabla^2)^{\frac{y}{2}-1} + \eta(-\nabla^2)^{\frac{y+1}{2}-1} \tag{3.7}$$

τ and η are absorption and dispersion proportionality coefficients. $\tau = -2\alpha_0 c_0^{(y-1)}$ and $\eta = 2\alpha_0 c_0^y \tan(\pi y/2)$.

The pressure source can be modelled as a mass source S_M, which represents the time rate of change of the input mass per unit volume (kg m^{-3} s^{-1}). It is added to the mass conservation equation [106]:

$$\frac{\partial \rho}{\partial t} = -(2\rho + \rho_0)\nabla.\mathbf{u} - \mathbf{u}.\nabla\rho_0 + S_M \tag{3.8}$$

To solve the coupled acoustic equations 3.3 to 3.5 outlined above k-Wave uses a k-space pseudospectral method [104]. Spatial gradients are calculated using the Fourier collocation method, which uses the Fourier series to interpolate between all the collocation points simultaneously and multiply its coefficients by the corresponding wave number to obtain the gradient. There are two advantages to this: first, the Fourier coefficients can be calculated using the fast Fourier transform (FFT), which allows for a computationally efficient implementation of the transform. Second, the basis functions are sinusoidal thus, theoretically, requiring only two grid points per wavelength for an accurate representation. This reduces grid size requirements which is critical to the simulations to be done here which have domains that are hundreds of wavelengths in all 3 directions.

To calculate the derivative in the time domain k-Wave uses a time difference calculation employing a k-space method [103]. The k-space methods aim to relax the limitation on the size of the time step imposed by the need to reduce errors in the numerical solutions of finite difference techniques. Replacing Δt with $\Delta t\ \mathrm{sinc}(c_0 k \Delta t/2)$ provides a solution that is guaranteed to be free from numerical dispersion in a homogeneous medium. The k-space operator can then be defined as [106]:

$$\kappa = \mathrm{sinc}(c_{ref} k \Delta t/2) \tag{3.9}$$

where c_{ref} is a scalar reference sound speed and k is a scalar wavenumber. For a 3D simulation $k = \sqrt{k_x^2 + k_y^2 + k_z^2}$. k_x, k_y and k_z are the wavenumbers in the x, y and z directions respectively.

In a homogeneous medium the solution using the k-space method can be unconditionally stable (and exact) by choosing $c_{ref} = c_0$, where c_0 is the spread of sound in the medium. However, for a heterogeneous medium there are two possibilities for choosing c_{ref}. If $c_{ref}/c_0 > 1$ the solution will be unconditionally stable, but phase errors will accumulate. With larger phase errors for larger values of c_{ref}/c_0. If $c_{ref}/c_0 < 1$ phase errors are limited, however stability is conditional on choosing a small time step, bounded by [106]:

$$\Delta t \leq \frac{2}{c_{ref} k_{max}} sin^{-1}\left(\frac{c_{ref}}{c_0}\right) \tag{3.10}$$

The Courant-Friedrichs-Lewy (CFL) number is used to describe the required time step used in the k-Wave simulation. The CFL is a dimensionless number defined as the ratio of the distance a signal can travel in one time step to the grid size.

$$CFL = \frac{c_0 \Delta t}{\Delta x} \tag{3.11}$$

Therefore, in order to choose a time step that is bounded by equation 3.10, the CFL has to be bounded by [106]:

$$CFL \leq \frac{2}{\pi}\left(\frac{c_0}{c_{ref}}\right) sin^{-1}\left(\frac{c_{ref}}{c_0}\right) \tag{3.12}$$

This means that a smaller CFL number is better for ensuring stability in a heterogeneous medium, however the computational requirements will also increase. This is because the time step of the k-Wave simulation is set from the following relationship with the CFL number:

$$\Delta t = \frac{CFL\Delta x}{c_{max}} \tag{3.13}$$

where c_{max} is the maximum sound speed defined in the medium.

A perfectly matched layer (PML) is applied to the boundary of the grid surrounding the medium [104, 107], in order to attenuate the waves at the edge of the grid to reduce the effects of wave wrapping resulting from the use of the FFT. The PML's absorption is anisotropic as it is defined such that only components of the wave that are normal to the boundary are absorbed within the PML [104]. Within k-Wave the size and absorption coefficient of the PML are adjustable through the optional input parameters `PMLAlpha` and `PMLSize` [106]. Using the default values for `PMLAlpha` = 2 and `PMLSize` = 10, the transmission was found to be reduced by 84 dB and the reflection coefficient was reduced by 65 dB [106].

3.1.1 Accuracy of k-space pseudo-spectral techniques

The accuracy of the k-space methods can be affected by phase errors, finite bandwidth and staircasing errors.

The use of a finite difference time step introduces phase errors that can be compensated for by the use of the k-space operator κ. However, using κ can only ensure exact simulation in a homogeneous medium, by choosing $c_{ref} = c_0$. For a heterogeneous medium the k-space operator will only correct for one sound speed. Therefore, other regions of the medium will experience dispersion errors. This may not be an issue in a weakly heterogeneous medium, since the accumulated errors may be within an acceptable value. But, in a medium where there are big contrasts in sound speed the choice of the reference sound speed is important and has to be considered along with the stability conditions [108]. If the reference sound speed

is double the sound speed in the medium the phase error was found to increase to 3% after 50 wavelengths of propagation [104].

The Fourier collocation method used to compute the spatial derivatives by fitting a Fourier series to all the collocation points simultaneously uses a finite number of coefficients, resulting in a band-limited representation. This band-limited function is called the band-limited interpolant (BLI). The gradient of the BLI is what is calculated by pseudospectral methods. This representation is accurate for periodic fields that vary sufficiently smoothly between collocation points. For discontinuous pressure and medium properties the limited bandwidth of the representation can result in Gibbs like phenomena. Smoothing windows can be used to filter the BLI to remove the oscillations between the discrete points, which could result in a closer representation of the pressure distribution [104, 108].

The uniform grid used results in the surfaces that are not aligned with the grid being represented by a staircase. The staircasing results in errors that depend on the extent to which the staircased geometry diverges from the ideal geometry. The errors arise from both the source and the media defined on the discrete grid. The effect of the grid resolution on source discretisation were shown for a single element focussed transducer represented using a bowl by Martin et al [109]. The lower resolution grids resulted in the source surface being further away from the position of the ideal bowl. This had an effect on the shape of the generated field especially in the near field, with the pressure profile not following the normal oscillatory shape. However, the focal shape and main lobes were captured well. Also, since the staircase shape results in a lower density of grid points in the diagonal direction compared to the points on axis a lower acoustic pressure is generated at the diagonal direction. A line at angle 45° has fewer points per unit length than that aligned with the grid. This results in the pressure generated being smaller by $\sqrt{2}$ [109].The authors propose multiplying the source pressure at the diagonal grid points by a scaling factor as a correction method [109]. Results highlighting the effects of source staircasing will be discussed when referring to the simulation of a single element transducer in section 3.4.

Staircasing errors also occur at the acoustic interfaces. Robertson et al [110] quantified the effect of staircasing errors across a highly heterogeneous medium of skull and brain tissue in time reversal simulations. They found that 6 PPW would be required to achieve 95% reconstruction of pressure amplitude (<10% error in intensity).

3.2 Patient Specific 3D Medium Structure

Abdominal patient CT scans are used to derive 3D heterogeneous media used in the k-Wave simulation model. First a Matlab script was used to segment each CT slice based on the intensity threshold of the image into bone, non-fatty tissue and fat. The raw CT scan for one of the patients recruited on a kidney ablation trial is shown in figure 3.1(a). The automatic segmentation result which has segmented the kidney into non-fatty tissue is shown in figure 3.1(b). The table below the patient is removed using another script. The kidneys were then segmented manually from the non-fatty tissue with a third script. This script uses an adjustable ellipse to select the kidney and redefines the selected tissue from a value of soft tissue or bone to that of kidney. The previous scripts were written by Prof. Cleveland. The result of the segmentation is shown in figure 3.1(c).

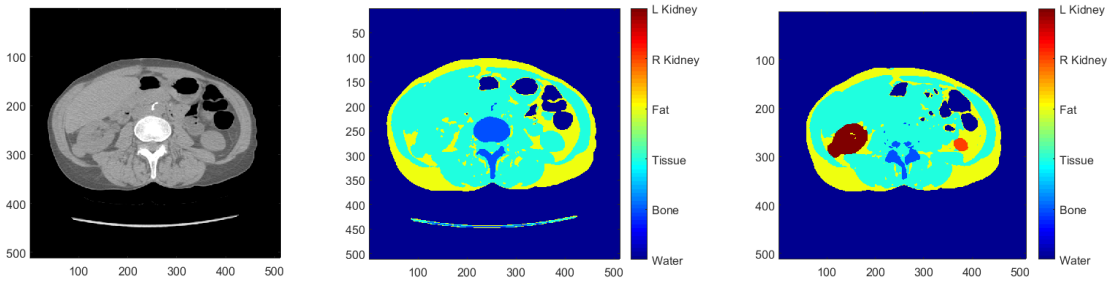

Figure 3.1: The CT scan segmentation process (a) input CT scan slice, (b) result of automatic segmentation of non-fatty tissue, fat and bone. The kidneys are defined as non-fatty tissue in this step, (c) result of manual segmentation of right and left kidneys. The intermediate step of removing the table below the patient has not been shown.

A stack of CT slices form a scanned volume of the patient typically with a wider vertical distance (inter slice distance) than the pixel spacing on the slice plane. To

select a specific patient volume a corresponding number of slices is selected. These are then interpolated using nearest neighbour onto the isometric k-wave simulation grid.

Once in the k-wave structure the segmented tissue types are assigned relevant acoustic properties, table 3.1. The volume outside the body is defined as water.

	Speed of sound (m/s)	Density (kg/m^3)	Attenuation (dB/cm @ 1MHz)
Water	1520	1000	0.00217
Bone	4080	1908	20.00
Tissue	1575	1055	0.60
Fat	1480	950	0.48
Kidney	1560	1050	1.00

Table 3.1: Acoustic properties for different tissue types [111]

3.3 Implementation of the model

The k-Wave toolbox is used to setup the acoustic environment. It is used to define the source, the medium and the required sensor points to store the resulting field.

For modelling the HIFU field of a 200 mm diameter transducer with a resolution of 0.25 mm a grid of 864 x 864 x 864 is required. This is a grid of nearly 645 million points. During the simulation time, there are 21 similar 3D matrices that define the properties on the grid in the spatial domain, as well as 3 real and 3 complex ones in the Fourier domain, all for defining the medium, acoustic quantities, derivative operations, and absorption operators [112].

The computation and memory requirement for running a simulation of this size are significant and therefore, the actual implementation of the discrete equations is done using a C++ code that is an extension of the toolbox. It uses the hierarchical data format (HDF5) library for input/output (I/O) operations. The k-Wave C++ code has been designed to run on distributed computing clusters. This implementation uses the standard message passing interface (MPI) to perform interprocess communications. The MPI version of the FFTW library is used for the Fourier transform calculations [112]. To enable the processing of operations across various processors one dimensional domain decomposition is used to divide

the computational domain over multiple nodes on a cluster. The domain is divided along the third (z) dimension into 2D slices. The total number of MPI processes to use should be $P \leq N_z$, where N_z is the number of points in the z dimension. The number of processes should ideally be a divisor of N_y and N_z, where N_y is the number of grid points in the second dimension y. This is to ensure that there are no idle processes during calculations on regular or transposed data [112].

3.4 Simulation of a single element transducer

The k-Wave toolbox was used to simulate the H101 HIFU single element transducer. The medium was set as a homogeneous medium with water properties, density $\rho = 1000\text{kg/m}^3$, speed of sound $c_0 = 1500\text{m/s}$ and no attenuation. The source was driven as a continuous wave sinusoid with a pressure of 1 Pa at a frequency of 1.1 MHz. It was modelled using the nominal transducer geometry of a bowl of diameter 64 mm and radius of curvature of 63.2 mm.

The linear simulation was run using a spatial resolution of either 0.4 mm (3.5 PPW) or 0.2 mm (7 PPW), using a CFL of 0.3. The corresponding grid sizes were 180 x 256 x 180 and 360 x 512 x 360 respectively. The width of the PML was set to 10 grid points with the PML absorption parameter set at 2 Nepers/grid point. These values were found to provide a reduction in the transmitted wave of 84 dB and a reflection coefficient of -65 dB in a homogeneous and lossless medium in results included in the k-Wave Manual [106]. These values were considered sufficient for use in the current simulation.

Figure 3.2 shows the axial pressure profile obtained from the simulation results using a resolution of 3.5 PPW and 7 PPW in comparison to the analytic O'Neil solution [113]. The pressure profile at the lower resolution of 3.5 PPW is disrupted in the near field with a peak variation at 13 mm. This is due to the source staircasing. This effect is less pronounced in the higher resolution 7 PPW case. The loss of pressure at the diagonal grid points has resulted in a lower pressure at the focus. The value of the focal gain for the analytical solution is 40.22, which is 1.09 times greater than for the simulation with 7 PPW. This ratio agrees with values obtained

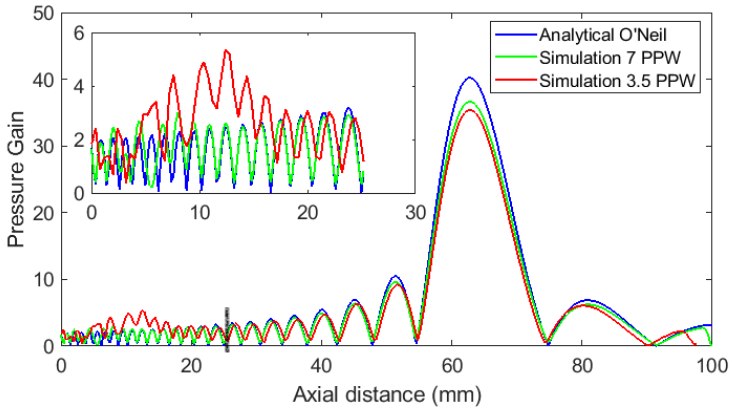

Figure 3.2: The axial peak pressure profile of the H101, comparing simulation and analytical results calculated using the O'Neil solution

in [109], where Martin et al. calculated the effect of source staircasing on the reduction in the generated acoustic pressure for different PPW values.

3.5 Simulation of the JC-200 transducer

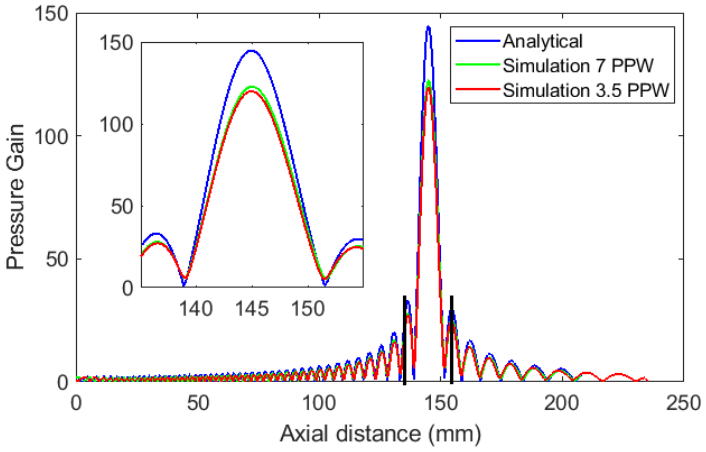

Figure 3.3: Axial pressure profiles for the JC-200 transducer, the blue line is the result of the O'Neil solution, red and green are the results of the simulation using a resolution of 0.369 mm and 0.2467 mm respectively

To perform clinically applicable simulations, the transducer used in the USgHIFU device (Model JC-200, HAIFU) was considered. It is a 0.95 MHz transducer, with a diameter of 200 mm and focal length of 145 mm. The -6 dB pressure focal spot is approximately 1.2 mm transversely and 5.9 mm axially. The JC-200 axial and

lateral pressure profiles are shown in figure 3.3. Similar to the simulation for the H101 transducer in figure 3.2 the lower resolution of 0.369 mm, 4.2 PPW gives a 2% lower estimation of the focal gain than the higher resolution of 0.2467 mm, 6.3 PPW.

3.6 Convergence Test

The choice of the grid resolution and CFL number is important for the simulation accuracy. A finer resolution gives better accuracy, however, it also impacts the size of the grid with a two-fold increase in resolution resulting in an eight-fold increase in the computational grid size. Therefore, the resolution has to be chosen with the required memory and execution time in mind. In this section the effect of changing the points per wavelength in the k-Wave simulation is investigated on the resulting focal gain of a transducer with the same F-number as a clinical JC-200 system's transducer, but with half the dimensions. A smaller transducer was chosen to reduce the required grid size and computation resources. The CFL number was fixed, resulting in a time step that decreases with the decrease in spatial resolution. The dimensions of the transducer are: outer diameter of 100 mm, inner diameter of 30 mm and radius of curvature of 72.5 mm. The transducer was defined with a source pressure of 1 MPa and frequency of 0.95MHz.

The convergence test was done using linear simulations for three different medium cases: a homogeneous medium, with sound speed of water and no attenuation, and two heterogeneous media cases one with only soft tissue and the other with soft tissue and bone. The latter two cases are more representative of the application of the model for use as a treatment planning tool for patients who are undergoing HIFU treatment.

For a heterogeneous medium, the CFL should be chosen so that $CFL \leq (c_0/c_{max})$ which would ensure $\Delta t \leq \Delta x/c_{max}$. The maximum sound speed in the grid was the sound speed in bone, which was set as 4080 m/s. The minimum sound speed was that of fat, set as 1480 m/s. The smallest $c_0/c_{max} = \frac{1480}{4080} = 0.3627$. CFL was chosen to be less than half c_0/c_{max}, resulting in a CFL of 0.15.

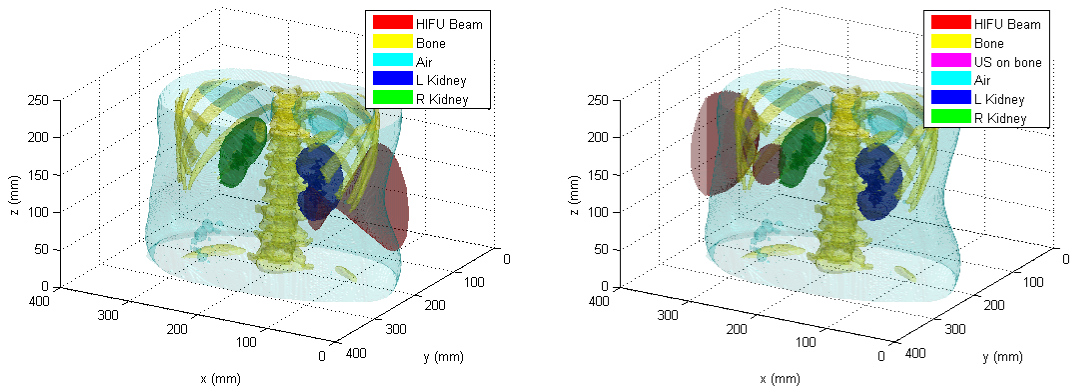

(a) **(b)**

Figure 3.4: The entry path of the ultrasound beam is shown relative to the patient geometry for the convergence test using heterogeneous tissue. The bone is shown in yellow, the right kidney is in blue and the left in green. Fat and muscle tissue are not displayed. (a) Soft tissue only in the HIFU propagation path, (b) Tissue with bone in the propagation path

The medium was derived from the anonymised CT scan. The pressure was saved over a volume of 106 mm^3 up to 119 mm^3, depending on resolution and number of grid points was selected from the segmented CT volume. The transducer was positioned as shown in figure 3.4.

3.6.1 Results

Figure 3.5 shows the axial focal plane for the convergence tests. The plots show the pressure gain overlaid on the tissue structure from the CT scan with the target focal point shown with a black cross. The position of the transducer is shown by the red curve. The effect of the heterogeneous tissue layers can be seen when comparing the sharp focal region in water 3.5(a) with the less defined region in figures 3.5(b) and 3.5(c).

Figure 3.6(a) shows the focal gain as a function of PPW for the water simulation. The focal gain was calculated as the maximum pressure divided by the source pressure of the transducer. The change in focal gain is within 11% across the range of chosen PPW values. The percentage change with each resolution increase is shown in table 3.2. It shows that the biggest increase in focal gain happens at the change from 4.2 PPW to 6.3 PPW, with further increases in resolution resulting in

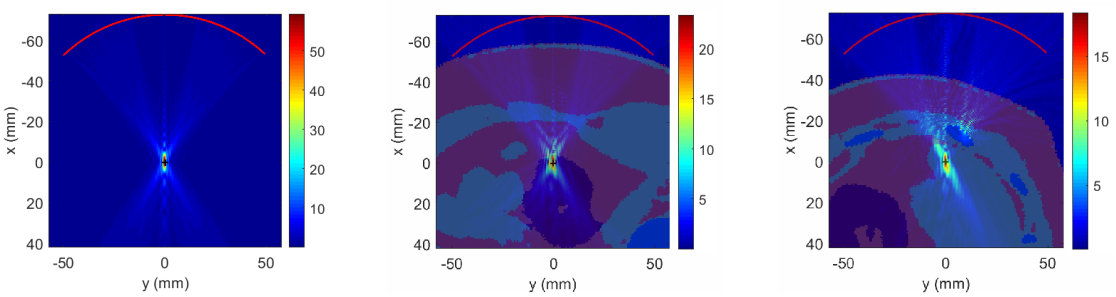

(a) (b) (c)

Figure 3.5: The transverse focal plane for the convergence test at 6.3 PPW for three different cases (a) homogeneous medium, (b) soft tissue only and (c) soft tissue and bone. The black cross shows the target point and the red curve is where the transducer is positioned.

a combined increase of <6%. The difference in the homogeneous medium results can be explained by the effect of source staircasing due to source discretisation [109]. For the heterogeneous media staircase errors also manifest themselves at tissue interfaces as discussed in section 3.1.1.

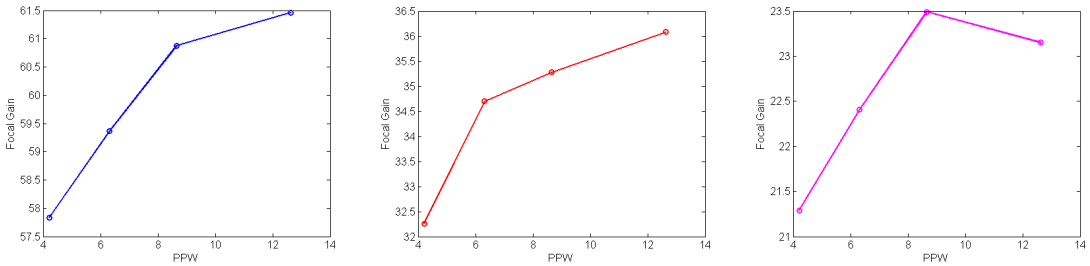

(a) (b) (c)

Figure 3.6: The focal gain as a function of points per wavelength for the HIFU propagation in (a) homogeneous, non-attenuating medium, (b) heterogeneous tissue without bone in ultrasound path, (c) heterogeneous tissue with bone.

	Water	No bone	Bone
4.2 PPW ->6.3 PPW	2.59%	7.03%	5%
6.3 PPW ->8.7 PPW	2.48%	1.64%	4.6%
8.7 PPW ->12.6 PPW	0.94%	2.22%	-1.47%

Table 3.2: The percentage change in the focal gain as the resolution increases, the resolution is expressed in points per wavelength

Another aspect that was considered in choosing the spatial resolution was the shape of the focal spot and its position. Table 3.3 shows the width of the -6 dB

focal spot in all three dimensions for the homogeneous medium test. For 6.3 PPW and greater the variation in width is less than 10%.

	width (mm)		
	x	y	z
4.2 PPW	7.77	1.85	1.85
6.3 PPW	7.65	1.73	1.73
8.7 PPW	7.59	1.67	1.67
12.6 PPW	7.65	1.60	1.60

Table 3.3: The width of the - 6dB value for the focal gain, calculated in the x, y and z coordinates, for water

For the tissue only simulations, figure 3.7 shows the transverse focal plane results and for tissue with bone the results are shown in figure 3.8. Tables 3.4 and 3.5 were used to quantify the change in width and focal point shift for tissue only simulations and tissue with bone simulations respectively. From tables 3.4 and 3.5 the difference in focal position for all the different resolution choices is no more than 0.25 mm in any direction (which is 1/6 of a wavelength). There is no consistent shift with either an increasing or decreasing trend, except in the z direction in table 3.5. For the -6 dB volume width again there is no trend. The width values were determined directly from the number of pixels covered by the -6 dB pressure volume. This can result in discritisation effects as can be seen in the identical width values for y and z for 6.3 PPW and 12.6 PPW in table 3.5.

	width (mm)			shift (mm)		
	x	y	z	x	y	z
4.2 PPW	7.03	1.85	1.85	0.37	-0.74	0.74
6.3 PPW	7.15	1.73	1.73	0.25	-0.74	0.74
8.7 PPW	7.22	1.67	1.85	0.185	-0.93	0.56
12.6 PPW	6.91	1.73	1.73	0.27	-0.86	0.62

Table 3.4: The width of the - 6dB value for the focal gain, calculated in the x, y and z coordinates, and the shift in the peak pressure from the transducer's focal point. For simulations with soft tissue only.

The time and computational resources required to run these simulations were also considered when choosing a suitable resolution. Table 3.6 shows the resource requirements for the convergence test in the tissue with bone simulation. The

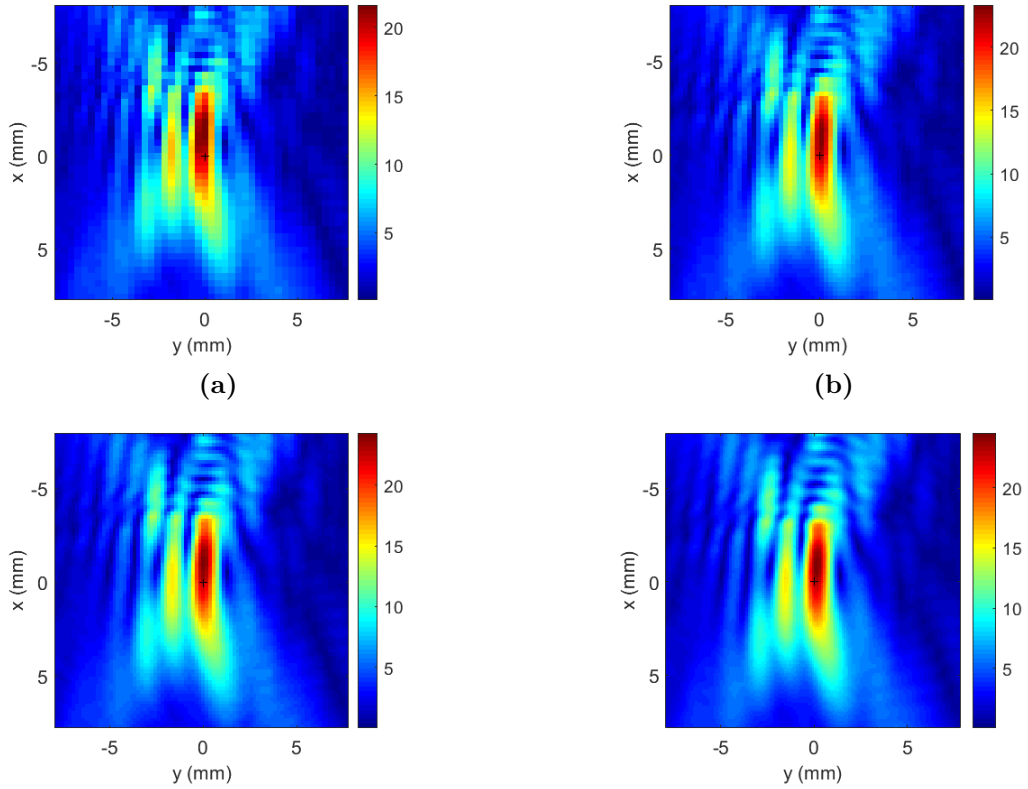

Figure 3.7: The transverse focal plane from the soft tissue simulation convergence test, for (a) 4.2. PPW, (b) 6.3 PPW, (c) 8.7 PPW and (d) 12.6 PPW

	width (mm)			shift (mm)		
	x	y	z	x	y	z
4.2 PPW	8.51	2.22	2.59	0	0	0.37
6.3 PPW	8.63	2.22	2.71	0	-0.25	0.49
8.7 PPW	8.33	2.22	2.41	-0.19	0	0.56
12.6 PPW	8.63	2.22	2.47	-0.12	-0.25	0.62

Table 3.5: The width of the - 6 dB value for the focal gain, calculated in the x, y and z coordinates, and the shift in the peak pressure from the transducer's focal point. For simulations with soft tissue and bone.

increase in the grid size means an increase in the number of processors and memory used. The increase in time steps also results in an increase in the simulation time.

To undertake the simulations on CT scans of patients who were treated using the JC-200 HIFU system the size of the grid has to be increased by two in each dimension. Therefore, for linear simulations a grid resolution of 6.3 PPW was selected as a compromise between the pressure amplitude and computational

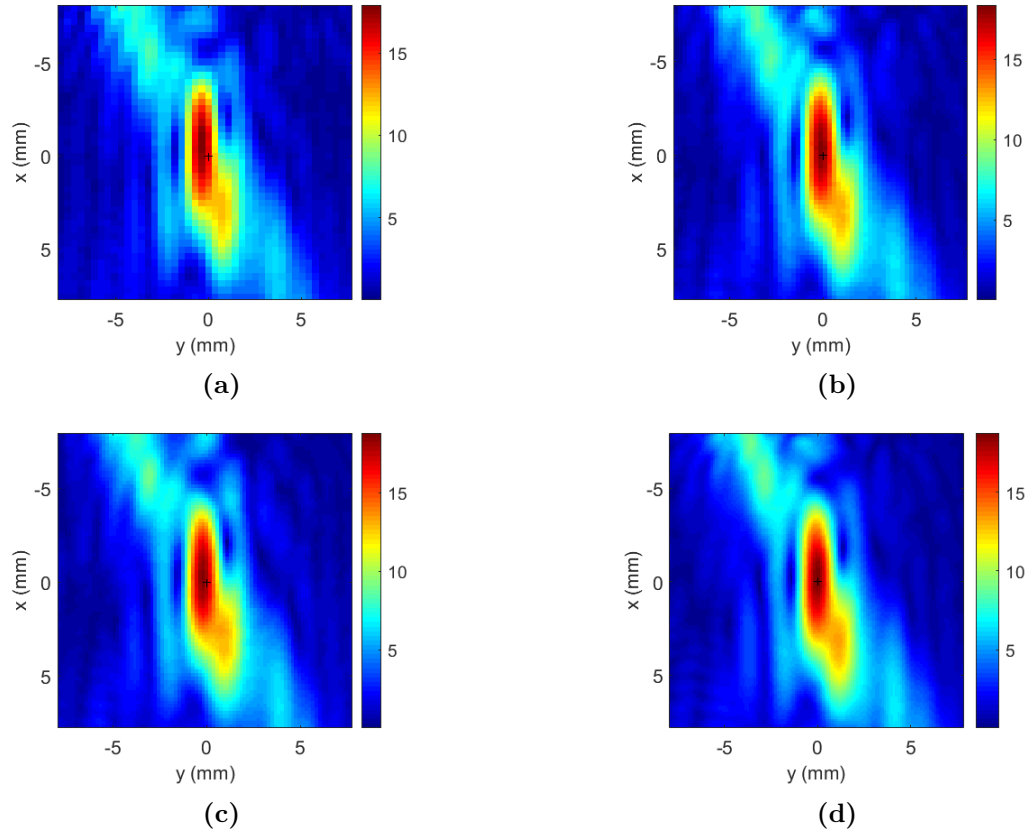

Figure 3.8: The transverse focal plane from the tissue with bone simulation convergence test, for (a) 4.2 PPW, (b) 6.3 PPW, (c) 8.7 PPW and (d) 12.6 PPW

	Spatial resolution (μm)	Temporal resolution (ns)	MPI processes	Peak memory (GB)	Computation time (hh:mm:ss)
4.2 PPW	370	13.6	81	7.8	01:01:33
6.3 PPW	246.67	9.07	81	16.63	05:14:38
8.7 PPW	185	6.8	81	31.63	13:44:02
12.6 PPW	123.33	4.53	144	74.59	51:20:35

Table 3.6: The computational resources required for running the simulation for HIFU propagation for the tissue with bone simulations, using a CFL of 0.15.

resources. This will give a value for pressure to within 10%, and the location of the focal point to within < 0.25 mm.

3.7 Thermal Simulation

The thermal simulations were also conducted using the k-Wave toolbox. The temperature rise caused by the ultrasound beam can be expressed using Pennes' bioheat equation [114] with the addition of a heat source term due to ultrasound absorption:

$$\rho_t C_t \frac{\partial T}{\partial t} = k_t \nabla^2 T - w_t C_b (T - T_0) + Q_s \tag{3.14}$$

where ρ_t is the tissue density; C_t is the specific heat capacity for tissue, T is the temperature field over the specific volume; T_0 is the temperature of the blood; k_t is the thermal conductivity for tissue; w_t is the average blood perfusion rate in the tissue; Q_s is the heating rate resulting from the HIFU field.

The ultrasound heat source's heating rate for the thermal simulation was obtained from the acoustic pressure resulting from the acoustic simulation using the following equation:

$$Q_s = 2\alpha I_{spta} = \frac{2\alpha p^2}{2\rho c} = \frac{\alpha p^2}{\rho_t c_t} \tag{3.15}$$

where I_{spta} is the spatial peak, temporal average intensity, α is the attenuation coefficient, p is the acoustic pressure, ρ_t and c_t are the density and speed of sound in tissue respectively. The attenuation coefficient is used in the equation in place of the absorption coefficient based on an assumption that all attenuation is due to absorption. The scatter component at low megahertz range accounts for 10-15% of attenuation [115]. For a frequency value less than 1 MHz, 0.95 MHz, the scatter component would decrease further and result in a contribution of less than 10%.

The simulations were undertaken using k-Wave's thermal simulation function kWaveDiffusion. It implements a time domain solution for the bioheat equation based on the k-space pseudospectral method with the spatial gradients computed using the Fourier collocation spectral method described earlier, and the temporal gradients calculated using a k-space corrected finite difference technique.

To give a measure of the extent of the resulting cell damage due to the achieved temperature the k-Wave simulation is also used to calculate the cumulative equivalent minutes at 43°C ($CEM43°C$) for each grid point. This method of expressing the

thermal dose as an equivalent duration of exposure at 43°C was put forward by Sapareto and Dewey [116]. It is termed the "thermal isoeffective dose" and converts a specific time-temperature combination to the equivalent time at 43°C through the following equation:

$$CEM43°C = \sum_{t=0}^{t=final} R^{(43-T)}\Delta t \tag{3.16}$$

where $CEM43°C$ is the cumulative number of minutes at 43°C, Δt:time interval of temperature reading in minutes, T average temperature during time Δt, $R = 0.5$ above 43°C and $R = 0.25$ below 43°C. The equation above uses the sum of the temperature values at the discrete time points at a step size of Δt as an estimate of the continuous temperature values $T(t)$ from $\int_0^{t_{final}} R^{43-T(t)}\mathrm{dt}$. The $CEM43°C$ has become the most accepted means of expressing the expected damage to cells based on the temperature used and duration of exposure [117].

The temperature value of 43°C was selected because it is close to the break point value where there is a reduction in the slope in the Arrhenius relationship between the rate of cell death and temperature [117].

The lesion boundary is determined by selecting a value for $CEM43°C$ at which complete thermal necrosis occurs. A range of values between 50 and 240 minutes was determined in the literature [45], from which a value of 240 $CEM43°C$ was selected here since this is the upper limit.

The grid size used for the acoustic simulations was kept for the thermal simulations. However, for the time-step a step size analysis was undertaken and is described in the section below.

3.7.1 Thermal simulation time-step convergence test

The required time step for the thermal simulations was determined by varying the time step from 0.5 s down to 0.025 s, for a patient model derived from an anonymised CT scan of patients treated during a HIFU kidney ablation clinical trial [75]. Table 3.7 shows the maximum temperature value obtained for the simulations for each time step and the corresponding time it took the simulation to run. It

shows that there is a small variation of less than 0.07% over all values. The choice for the step size was 200 ms, because 50% of the change from 500 ms resolution to 25 ms resolution was between 200 ms and 500 ms and it had an acceptable computation time of 14 minutes.

Time step (ms)	Input pressure (kPa)	Maximum temperature (°C)	Duration minutes
500	130	67.29	7
200	130	67.31	16
100	130	67.33	32
50	130	67.33	65
25	130	67.34	137

Table 3.7: The time convergence results, simulation 3 (described in chapter 5) was used for the test.

4

Transducer Characterisation

The characterisation of the JC-200 system transducer is important in order to understand the pressure profile and the conversion from power on the control panel to pressure in the ultrasound field. The method that is implemented here uses a hydrophone scan of a pre-focal plane which is then back propagated to form the source plane, [118–120].

4.1 Plane Back-Propagation using the Angular Spectrum Method

The back projection of the scanned pre-focal plane can be performed with different techniques, using the angular spectrum method (ASM) [118, 120–122], and the Rayleigh integral [119]. Another approach determines an equivalent source using a gradient-based optimisation method that matches the resulting modelled plane to the measurement plane data [123]. The method used here is the ASM, which propagates the angular spectrum of the field, with the assumption that linear acoustics holds. The present ASM implementation modified code written by Dr. Joseph Blackmore.

The angular spectrum represents the decomposition of the field into a superposition of plane waves that propagate independently, and can then be recombined to reconstruct the complete field. For any plane z, within a homogeneous medium,

the velocity potential in the frequency domain can be written as [120]:

$$\Phi(k_x, k_y, z) = G(k_x, k_y)e^{i(\pm k_z z - 2\pi f t)} \tag{4.1}$$

where $G(k_x, k_y)$ is the two dimensional spatial Fourier transform of the velocity potential at the source $z = 0$, k_x and k_y the transformation variables of x and y, $k_z^2 = k^2 - (2\pi)^2(k_x^2 + k_y^2)$ is the wavenumber in the z direction, $k = 2\pi f/c_0$, f is the frequency and c_0 the speed of sound. The velocity potential can be obtained from a source pressure using $\phi = \frac{p}{\rho_0 c_0 ik}$. The spectrum is propagated along the z axis using the propagation factor $e^{\pm ik_z z}$, with the $\pm$ sign showing that the wave can propagate in either the forward (+ve) or backward (-ve) directions. The velocity potential spectrum at the required plane is then calculated using equation 4.1 with the propagation factor $e^{\pm ik_z z}$ having z set as

The spectrum is propagated along the z axis using the propagation factor $e^{\pm ik_z z}$, with the $\pm$ sign showing that the wave can propagate in either the forward (+ve) or backward (-ve) directions. The velocity potential spectrum at the required plane is then calculated using equation 4.1 with the propagation factor $e^{\pm ik_z z}$ having z set as

gated along the z axis using the propagation factor $e^{\pm ik_z z}$, with the $\pm$ sign showing that the wave can propagate in either the forward (+ve) or backward (-ve) directions. The velocity potential spectrum at the required plane is then calculated using equation 4.1 with the propagation factor $e^{\pm ik_z z}$ having z set as the required distance to propagate and the sign defined for the required direction. The inverse Fourier transform is used to obtain the velocity potential, ϕ, which is then used to calculate the pressure at the new plane using:

$$p = \rho_0 c_0 ik\phi \tag{4.2}$$

The choice of the position and size of the pre-focal plane at which to measure the pressure was based on the analysis presented by Sapozhnikov et al [119]. The position of the pre-focal measurement plane z_h was a third the radius of curvature away from the geometric focus, $z_h = \frac{2}{3}z_f$. The size of the 2D plane is defined by the half length of the side a_h, see figure 4.1.

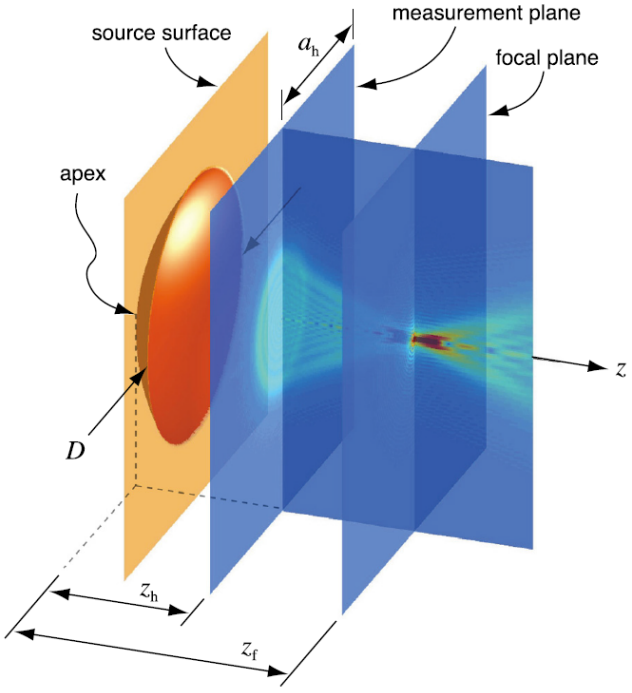

Figure 4.1: The schematic shows the position of the measurement plane at a distance z_h. This plane is back propagated to a source plane which can then be forward propagated to form the pressure field in full. Schematic from [119]

Because of the size of the JC-200 transducer, with a diameter of 200 mm, a full 2D scan was not practical, since it would take a few days to undertake. For example, assuming that a plane, 53 mm pre-focally is scanned, even with only a quarter of that plane scanned at a step size of 0.7 mm (2 PPW), this would require the acquisition of 10,000 points. With a PC controlled acquisition system it would take 29 hours to perform the scan and it was not practical to gain that level of access at the hospital. Instead the symmetry of the source was exploited and radial scans were used to recreate the full 2D plane.

4.2 Pre-focal Simulation of the Field of the H102 Research Transducer

A preliminary test of the ability to perform an extrapolation from a radial scan to a complete 2D plane was done on a single element 1.1 MHz transducer with an outer diameter of 64 mm, inner diameter of 20 mm and a radius of curvature of

62.64 mm (Model H102-35E, Sonic Concepts, Bothell, WA, USA).

The concept was first tested on simulation results. A k-Wave simulation of the H102-35E was run at a resolution of 7 PPW. The pressure waveform was recorded at a plane positioned 21 mm pre-focally, ie. 41.64 mm from the transducer bowl's rear surface. The amplitude and phase were extracted using the FFT. The plane was then back propagated 33.64 mm towards the transducer resulting in a pressure distribution defined on a plane 8 mm in front of the transducer's rear surface. The speed of sound was set to 1500 m/s.

First the full 2D plane was propagated. Then to make the situation similar to the experimental scan a radial line was chosen from the plane and rotated to fill the 2D plane. Figure 4.2 shows the radial line, the interpolated 2D area of phase and amplitude and the result of the AS back propagation. Since a 2D spatial Fourier transform is used to propagate the angular spectrum in the k-space domain, zero padding was performed around the 2D plane to increase the resolution in k-space and reduce wrap-around artifacts due to the use of the periodic discrete Fourier transform. In figure 4.2(c) and 4.2(d) it can be seen from the shape of the 2D area that the interpolation has successfully achieved the transducer's characteristic annular pattern for the amplitude and phase in the transverse plane. The angular spectrum (AS) back propagated plane at the edge of the transducer in figure 4.2(e) shows that the amplitude reflects the pattern of the transducer's surface with the 20 mm circular cut-out discernible in the centre.

To test what effect reducing the scan size would have on the resulting pressure profile the 72 mm radial line was truncated to 38 mm based on a choice of 3/1 ratio of radial line to beam size at the 41.64 mm plane. This factor was chosen because it was reported to result in a maximum error of approximately 5% in pressure at any point in the field [119]. Figure 4.3 shows the amplitude and phase resulting from truncating the radial line. When comparing the results of the AS back propagation in figure 4.2(e), 4.2(f) and 4.3(c), 4.3(d) it is noted that the amplitude and phase distributions are similar. Also, the values for the amplitude are within the same range, with the maximum pressure within 2%.

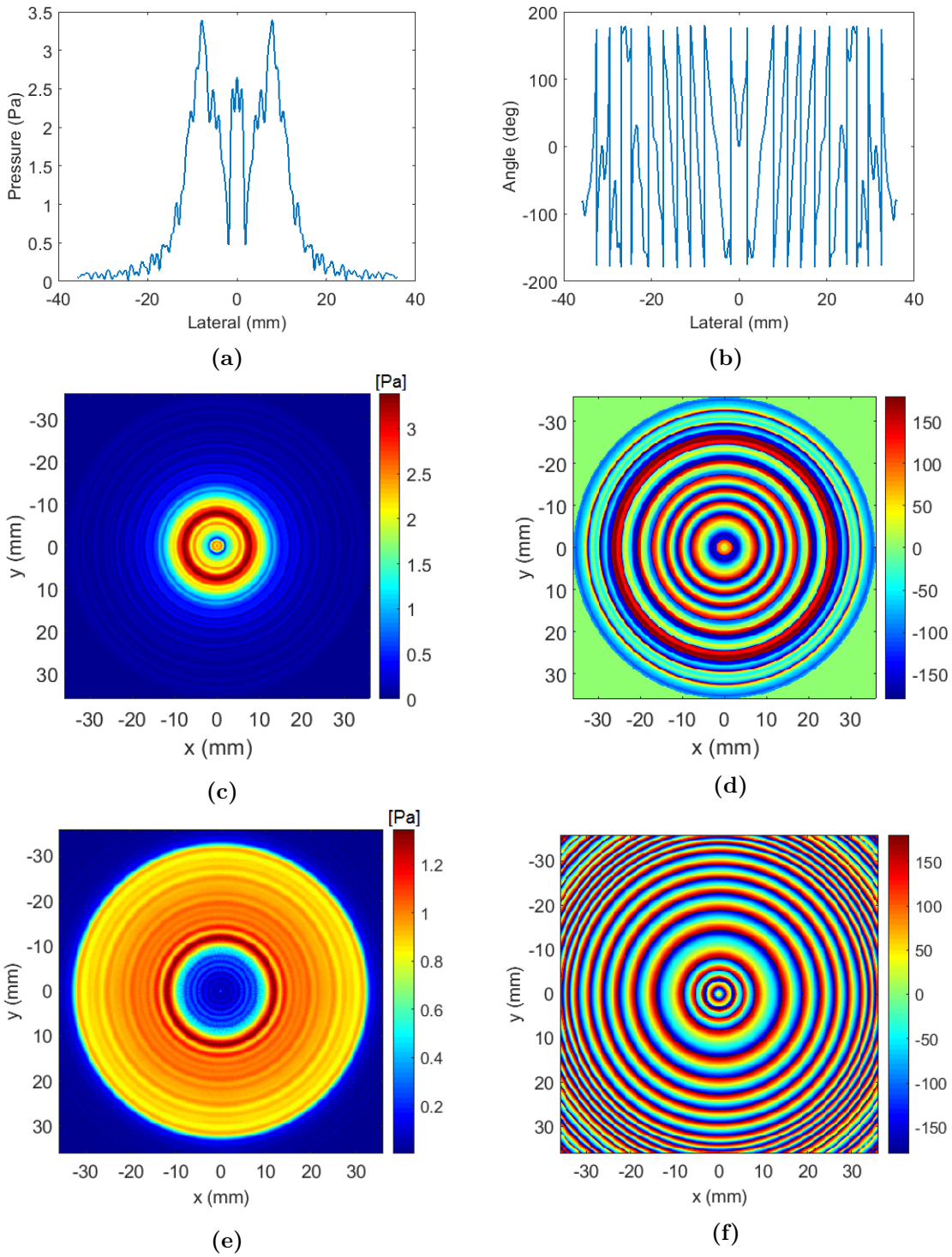

Figure 4.2: AS back propagation from a radial line at 41.64 mm using a simulation of the H102-35E transducer, (a) amplitude plot for the radial line, (b) phase plot for line. (c) Amplitude covering 2D area created by rotating radial amplitude in (a), (d) 2D phase created from phase in (b). The resulting AS back propagated plane: (e) amplitude and (f) phase.

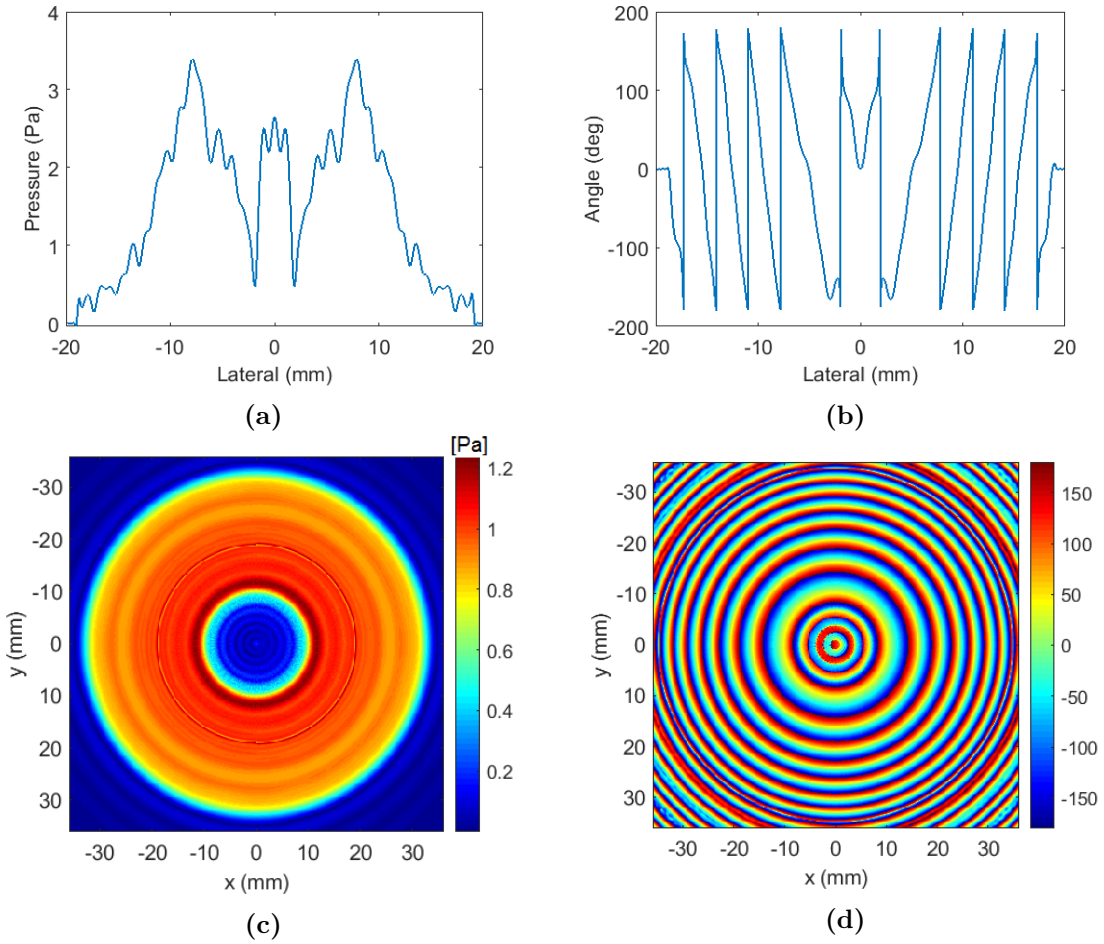

Figure 4.3: AS back propagation from a radial line at 41.64 mm using a simulation of the H102-35E transducer, (a),(b) The amplitude and phase of the truncated radial line, (c),(d) the amplitude and phase of the resulting AS back propagated plane.

The axial pressure profile obtained from using the back propagated plane as the source condition imposed as a Dirichlet boundary condition in a k-Wave simulation with 7 PPW resolution and $c_0 = 1500$ m/s is shown in figure 4.4. The pressure at the focus for the back propagated 2D plane and for both the interpolated complete radial line and truncated line simulations are 32.91 Pa, 32.86 Pa and 32.88 Pa, which are not significantly different from the 33.39 Pa obtained from the original simulation. The pre-focal profile does not approximate well to the expected shape below 30 mm for the truncated line and below 22 mm for the 2D plane and complete radial line results. This is likely because the measurement plane is $\sim$ 33.64 mm in front of the edge of the transducer bowl resulting in the loss of

the waves that have diverged before reaching the measurement plane. Waves not captured by the aperture could have constructively and destructively interfered to form nulls and peaks on axis [119].The truncated line simulation has an added loss due to the smaller aperture used.

The profile obtained from the truncated line has a lower pressure value at the first post-focal lobe. The main lobe however is not affected by truncation, with the green and black lines in figure 4.4 overlapping. This indicates that the loss of energy is not affecting the main lobe which is the most relevant part of the pressure profile for quantifying ablation.

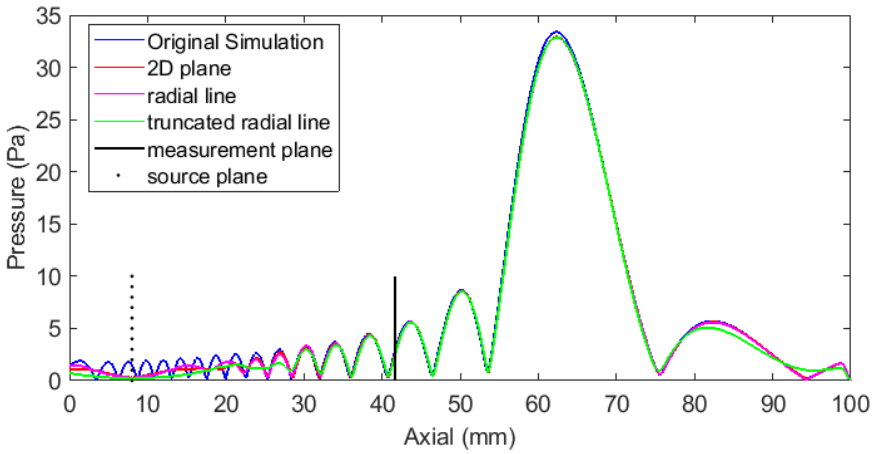

Figure 4.4: Comparison of the axial pressure profile of the k-Wave simulation when using different source conditions, the dotted vertical line shows the position of the original plane that was back propagated.

4.3 Pre-focal Measurements of the Field of the H102 Research Transducer

The radial scanning approach was tested experimentally using the H102 transducer. To test the symmetry of the transducer and use multiple average lines for added accuracy two radial lines at right angles were scanned at a plane 21 mm pre-focally. The results of amplitude and phase for the linear scans were averaged to form a single line that was interpolated and used to fill the 2D plane. This

is a good test run for what would need to be implemented on the JC-200, which is nearly twice as big as the H102.

The HIFU transducer was driven through a matching network by a 55 dB radio frequency power amplifier (A300, E & I, Rochester, NY, USA) with a 60 cycle input signal from a function generator (33220A; Agilent Tech., Palo Alto, CA, USA). The pressure signal was recorded by a 400 μm diameter needle hydrophone (SN1228, HNA series, ONDA). The hydrophone was moved using a 3D positioning system. Figure 4.5 shows the experimental setup. Two experiments were undertaken one without acoustic absorbers, the other with two acoustic absorbers placed on the hydrophone in front of the holder as can been seen in figure 4.5(c). The acoustic absorbers were required for the JC-200 setup since the water air interface is closer to the hydrophone, therefore it was important to test their effect on the H102 setup.

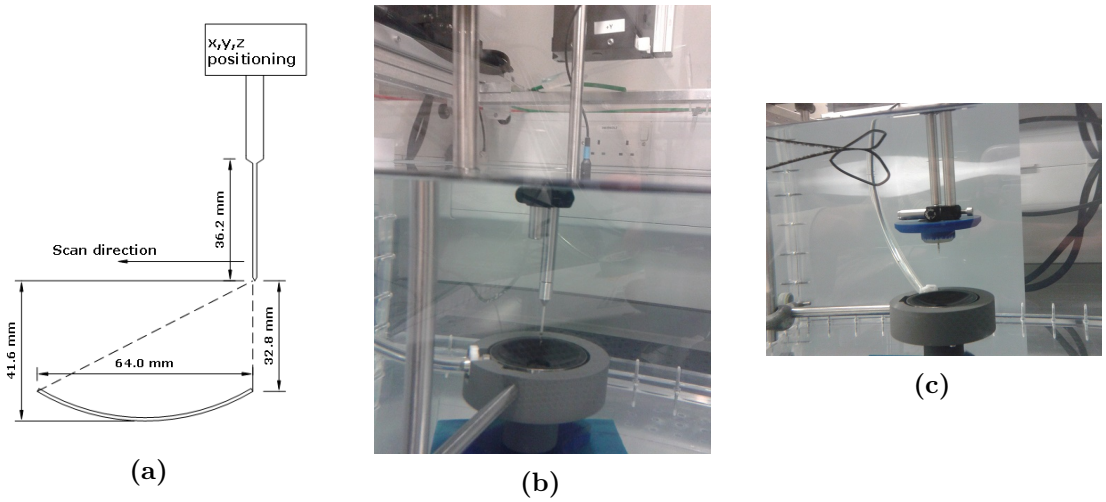

Figure 4.5: The radial pre-focal scan of the H102-35E transducer, (a) shows a schematic, (b) the picture of the setup with no acoustic absorber and (c) the picture of the setup with two acoustic absorbers

To obtain the pre-focal plane scan the hydrophone was first positioned at the focal point (highest pressure). It was then moved 21 mm towards the transducer. Then a radial plane scan was performed to find the centre of the pre-focal plane. In both the experimental setups shown in figure 4.5 the centre of the pre-focal plane was offset by a maximum of 0.2 mm from the centre of the focal plane. This indicates that the transducer is slightly tilted and misaligned to the axis of the

scan plane. Before the scan the position of the hydrophone was modified to ensure that the radial scans were each passing through the centre point of the pre-focal radial plane. The radial scans at right angles were acquired from -36 to 36 mm with a 0.2 mm step size. In both experiments the temperature of the water was measured and found to be 18°C and 19° C which result in a speed of sound of 1476 m/s and 1479 m/s respectively [124]. Measuring the speed of sound was important for the accurate reconstruction of the pressure profile [119].

A 3 cycle window was selected from the recorded waveform that guarantees the inclusion of all signals from all parts of the transducer, and ensures no reflections are in this window, that is the signal represents a continuous wave condition. The FFT was then used to extract the amplitude and phase from this segment at the centre frequency of the transducer, 1.1 MHz. The amplitude and phase obtained from the two radial lines were then averaged to give a single line of amplitude and phase. The positive and negative sides of this resulting line were further averaged in order to obtain a symmetric line. Figure 4.6 shows the resulting amplitude and phase profiles. The phase was unwrapped before averaging.

The averaged symmetric radial line was then interpolated and used to fill the pre-focal radial plane. The AS method was used to back propagate the plane in order to obtain a source plane for use in the k-Wave simulation. Figure 4.7 shows the resulting 2D source planes for the complete radial line and results from using a truncated line to represent 38 mm scan length. The results for the amplitude of the AS back propagation obtained from the truncated line are very similar to those obtained from the non-truncated one. However, it is apparent that the annular rings are more distinct for the non-truncated case.

The source planes were used in k-Wave to simulate the H102 transducer's field in a homogeneous medium with a speed of sound of 1500 m/s and no attenuation. The grid size was 360 x 512 x 360 with 0.2 mm resolution, 7 PPW. The resulting axial and lateral pressure profiles are normalised and shown in figure 4.8 for different experimental and window selection cases. All the simulations were undertaken with the input pressure defined as an additive source, except for one where the input

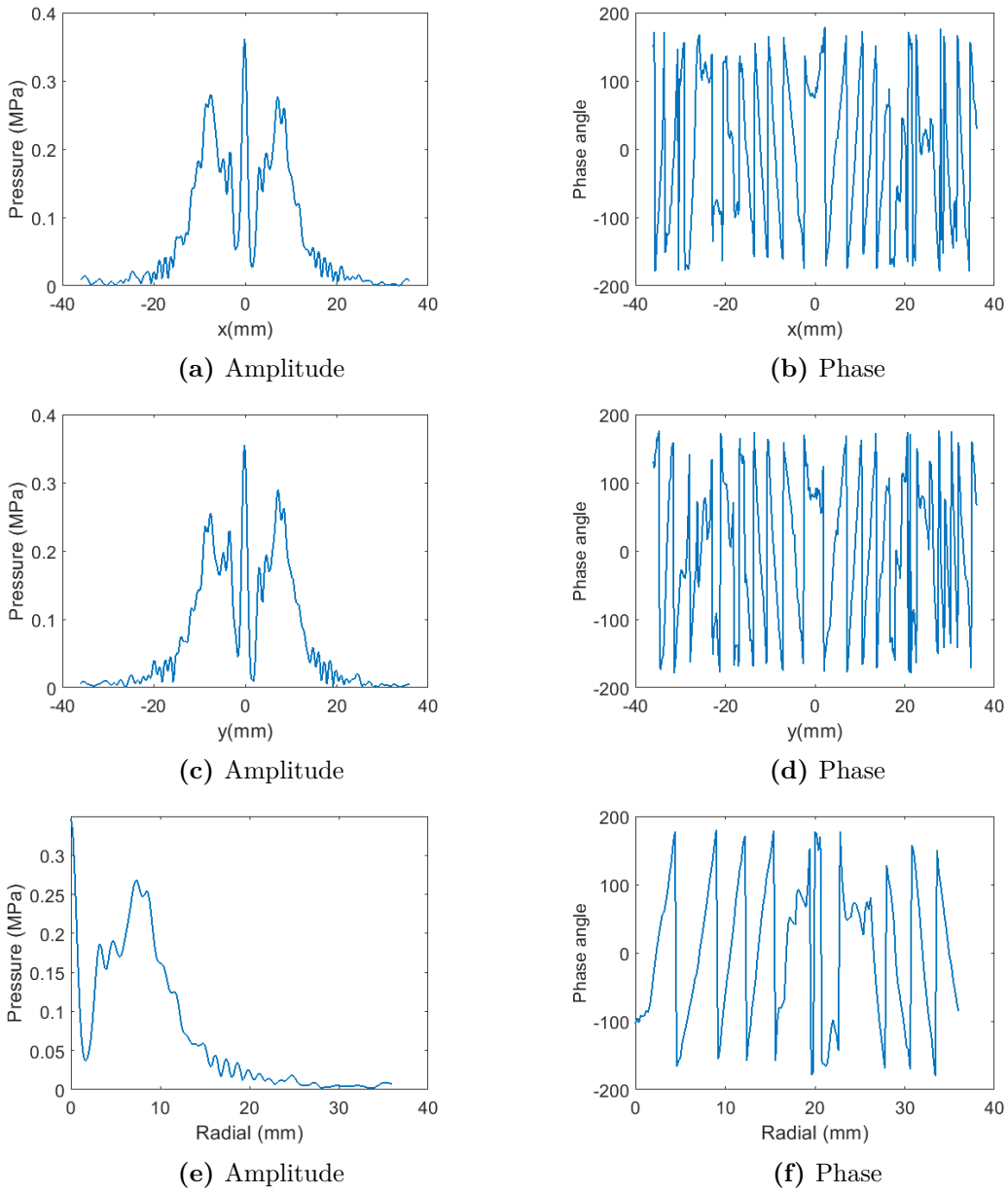

(a) Amplitude **(b)** Phase

(c) Amplitude **(d)** Phase

(e) Amplitude **(f)** Phase

Figure 4.6: The radial line values of amplitude and phase at 1.1 MHz. (a),(b),(c),(d) show the values extracted from the two right angle line scans, these values are averaged and the result of their average is averaged around the centre point to obtain the symmetric radial line shown in (e) and (f)

pressure was defined as a Dirichlet source condition. The additive source applies the input pressure as an injected mass source whereas the Dirichlet condition setting imposes the source plane as a fixed boundary condition.

The magenta and red lines are the result of using the data from the experiment with the acoustic absorbers to reduce reflections. The red line resulted from selecting

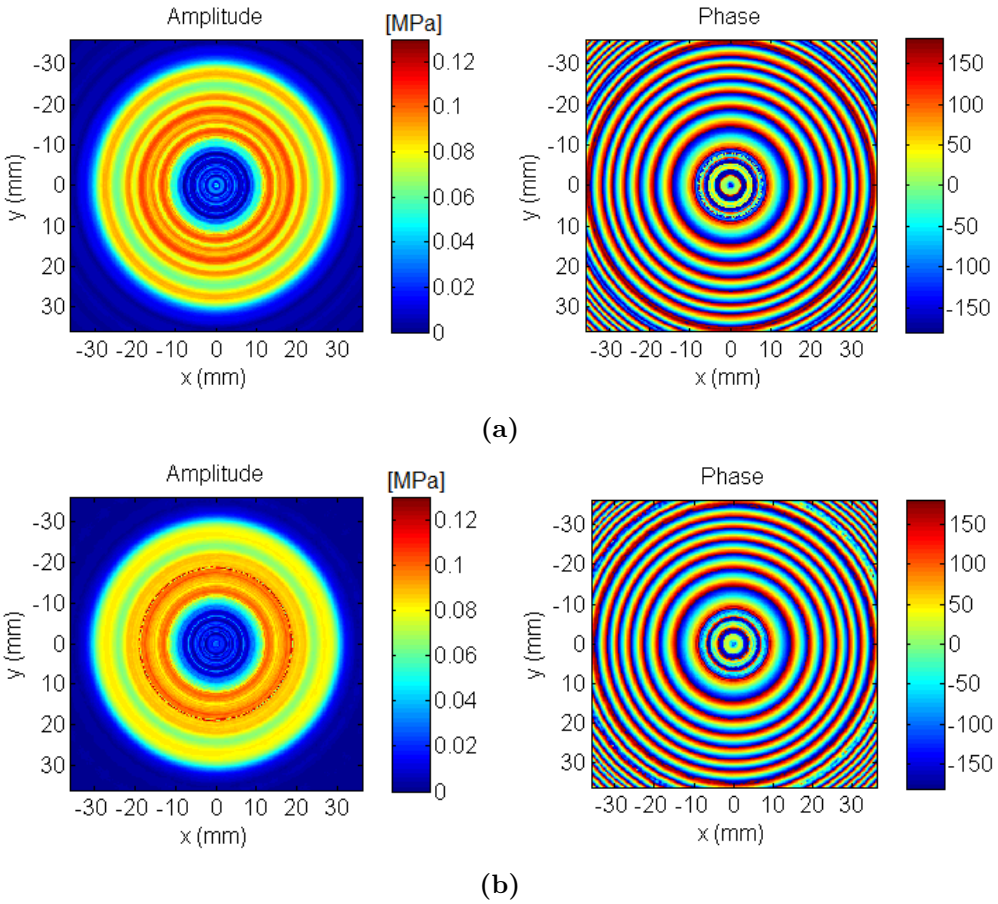

Figure 4.7: The AS back propagation for the radial scan measurements of the H102, (a) using a 72 mm radial line scan, (b) using only the 38 mm centre section of the radial scan.

a window that is 3 μs earlier than that used to produce the magenta line. This was a test of how sensitive the result was to the choice of window position. The results show that the second condition of starting at 65 μs has done a better job in estimating the pressure at the post focal first side lobe. However, pressures from both conditions are overlapping in the main lobe. The yellow line from the Dirichlet condition simulation is overlapping with the red line resulting from the simulation of the same signal using an injected mass source setting.

The cyan and blue lines in the figure are the simulation results from the experiment with no acoustic absorbers. One with the full radial line, 72 mm, the other with the amplitude and phase truncated to represent a 38 mm line scan. The pressure profile for both simulations is overlapping with only the first 20 mm showing a deviation in the pressure pattern. This is similar to the result obtained

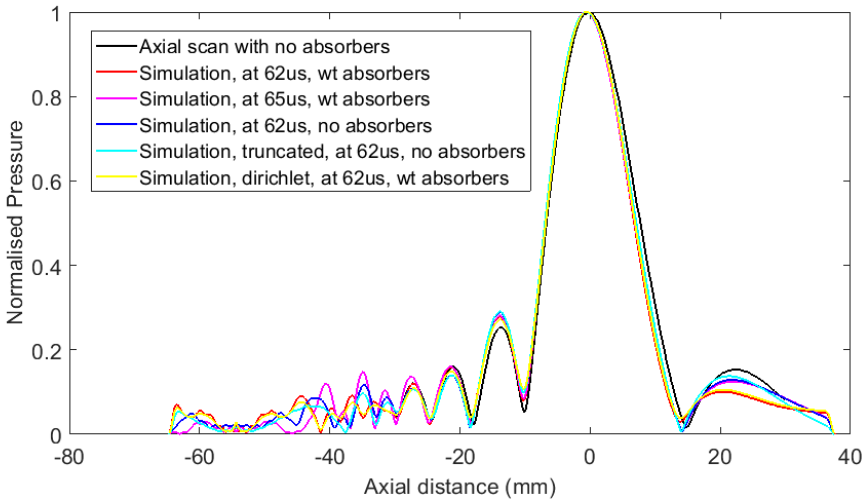

(a)

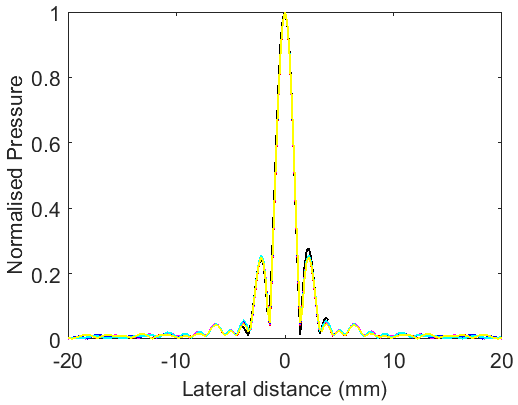

(b)

Figure 4.8: The comparison of the pressure profiles between an axial scan measurement of the H102 and simulations from source conditions obtained from pre-focal scans of the same transducer

with the simulation plane in section 4.2.

As with the previous results in section 4.2 all the simulations result in a pressure profile in the near field that does not have the characteristic nulls and peaks. The experimental axial scan did not extend far enough towards the transducer to enable a comparison.

The maximum pressure obtained at the transverse plane, at the focal point defined in the simulation, for all four cases was 2.78±0.01 MPa. The maximum pressure on the axial line passing through the focal point was 2.79±0.01 MPa. These pressure values represent a 15% increase in the maximum pressure value that

was obtained from an axial scan measurement of the H102, which gave a value of 2.43 MPa. The simulation using the signal from the scan with no absorbers was redone using a Dirichlet source condition. The resulting peak pressure was 2.52 MPa, 3.7% higher than the measured value. Therefore, using a Dirichlet boundary condition was found to be the simulation method that best described the transducer's pressure profile.

4.4 Pre-focal Simulation of the Field of the Clinical JC-200 Transducer

A simulation of the JC-200 transducer with a radius of curvature of 154 mm was used as a test to check that the selected size of the radial scan line would be sufficient to reconstruct the pressure field of the transducer. The k-Wave simulation was run with a resolution of 6.3 PPW with the pressure recorded at a plane 51 mm pre-focally (103 mm from the rear surface of the transducer). The grid size was 844 x 844 x 844 with the addition of 20 points in each dimension for the PML to give a final grid size of 864 x 864 x 864. The resulting phase and pressure amplitude values at the pre-focal plane were extracted using the FFT. The pressure waveforms were then back propagated 66 mm using the ASM to obtain a source plane defined at 37 mm from the transducer's rear surface.

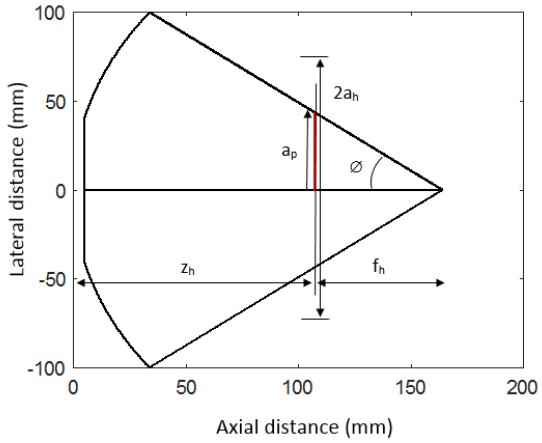

Figure 4.9: Sketch that shows the method used to select the position and size of the pre-focal plane for the characterisation of teh JC-200 transducer. The flat section in the transducer curve is the location of the B-mode probe.

As was done for the H102 transducer the radial line was truncated to match the length of the radial line that would be used in the scan. The length was selected to give a ratio of 3/1 of radial line to beam width at the measurement plane [119]. The calculations for the dimensions, shown in figure 4.9, use the values for radius of curvature 154 mm and the radius of the outside circle of the transducer 100 mm. The measurement plane was a distance of 1/3 the focal length from the focal point, $f_h = 51.3$ mm. The half angle $\phi = \arcsin \frac{100}{154} = 0.71$ rad. The beam width a_p can then be calculated by $a_p = f_h \tan \phi = 44$ mm. The size of the measurement plane was $2a_h = 3 \times a_p = 132$ mm

The value of $2a_h$ is rounded up to 140 mm, 70 mm each side. The truncated radial line, see figure 4.10, was rotated to fill a 2D plane. The resulting plane is back propagated using the ASM to obtain the source plane shown in figure 4.11.

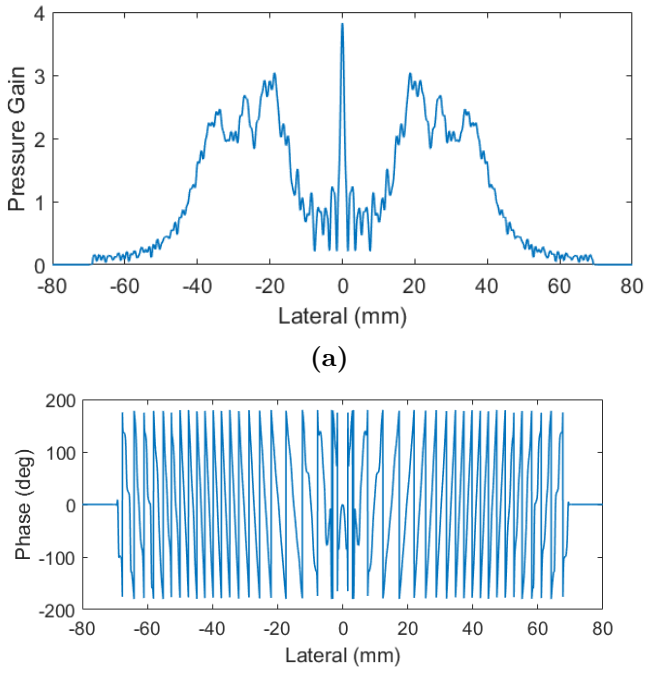

Figure 4.10: The radial line values of amplitude and phase at 0.95 MHz. (a) The pressure gain received at the scan line radially across the face of the transducer. (b) The corresponding phase values

The resulting source plane was then used as a time series pressure source in a k-Wave simulation using an enforced Dirichlet boundary condition. The result

of that simulation was compared with the original simulation's pressure profile. Figure 4.12 shows both axial and lateral pressure profiles of both simulations overlaid. The peak pressure values obtained from the source plane simulation is 1.2% smaller than the original simulation.

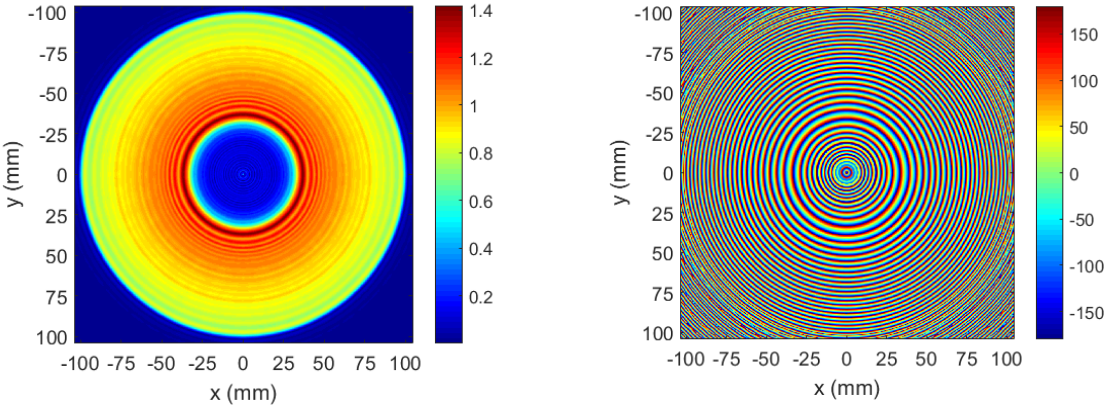

Figure 4.11: Pressure gain (a) and phase (b) at the source plane, 37 mm from the rear surface of the simulated JC-200 transducer, back propagated using AS from the pre-focal measurement plane

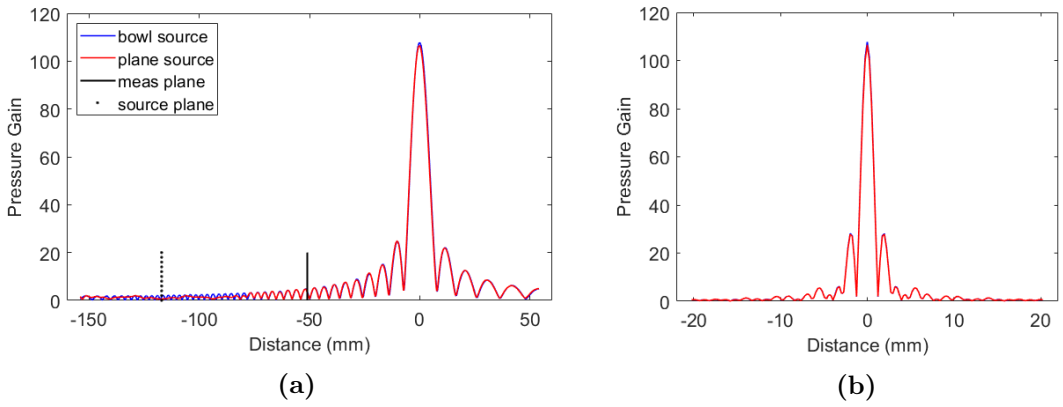

Figure 4.12: The pressure profiles for the simulations from the original simulation defining a pressure source over a bowl surface, and from the ASM back propagation of a pre-focal plane of the simulation. (a) Axial profile, shows the location of the pre-focal plane with the black line and the source plane with the dotted black line. (b) lateral profile limited to the centre 40 mm

Figure 4.13: The HAIFU JC-200 system installed in the Churchill Hospital, University of Oxford

4.5 Platform Design

In order to be able to characterise the JC-200 transducer using a pre-focal scan a positioning system was designed and built to enable radial scans of the JC-200 transducer. This positioning system has to be mounted above the patient bed at the opening where the transducer is located. Figure 4.13 shows the JC-200 system.

A platform was designed to mount the positioning system on the bed and enable the scan of the JC-200 along radial lines. Figure 4.14 shows the CAD drawing and resulting platform. The design of the platform was undertaken using AutoCAD 2016 and it was fabricated by the senior technicians in the IBME workshop. It is composed of three main sections: 2 side rails made from C-channel that are used to fix the platform to the side rails of the JC-200 bed, 2 horizontal pieces that provide the support across the bed, a movable bracket on which the position stages are mounted and 2 segments attached to the C-channels to provide a uniform elevation for the movable bracket. The requirement to cover multiple radial lines across the face of the transducer necessitates moving the stages at different angles.

Therefore, the movable bracket was designed to be positioned at different angles, with 45° spacing, and fixed to the support sections with easy release screws. The position of the threaded holes in the movable bracket correspond to the holes in the position stage to be mounted on the bracket.

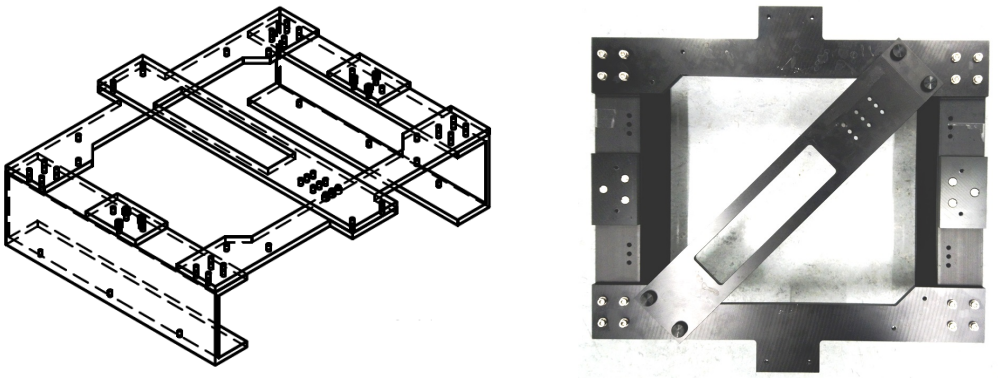

(a) (b)

Figure 4.14: The platform designed to allow the pre-focal scanning of radial lines across the face of the JC-200 transducer, (a) CAD design, (b) photo of the platform. The movable bracket is shown in different positions in (a) and (b)

Figure 4.15 shows the position stages mounted on the platform. The positioning system used included two linear actuators (850G, Newport) with a maximum travel distance of 50 mm and 45 mm. The actuators were controlled by an ESP 300 Motion Controller (Newport Corp., Irvine, CA, USA), which was connected through a serial (RS232) interface to a laptop. The Matlab functions that enabled the interface with the controller were written by Prof. Robin Cleveland. The actuators use stepper motors and have inbuilt optical sensors for positional feedback. The linear actuators were connected to position stages that were cascaded to provide 95 mm of linear motion. Another three manual positioning systems were used for the transverse and elevational directions to allow the accurate positioning of the hydrophone.

4.6 Fibre-Optic Hydrophone Calibration

The hydrophone used to record the pressure at the pre-focal plane was chosen to be a fibre-optic hydrophone (Precision acoustics, Dorchester, UK). The directivity pattern of the fibre-optic hydrophone was measured and compared to an ONDA

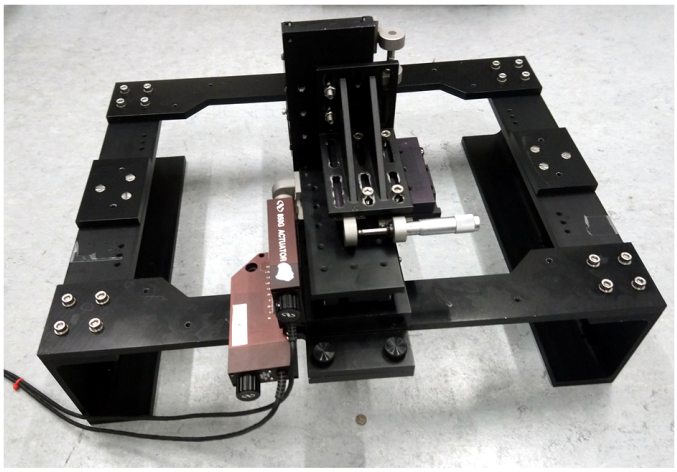

Figure 4.15: The position stage mounted on the designed platform.

needle hydrophone HNA-0400's directivity pattern in the range from 0° to +90°. The measurement was undertaken by recording the focal pressure of an H102-35E transducer with the hydrophone positioned at different angles within the field. To translate the previous graphs into numbers that can be used to select the best position, the BPAP and BPPD were calculated. Figure 6.8 shows the plots of the BPAP and BPPD plotted in relation to the transducer's angular position for patient 1. The values for BPAP and BPPD compensated for staircaising effects are overlaid with the non-compensated values. Figure 4.16 shows the graphs obtained from the measurements compared with the theoretical value using the equation.

$$D(\Theta) = \frac{2J_1(ka_0 \sin\Theta)}{ka_0 \sin\Theta} \tag{4.3}$$

where $J_1(.)$ is the first-order Bessel function, k is the wavenumber, and a_0 is the radius of the hydrophone sensing element surface. This equation assumes a circular piston in a rigid planar baffle and results in a broader directivity pattern than measurements for values of ka < 2.5 [125].

The fibre-optic hydrophone is less directionally sensitive than the ONDA therefore it was a better choice for the scan. Another important reason for the choice of the fibre-optic hydrophone is that it is cheaper to replace if damaged by the high pressures generated by the JC-200 transducer. As will be described in section 4.7.2 the hydrophone was indeed damaged due to the high pressures generated at the focal point of the transducer.

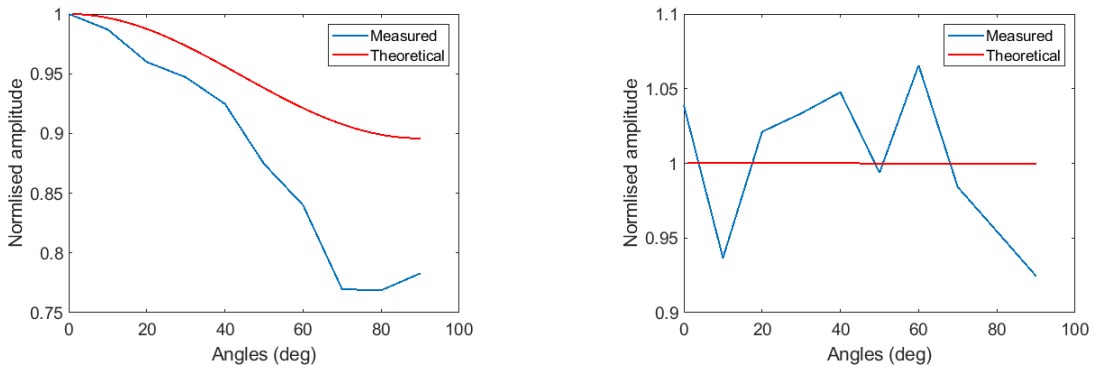

Figure 4.16: The theoretical and measured directivity patterns from 0° to 90° for (a) ONDA HNC-0400, (b) fibre-optic hydrophone.

The fibre-optic hydrophone's output voltage was calibrated and found to be similar to the manufacturer's calibration. The reference hydrophone for the calibration of the fibre-optic hydrophone was the ONDA needle hydrophone HNC-0200 (ONDA Corp., Sunnyvale, CA) connected with an amplifier AH2020 with 20dB amplification. The calibration was undertaken by measuring the focal pressure of the H102D-28 (Sonic Concepts, Dorset, UK) which was driven at 1.0 MHz using a signal generator (33220A, Agilent Technologies, Santa Clara, CA, USA) and an amplifier 1140LA (ENI, Rochester, NY, USA). The transducer was driven at voltages from 4.7V to 48 V measured at the output of the power amplifier. The pressure calibration for the ONDA hydrophone was used to obtain the corresponding pressures of 0.17 MPa to 1.6 MPa. A linear fit was used to obtain the calibration for the fibre-optic hydrophone with a slope value of 206.6 mV/MPa. The manufacturer's supplied calibration was 217 mV/MPa. Figure 4.17 shows the relationship of the pressure value to the voltage output of the fibre-optic hydrophone.

4.7 JC-200 Pre-focal measurements

The pre-focal scans were undertaken on 3 separate days on the JC-200 system and were conducted in collaboration with Dr. Michael Gray. A Matlab script running on the laptop controlling the positioning system's linear actuators was used to synchronise the stepping of the position stages with the signal acquisition from a

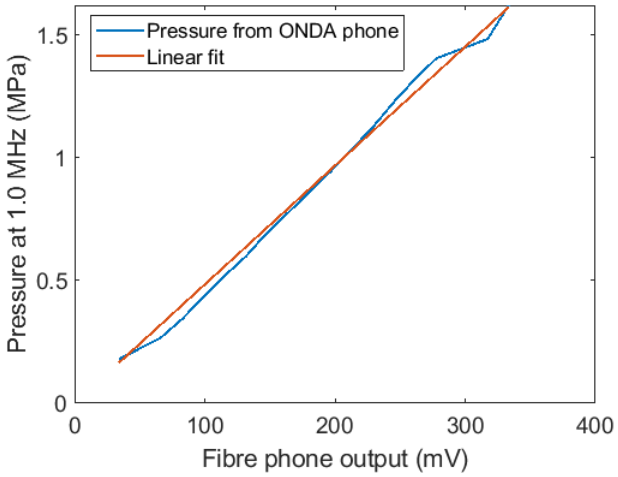

Figure 4.17: The calibration graph for the fibre-optic hydrophone (FP 129-10) obtained with a reference measurement from the ONDA HNC-0200

scope. The scope used was a HDO4024 WaveSurfer (Teledyne LeCroy, Chestnut Ridge, NY, USA) with an interface to Matlab using functions that were written by Prof. Robin Cleveland. Two hydrophones were used, one was a 200 μm needle hydrophone, (NH0200, Precision Acoustics, Dorchester, UK), connected through a pre-amplifier, DCPS586 (Precision Acoustics, Dorchester, UK), and a low pass filter to channel 1 of the scope. This hydrophone was positioned at the rim of the transducer's bowl to provide the trigger signal for the acquisition, described in section 4.7.1. The other hydrophone was used to capture the radial scan signal, it was a fibre-optic hydrophone sensor, FP129-10 (Precision Acoustics, Dorchester, UK), connected through a fibre-optic hydrophone control unit (Precision Acoustics, Dorchester, UK) to channel 3 of the scope. The setup is shown in figure 4.18 and the trigger hydrophone can be seen in the photo in figure 4.19.

During the experiment the JC-200 system was driven at three different power levels of 75 W, 150 W and 200 W. The pulse repetition frequency was fixed at 10Hz with a duty cycle of 25% for all power levels.

4.7.1 Trigger Set-up

The JC-200 system does not provide an external trigger that can be used as a time reference for measuring acoustic signals. Further complications for the signal

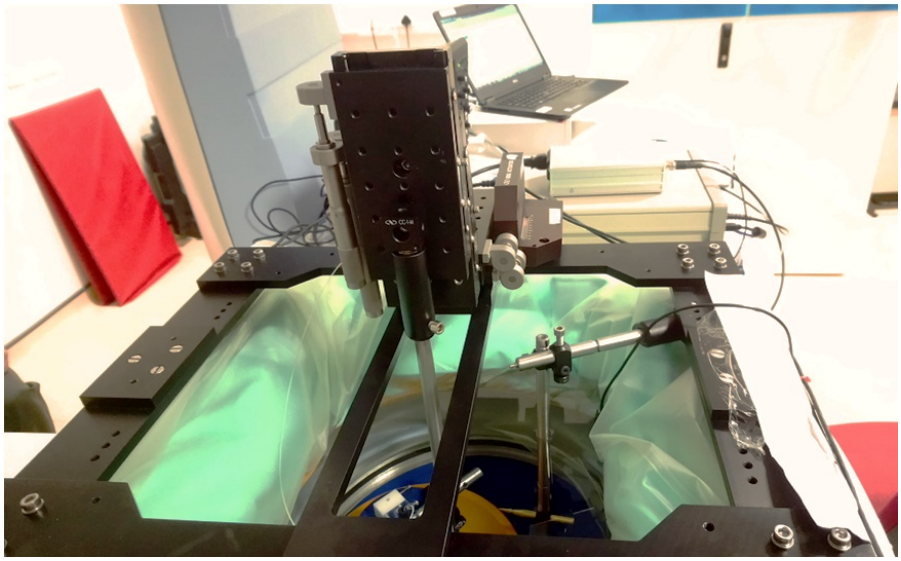

Figure 4.18: A photo of the setup for the pre-focal scan of the JC-200 transducer. The designed platform is shown connected to the patient bed. The positioning system mounted on the platform has the scanning hydrophone connected. The trigger hydrophone is mounted at the side of the platform. The laptop and Newport control unit used to drive the linear actuators are shown in the background.

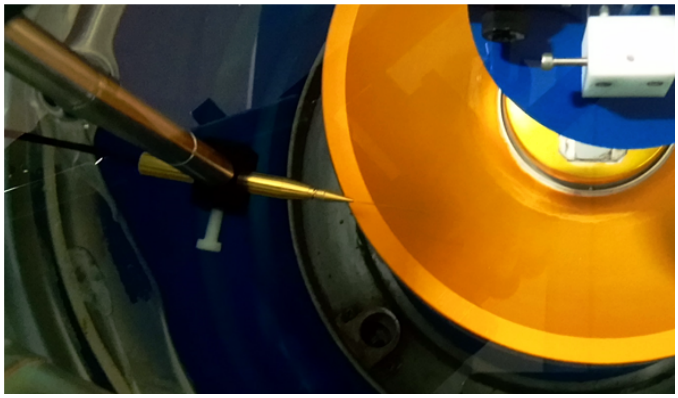

Figure 4.19: The position of the trigger hydrophone at the rim of the JC-200 transducer. The hydrophone is used to provide the time reference required to obtain phase information from the scan signal.

acquisition resulted from the presence of electrical noise on the order of the acoustic signal picked-up on the hydrophone signal connected to the scope's trigger. The scope was set up to capture a 200 ms signal at a sample rate of 12.5 MS/s. In order to enable triggering from the hydrophone signal the trigger settings were selected as 'qualified A & B with edge trigger' on channel 1. A two event trigger set-up was used to increase the likelihood of a valid signal being captured. Event A sets the trigger to arm with Event B triggering signal acquisition. Both events were set to occur on

the rising edge of the signal with a threshold above a specified value. Because of the 10Hz PRF used for the JC-200 signal a wait time of 100 ms was set before Event B would be enabled. The threshold for the edge triggers for A and B was adjusted according to the power level at which the scan was undertaken. For example, at 75W, keeping the threshold above 10 mV resulted in a very long acquisition time since the level was not sufficient to trigger at every instance during the scan. However, when the threshold was dropped to 9.4 mV many erroneous triggers were obtained due to the presence of a periodic noise signal that was hypothesised to be an electrical signal pick up from the B-mode on the JC-200 system. Because when the experiment was undertaken the ultrasound scan was set-up to use the hand-held probe attached to the system. At one time the B-mode probe in the centre of the JC-200 was covered with an acoustic absorber, which did not eliminate nor reduce the signal. Figure 4.20 shows both a valid trigger and an erroneous one. The broadband signal was present even with the insertion of a low pass filter with a pass band specified up to 1.9 MHz (BLP-1.9+, Mini-Circuits, Brooklyn, NY).

4.7.2 Pre-focal pressure scans

The set-up for the pre-focal scans is shown in figure 4.21, which gives a graphic representation and a photo taken during the experiment. Two acoustic absorbers were placed behind the fibre-optic hydrophone tip in order to minimise reflections from the metal brackets and water surface. The front absorber was HAM A (Precision Acoustics) and the back one was Aptflex F28P (Precision Acoustics). The front reflector was used as well as the back one, because the F28P reflector can cause specular reflections.

The first step in obtaining the radial scans was finding the focal point of the transducer. The JC-200 system power was set at the minimum value of 32 W. To position the hydrophone at the focal point both the transducer and the hydrophone were moved. The movement steps for the transducer are not as accurate or as fine as those enabled by the position stages connected to the hydrophone. Therefore, the JC-200's movement system was used to provide centimetre resolution whereas

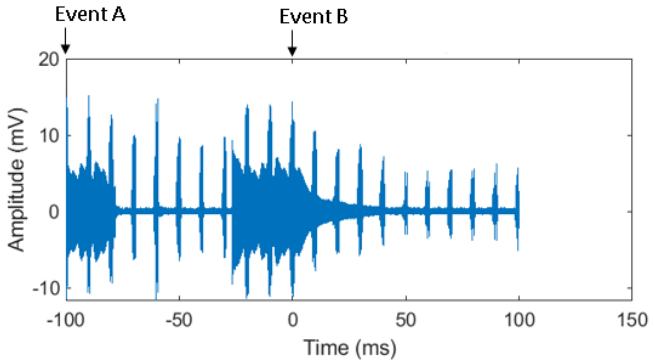

(a) Valid trigger signal

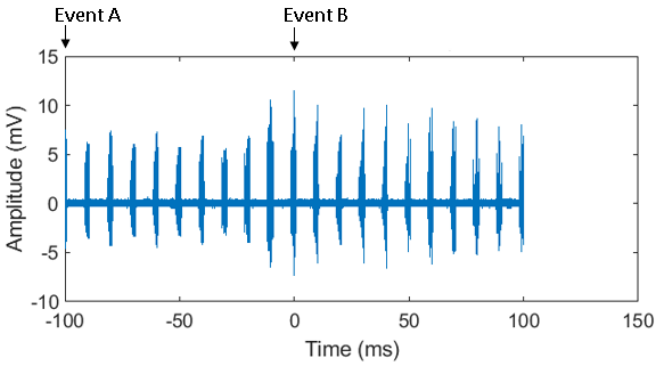

(b) Noise signal

Figure 4.20: Plots showing the waveform recorded at the trigger channel from: (a) a valid transducer signal, (b) an erroneous signal from electric noise pick up.

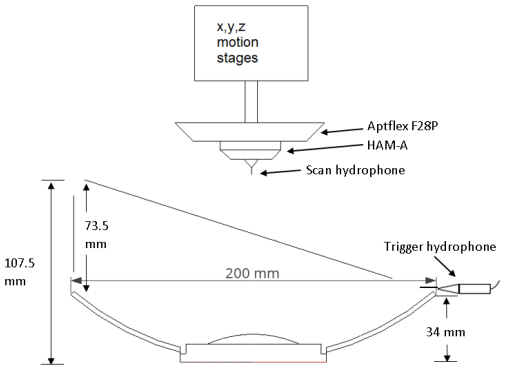

(a)

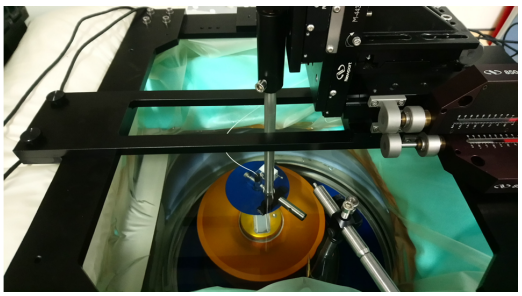

(b)

Figure 4.21: The setup for the pre-focal scan. (a) Sketch, (b) Photo of experiment

the manual and the software controlled position stages mounted on the JC-200 bed were used for finer movement.

To find the focal point in the axial direction the transducer and positioning system were moved until an approximate point was found by placing the tip of the fibre-optic

hydrophone at the marked focal point on the B-mode image, see figure 4.22.

The fibre-optic hydrophone was then moved to find the focus in the horizontal plane using a Matlab script to control the position stages and record the movement on the manual stage. The script would plot a 2D graph of the voltage recorded by the hydrophone. The fibre-optic hydrophone used stopped producing a signal after a value of 1.67 V was recorded, which corresponds to approximately 9.3 MPa. It was replaced with another hydrophone which was also damaged after recording a value of 1.9 V, 8.8 MPa. It was then concluded that the high pressure at the focal point must have created cavitation at the tip of the fibre-optic hydrophone damaging it irreparably.

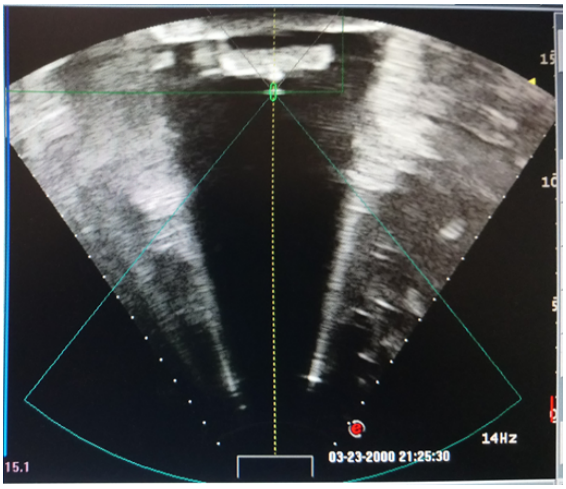

Figure 4.22: A photo of the JC-200 system's screen showing a B-mode image where the fibre-optic hydrophone is seen at the centre of a mark where the focal point is highlighted

Since finding the focus by using time of flight was not possible due to the absence of a readily available trigger signal from the JC-200 drive, the B-mode image, seen in figure 4.22, was used to define the axial position for the focal point. The fibre-optic hydrophone was then moved 51 mm pre-focally for the pre-focal scans to be undertaken. To determine the focus in the horizontal pre-focal plane the centre of the B-mode beam in the elevational direction was found. Since the B-mode probe was coaxially aligned with the JC-200 transducer finding the centre of the B-mode elevation profile would give a good approximation of where the JC-200's focal point was in the horizontal plane. The fibre-optic hydrophone was scanned

across the elevational dimension of the probe, with the centre of the resulting curve obtained by selecting two points at the side of the curve that were at similar values. The B-mode probe was then rotated 90° to present the elevational dimension to the other axis on the plane and the same method was used to find the centre in the new axis. Figure 4.23 shows how the centre of the pre-focal plane was found for the 75 W power setting. The plot in figure 4.23(a) was the scan in the x axis and the plot in figure 4.23 was in the y axis after the probe was rotated by 90°.

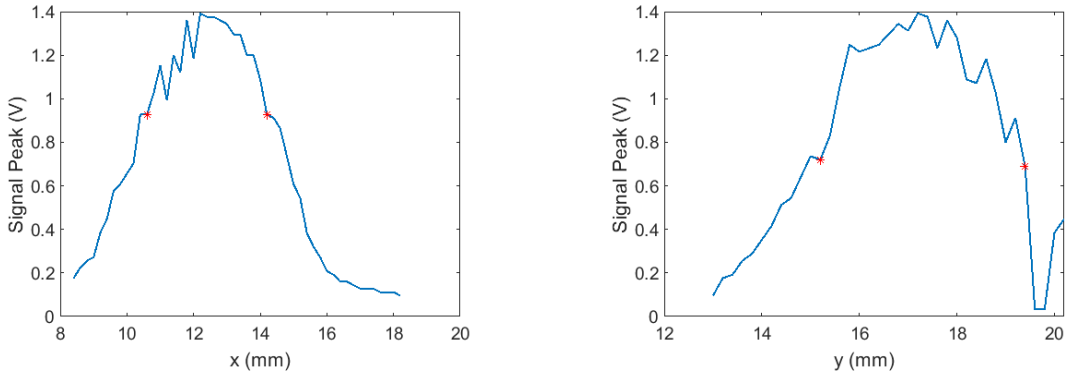

(a) (b)

Figure 4.23: Finding the focus using the profile of the B-mode C5-2 probe that is coaxially aligned with the JC-200 transducer. (a) Linear scan in x dimension with points manually selected to give edge of elevation profile, (b) Linear scan in the y dimension - after the probe was rotated at 90°

The previous alignment using the B-mode probe was undertaken before every radial scan. In total 7 scans were completed. To locate the centre of the B-mode probe the power of the B-mode probe was increased by setting the mechanical index (MI) to 1.3. Before all the pre-focal radial scans the MI was reduced to 0.5. A depiction of the location of the scans is shown in the diagram in figure 4.24. Scan 1 and 2 were undertaken at two power levels 75 W and 150 W. Scan 3 was also undertaken at two power levels 150 W and 200 W. Scan 4 was undertaken at only 150 W. The JC-200 system was activated manually for each acquisition and set to produce 3 bursts with 10Hz PRF and 25% duty cycle.

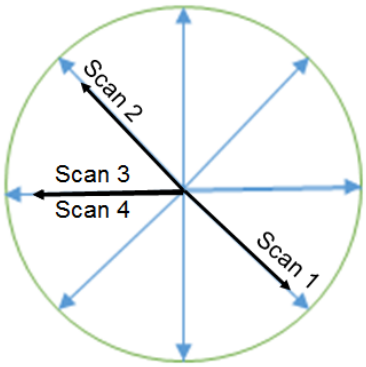

Figure 4.24: A diagram showing the relative radial scan locations.

4.8 Pre-focal signal analysis

The first step in extracting the phase and amplitude at 0.96 MHz from each scan was to align all the signals in time. This was necessary because the trigger method used did not provide the required microsecond accuracy. Figure 4.25 shows two signals recorded from scan 2 at 75 W, it demonstrates a 10 ms offset between the signals.

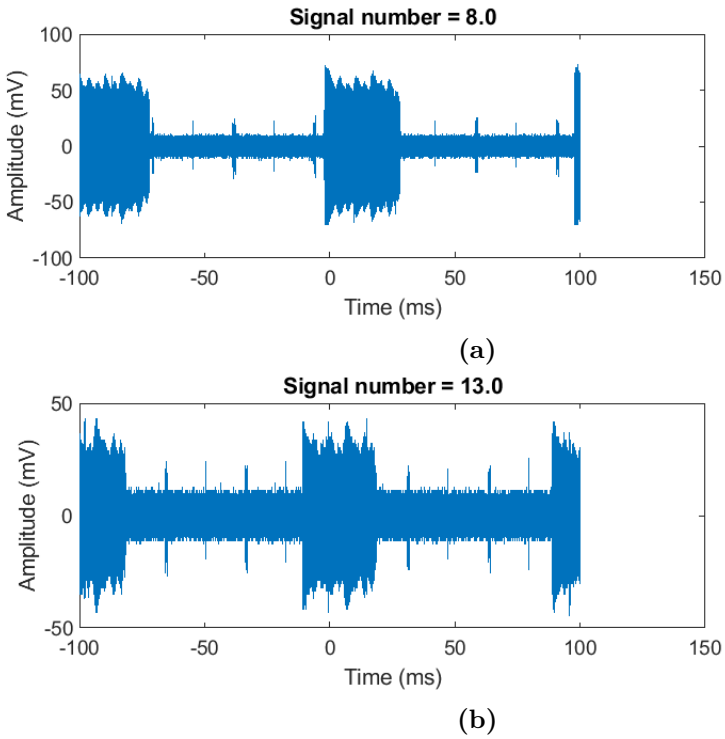

Figure 4.25: The trigger signal recorded by the trigger hydrophone at the rim of the transducer during the pre-focal scan at 150W. The signals in (a) and (b) are shifted relative to each other by nearly 10 ms.

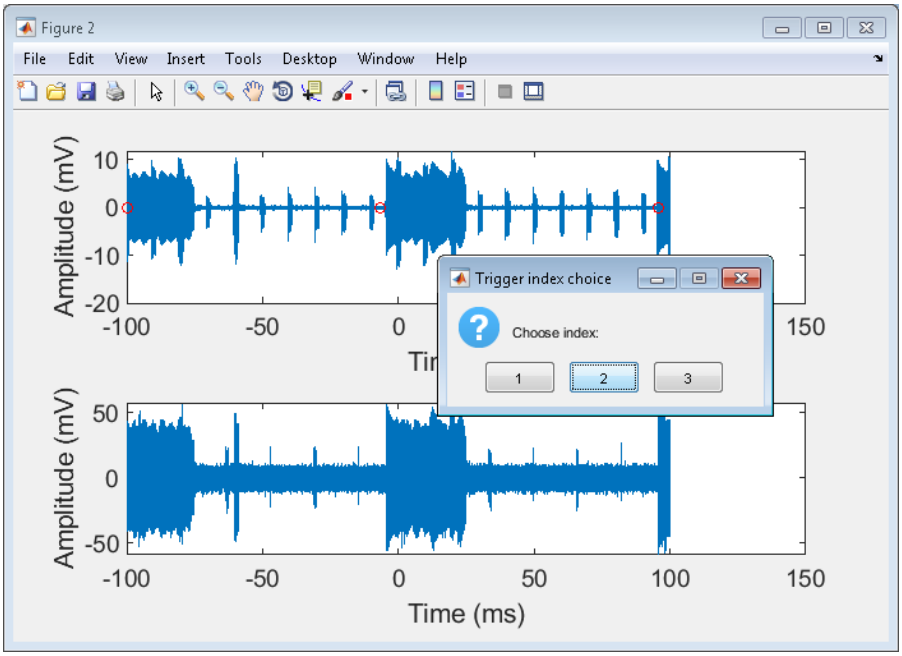

Figure 4.26: The selection of the trigger signal section. The red circles show the positions at the start of the longest sections within the trigger signal. The dialogue box was used to manually select one of the red circle positions. The other signal in the bottom section of the figure is the corresponding acoustic signal from the scan hydrophone.

First the location of the acoustic signal of interest has to be selected from within the 200 ms recorded signal. A script that selects the longest signal envelope written by Prof. Robin Cleveland was modified to find the longest three signal segments within the recorded signal and the best one was selected manually. Figure 4.26 shows the interface used to undertake this selection, it shows that index 2 was the default selection, since this was the central signal and was mostly the best choice.

Another manual selection stage was used to improve the alignment of the signal before cross-correlation. The start index from the envelope detection was set at the centre of a 40 ms segment from the trigger signal. A new index was automatically selected from within this section chosen at 1 ms before the position of the half maximum signal. Then this was displayed in a figure to confirm or modify the index manually. Figure 4.27 shows the selection method for the index with the default index selection displayed with a red circle. An updated index can be selected with the cursor.

Cross-correlation was then used to find a finer time alignment of the trigger

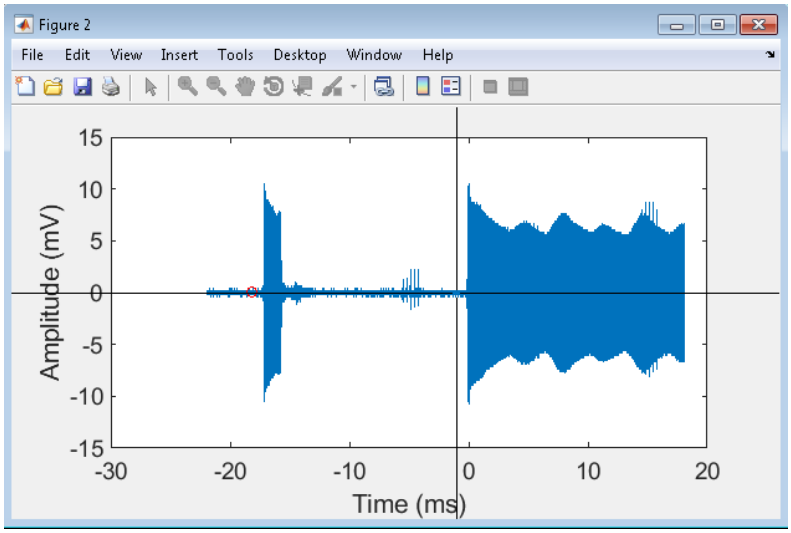

Figure 4.27: The selection for the start of the relevant trigger signal section. The red circle shows a default selection with the cursor showing the ability to modify it. The signal is from scan 4 at 150W

signals. The first recorded signal of each scan was the reference for all the other trigger signals of the scan. The cross-correlation was undertaken twice to obtain a close time alignment. For the first, coarse, cross-correlation a segment length of 0.5 ms was used. The segments were divided into two sections in order to pass the first section across the whole signal to find the Pearson's linear correlation coefficient at each step. Both the reference signal and compared trigger signal were moved across the other. The highest correlation coefficient value was selected as the best alignment position. Figure 4.28 shows the result of the cross correlation for one of the signals obtained during scan 4.

The second, fine, cross-correlation stage involved the same process, but the length of the signal segments were reduced to 0.2 ms. Figure 4.29 shows the same signal of figure 4.28 put through the second cross-correlation stage. Once the time alignment had been accomplished the relative phase values can be extracted from the signals. The amplitude and phase values at the centre frequency of 0.96 MHz were extracted from the signal using the FFT.

The axial position of the hydrophone was defined based on the B-mode image shown in figure 4.22. To perform the pre-focal scan the fibre-optic hydrophone was moved from this point 51 mm pre-focally. The B-mode image defines the

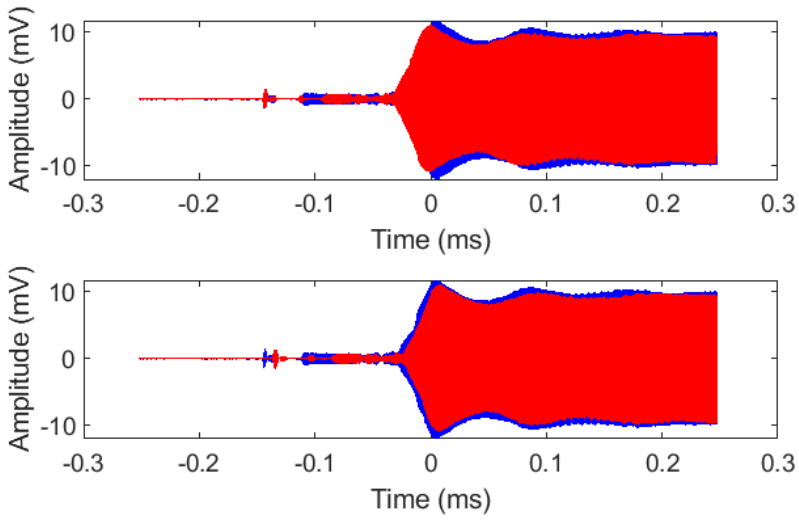

Figure 4.28: The result of the coarse (first stage) cross-correlation for two trigger signals, the reference signal is in blue. Upper graph shows the signals before cross-correlation, bottom one shows the red signal shifted to be in alignment with the reference.

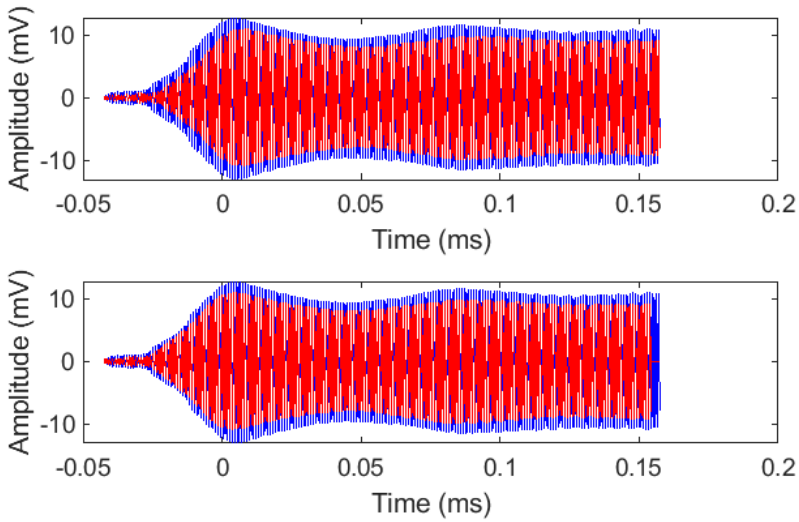

Figure 4.29: The result of the fine (second stage) cross-correlation for two trigger signals, the reference signal is in blue. Upper graph shows the signals before cross-correlation, bottom one shows the red signal shifted to be in alignment with the reference

distance from the time of flight information based on the speed of sound used in the JC-200 system which is 1540 m/s. However, the temperature of water during the experiment was 22°C at which the speed of sound is 1488 m/s. Therefore, a correction of the recorded distance needs to be undertaken. The calculation for the corrected distance, assuming a focal distance of 164 mm can be obtained by:

$\frac{0.164\times1488}{1540} = 0.1585$ m. This calculation is approximate and could be out by 2 mm since estimating the position from the B-mode image is not exact.

The depth of the transducer's bowl is calculated using the radius of curvature and the transducers outer diameter, recall figure 4.21(a), using: $164-\sqrt{164^2-100^2} = 34$ mm. Since the hydrophone was moved towards the transducer by 51 mm this puts it at a distance of $158.5 - 51 - 34 = 73.5$ mm from the rim of the transducer. The longest travel distance would be from the edge of the opposite rim to the hydrophone and can be calculated using the diameter and distance to the rim: $\sqrt{200^2+73.5^2} = 213$ mm which has a corresponding travel time of 143 μs. Therefore, the first 200 μs was not included in the steady state segment. The length of the segment was chosen to be 150 μs, which gave a frequency resolution of 6.7 kHz.

The extracted phase and amplitude at the fundamental frequency of 0.96 MHz are shown in figures 4.30 to 4.34 for scans 1 to 4. The values in the locations where an erroneous trigger happened were marked and replaced by interpolated values using linear interpolation from the neighbouring values.

The phase oscillation pattern seen in the radial scans up to 40 mm in figures 4.30 to 4.34 show a similar pattern to that seen for the JC-200 simulation radial graph shown in figure 4.10. Beyond a distance greater than 40 mm of the scan the clear phase pattern begins to break down. Here the signal is lower so the noise will have a bigger impact on the extracted phase and amplitude. The frequency analysis shows how the relative value of the 2nd harmonic is bigger than the fundamental in this section of the scan, see figure 4.37 and 4.38.

At the start of scan 1 at a power of 75 W 42 signals (8.2 mm) were acquired with a voltage per division setting that caused signal clipping. This resulted in the first 8.2 mm section for scan 1 in both phase and amplitude having a different shape to that obtained with scan 1 at 150 W.

Scans 1, 2 and 3 are on the same pre-focal plane so a similarity in the shape of the graphs for phase and amplitude is expected particularly in the region up to 40 mm where the pressure amplitude is highest. The start of the phase signal for scans 1, 150 W and scan 3 is the same, see figure 4.32. For scan 2 it appears

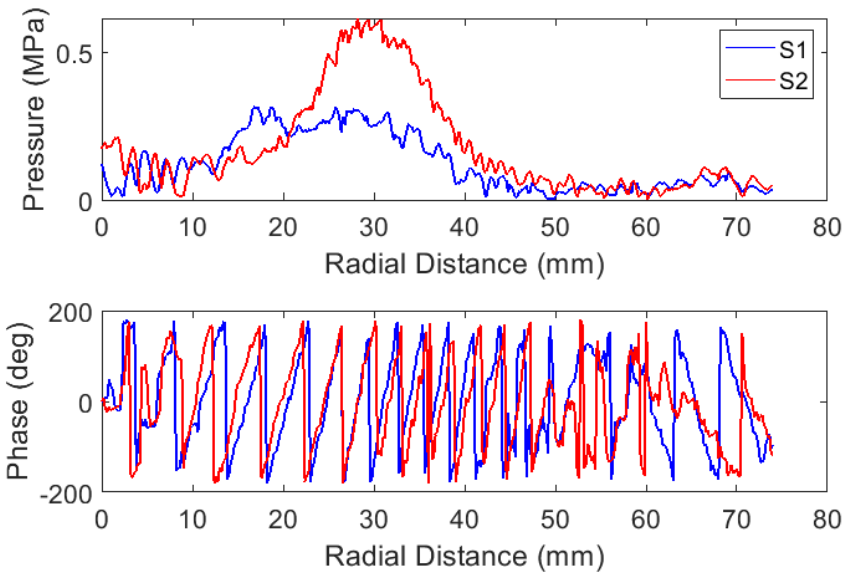

Figure 4.30: The radial amplitude and phase obtained for scan 1 and scan 2 at 75 W, scan 1 is in blue with scan 2 in red.

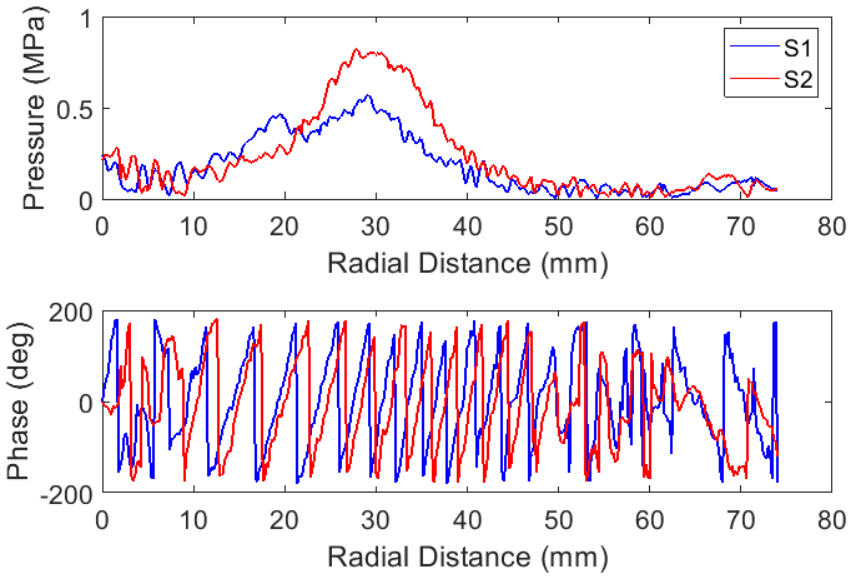

Figure 4.31: The amplitude and phase obtained for scan 1 and scan 2 at 150 W, scan 1 is in blue with scan 2 in red.

that this phase signal is shifted to the right by approximately 2 mm, see figure 4.31. However, the shape of the amplitude extracted is different for all the scan locations, with each radial location 1, 2 or 3 displaying a unique beam shape that is followed for both the scans undertaken at different power levels.

A scan was also undertaken at position 3 using a 200 W power setting, to

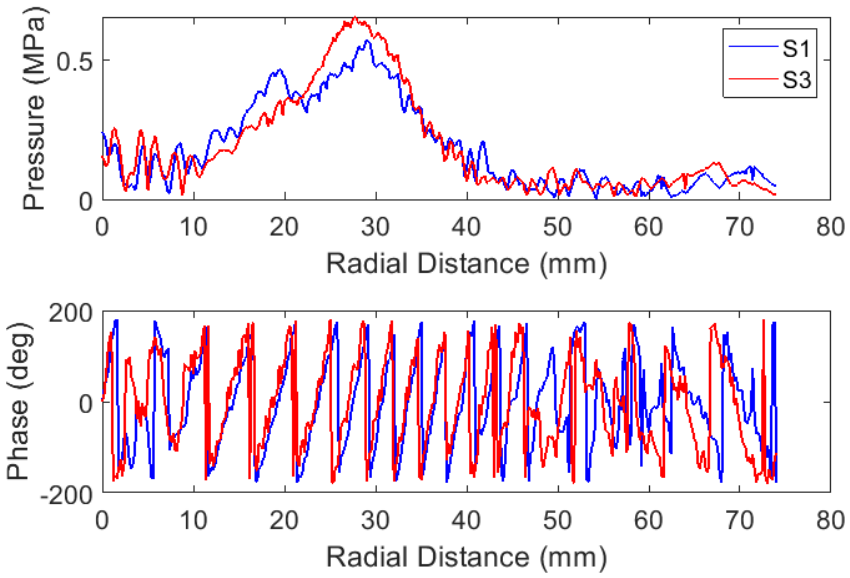

Figure 4.32: The amplitude and phase obtained for scan 1 and scan 3 at 150 W, scan 1 is in blue with scan 3 in red

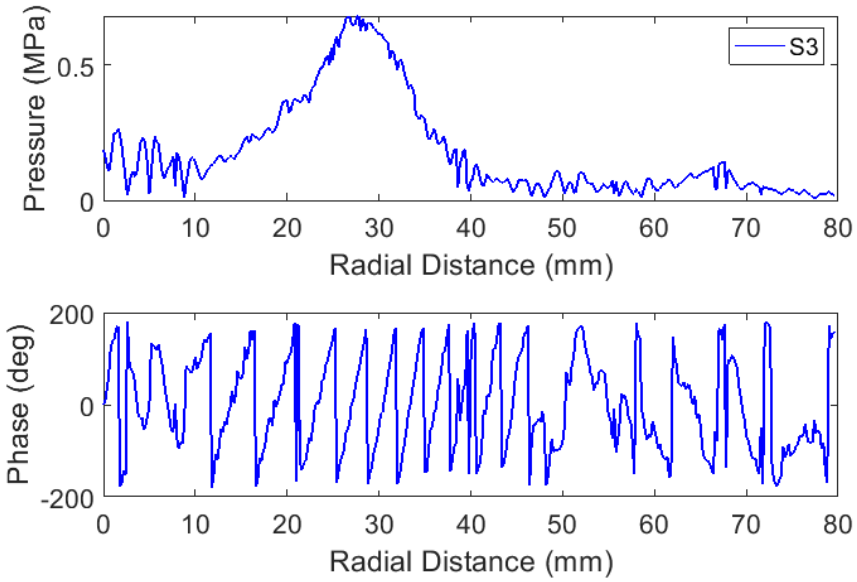

Figure 4.33: The amplitude and phase obtained for scan 3 at 200 W

compare the pressure values across three power levels and check the impact of increasing the power on the frequency content. Figure 4.33 shows the amplitude and phase at 200 W for scan 3, which follow the graphs from scan 3 at 150 W closely.

Scan 4 was taken at a plane 10 mm towards the focus from the plane of scan 1, 2 and 3. The extracted amplitude and phase extracted from the scan's signals

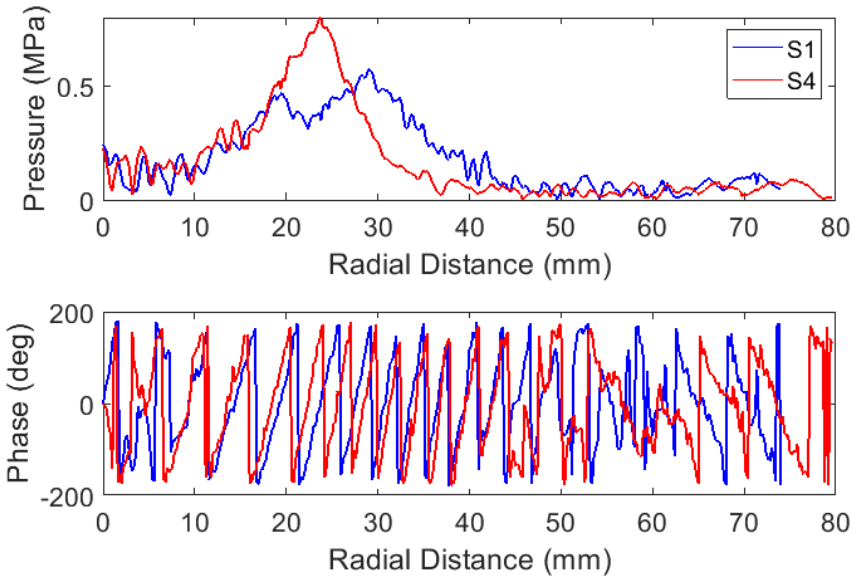

Figure 4.34: The amplitude and phase obtained for scan 1 and scan 4 at 150 W, scan 1 is in blue with scan 4 in red. Scan 1 is 56.5 mm pre-focally.

are shown in figure 4.34. The beam width is much smaller for scan 4, which agrees with its position closer to the focal point.

Scan	Plane position (mm)	Peak pressure (MPa)	- 6dB width (mm)
Scan 1, 75 W	107.5	0.315	24.6
Scan 1, 150 W	107.5	0.572	19.2
Scan 2, 75 W	107.5	0.616	14.8
Scan 2, 150 W	107.5	0.825	14.0
Scan 3, 150 W	107.5	0.653	15.4
Scan 3, 200 W	107.5	0.681	14.2
Scan 4, 150 W	117.5	0.798	8.2

Table 4.1: The maximum pressures and width of the half pressure points for all pre-focal scans

Table 4.1 shows the -6 dB pressure widths and peak pressures obtained for each scan. Scan 1 at 75 W has the smallest pressure value followed by scan 1 and scan 3 at 150 W. Then scan 3 at 200 W has a higher pressure than at 150 W. The values for maximum pressure obtained at scan 2 are not consistent with the previous trend. The maximum pressure from scan 2 at 75 W is higher than that obtained from scan 1 at the double power of 150 W and is only 6% less than

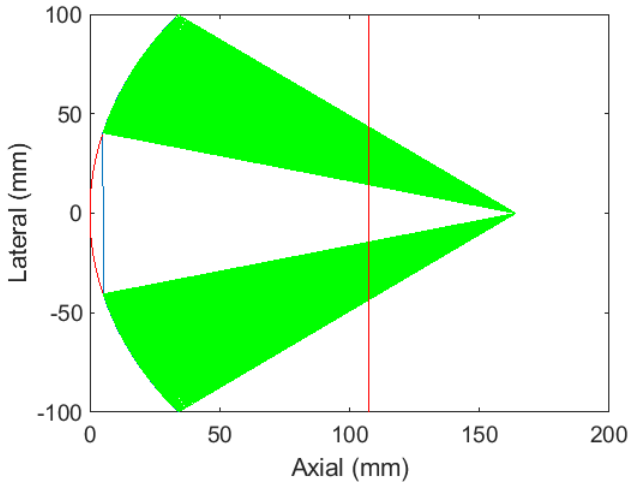

Figure 4.35: Ray trace for the JC-200 transducer with a radius of curvature of 164 mm. The red line represents the measurement plane.

maximum from scan 3 at 150 W. The pressure value at 150 W for scan 2 is also higher than for scan 4 which does not reflect the pressure values anticipated due to scan 4 being closer to the focal point by 10 mm. The maximum pressure from scan 4 is higher than those for scan 1 and scan 3 which reflects the position of their corresponding planes within the pressure field.

The radial scans with the widest beam width are the measurements for scan 1 at 75 W and 150 W. They more closely resemble the expected pattern from the transducer's geometry. Figure 4.35 sketches the geometry of the source and indicates that the width of the ultrasound beam, based on geometrical acoustics, at the plane 107.5 mm from the rear surface of the bowl is 29 mm. The simulation result in figure 4.10 shows a 22.7 mm beam width which is also closer to values for scan 1.

The frequency components of the signals were analysed looking specifically at the second harmonic and comparing it across the different scans. The method used to obtain the pressure amplitude at the second harmonic involved finding the maximum value at a range of ±20kHz around 1.92 MHz to account for finite window effects that were noted in the spectrum in the shift of the maximum signal to adjacent frequency bins, see figure 4.36.

The manufacturer's calibration was used to obtain the pressure values at the second harmonic. Figures 4.37 and 4.38 show the plots for the second harmonic

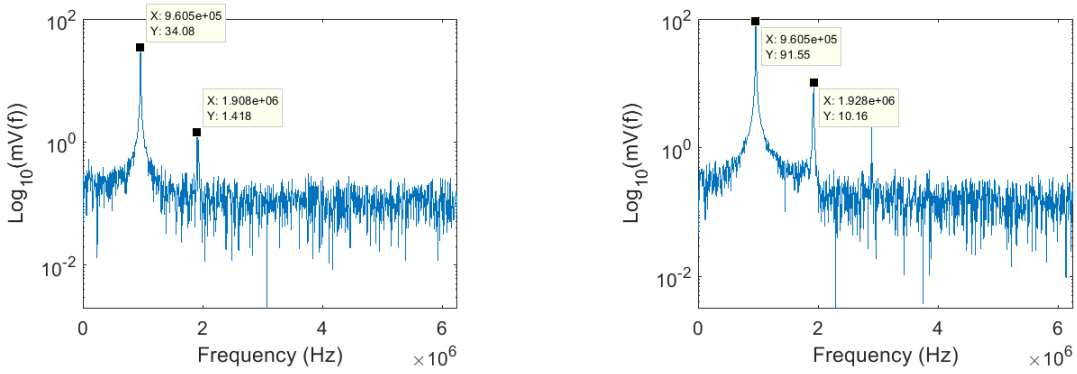

(a) (b)

Figure 4.36: The frequency analysis for signals from scan 1 at 150 W, plotted on a semi-log scale

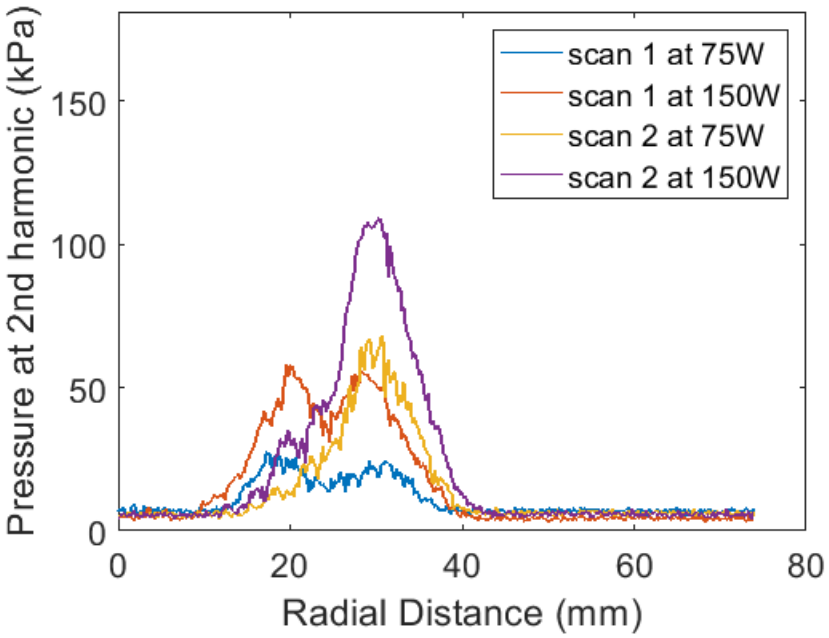

Figure 4.37: The pressure extracted at the second harmonic for the radial scans 1 and 2 at 75 W and 150 W

component of the signal. Figure 4.37 shows the results of scan 1 and scan 2 at 75 W and 150 W. It shows that the value of the second harmonic component for the signals recorded at a power of 150 W is double the value of the second harmonic obtained at 75 W for both scan 1 and 2. This is consistent with the expected ratio for weak nonlinear propagation [126].

The peak pressure values for the second harmonic and the fundamental for the

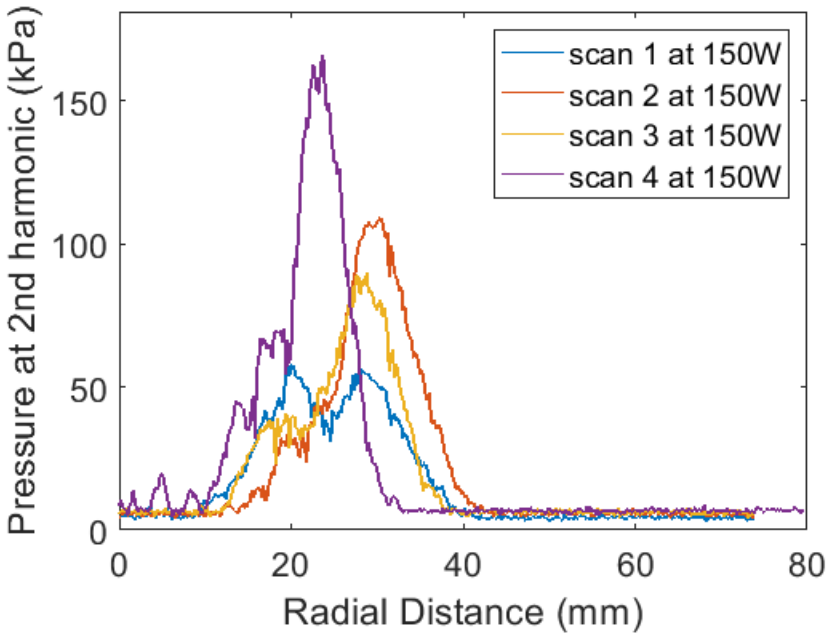

Figure 4.38: The pressure extracted at the second harmonic for the radial scan 3 at 150 W, 200 W and scan 4 at 200 W compared to scan 1 at 75 W

Scan	Peak Fund (MPa)	Peak 2nd harmonic (MPa)	Ratio Percent.
Scan 1, 75 W	0.315	0.027	8.6%
Scan 1, 150 W	0.572	0.058	10.1%
Scan 2, 75 W	0.616	0.031	5.0%
Scan 2, 150 W	0.825	0.109	13.2%
Scan 3, 150 W	0.653	0.09	13.8%
Scan 3, 200 W	0.681	0.133	19.5%
Scan 4, 150 W	0.798	0.166	20.8%

Table 4.2: The maximum pressures at the fundamental and second harmonic frequencies for the pre-focal scans. As well as the percentage ratio of the peak second harmonic value to the peak fundamental value.

scans are listed in table 4.2. The table shows the ratio of the second harmonic to the fundamental. For scans 1 and 2 the ratio varies from 5% to 13% with scan 1 showing the smallest ratio for 150 W and scan 2 showing the smallest ratio for 75 W. The second harmonic values for scan 1, 2 and 3 at 150 W follow the order for the fundamental values from low to high respectively. But the ratio for the scans show a slight increase in scan 3 compared to scan 2.

Figure 4.38 shows the second harmonic components for the scans at 150 W. Scan

4, which was undertaken at a position that was 10 mm nearer the focus than the other scans, shows the highest value for the second harmonic. This was anticipated since nonlinearity will increase with the longer propagation distance and narrowing of the beam nearer the focus. The resulting ratio, see table 4.2, shows that the second harmonic signal's value was 20% the value at the fundamental, which is a doubling of the percentage obtained at the same power for scan 1. The other scan with a similar ratio of second harmonic to fundamental of 19.5% was the radial scan 3 undertaken at the higher power of 200 W.

4.9 Back Propagation Pressure Profile Results

The amplitude and phase extracted from the scans were rotated to complete a 2D plane as was done in the simulation results in section 4.4. The ASM was then used to back propagate this plane to a location 3 mm in front of the rim of the transducer, 37 mm from the rear surface of the bowl. Figure 4.39 is a plot of the resulting 'source' plane that was obtained for scan 1 at a power setting of 150 W.

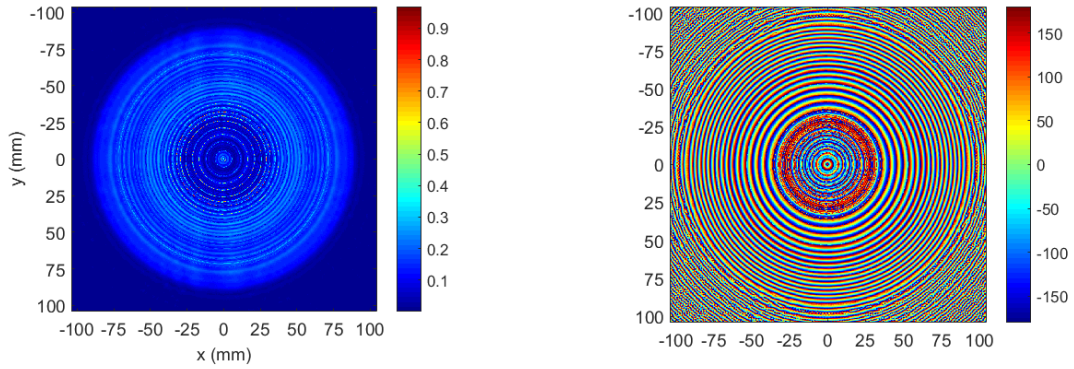

(a) **(b)**

Figure 4.39: The plane resulting from the ASM back propagation of the measurement plane, (a) pressure amplitude (MPa), (b) phase in degrees

To use this resulting source plane in a k-Wave simulation the values of amplitude and phase were interpolated from the 0.2 mm resolution of the scan to 0.2467 mm resolution for the k-Wave grid. The source plane was used as a time varying source input to simulate the transducer's field in a homogeneous non-attenuating

medium with the sound speed of water at 22°C, 1488 m/s, to match the condition at which the scans were undertaken.

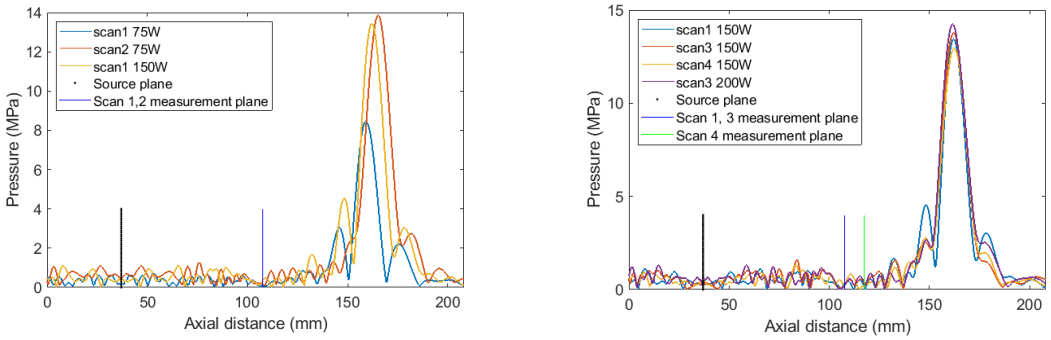

Figure 4.40: The axial pressure profile resulting from k-Wave simulations using the back propagated planes obtained from a few different radial scans at different power settings. The black vertical lines show the location of the measurement plane at 107.5 mm and the back propagated source plane at 37 mm.

Six of the seven radial scans were simulated with the axial pressure results shown in figure 4.40. Four of the scans are similar in the position of the focal location with a focal point between 161 mm and 162 mm as listed in table 4.3. The focal pressure values for scans 1 and 3 at 150 W are 3% different. The simulation for scan 2 at 75 W gives a focal pressure value that is higher than the focal pressure from scans 1 at 150 W and a similar value to that from scan 3 at 150 W. The focal pressure for scan 4 at 150 W is 3% lower than the pressure for scan 1 at 150 W. From figure 4.40 the shape of the profile obtained at scan 1, for both power levels, shows the expected shape of nulls at the side lobes more closely than do the axial profiles from the other scans. The positions of the nulls are more pronounced for scan 1.

The focal pressure value obtained from scan 1 at 75 W was approximately 8.5 MPa, which is consistent with the pressure value at 150 W. This value is 1 MPa lower than the result of the pressure calculated using the pressure at 150 W, $\sqrt{\frac{75}{150}} \times 13.5\text{MPa} = 9.5$ MPa, assuming a fixed power pressure conversion ratio.

Scan	Focal pressure (MPa)	Axial focal distance (mm)
Scan 1, 75 W	8.5	159.1
Scan 1, 150 W	13.5	161.8
Scan 2, 75 W	13.9	165.0
Scan 3, 150 W	13.8	161.6
Scan 3, 200 W	14.3	161.3
Scan 4, 150 W	12.9	162.1

Table 4.3: The maximum pressures and width of the half pressure points for all pre-focal scans

4.10 Discussion

The characterisation of the JC-200 clinical transducer was achieved by performing radial pre-focal scans at different power inputs as full 2D scans were not feasible. The reconstructed pressure profile of the transducer from the radial scans was different for each of the scans. Scan 1 at 150 W, scan 3 at 150 W and scan 3 at 200 W are the closest in giving a focal point falling between 161 mm and 162 mm: whereas, scan 2 at 75 W and scan 1 at 75 W give focal points at 165 mm and 159 mm respectively.

The focal pressures resulting from the radial scans 1, 3 and 4 at 150 W show less than 7% variation, which was deemed acceptable. The resulting focal distance values obtained from these scans were different by 0.5 mm. On the other hand scan 2 shows a 39% increase in pressure at 75 W compared to scan 1. The value of 13.85 MPa is higher than focal pressures at 150 W from scans 1, 3 and 4. The radial scan at 150 W for scan 2 was not simulated because it was showing a similar big amplitude difference of approximately 31% to the other scans measured at the same pre-focal plane, scans 1 and 3.

Another aspect noted from the amplitude and phase values over the radial scans was that there was a similarity in the amplitude shape between scan 2 and scan 3 which was different to the wider amplitude shape seen in scan 1. Since scan 2 was at 180° rotation from scan 1, and scan 3 only 45° from scan 2 this shows the possibility that the transducer is not symmetric or that the transducer could be tilted with respect to the scan plane. Although, the lack of agreement in pressure suggest that it might be due to the approximations in finding the focal position.

Radial scan 3 was extended beyond 74 mm to 79.6 mm when scanned at a power of 200 W. This did not cause a marked change in the shape of the resulting pressure profile, which would appear to indicate that the selected side length of the measurement plane was sufficient to cover the ultrasound beam passing through. The choice of the length of the scan had already been verified from simulations.

It was difficult to obtain a full representation of the transducer's field of view because of the small sections scanned. Since the radial scans across different parts of the face of the transducer show distinct shapes, this would indicate the asymmetry of the transducer field. When the same scan was undertaken for the H102 transducer the pressure amplitude and phase obtained along two radial lines were similar.

A better method of scanning would use a motion stage that can cover a longer scan of 148 mm across the focal point to obtain the complete radial line from one end of the transducer to the other. Scan 1 and scan 2 would have been captured in one continuous scan. This would better show the shape of the pressure distribution across the face of the transducer.

According to the simulations undertaken by Sapozhnikov et al [119] errors in the axial and focal plane pressure values and in the beamwidth of the reconstructed field would be less than 1% if the hydrophone used had a sensing element with a diameter $< \frac{\lambda}{4}$. Therefore, using a fibre-optic hydrophone with a diameter of 10 μm clearly satisfies the condition at 0.96 MHz where $\lambda = 1.5$ mm. Therefore, the errors that are specific to the JC-200 transducer's scan setup can be restricted to the position of the hydrophone and the quality of the selected section of the recorded signal.

The radial scans rely on the focal point being found precisely. Positioning the hydrophone in the centre of the pre-focal plane was done by obtaining an approximate centre for the B-mode array. This can cause errors of a few millimetres. Indeed it was noted that the start of the amplitude and phase for radial scan 2 appeared to be shifted by 2 mm from the other scans. The axial position was also specified by using a manual assessment of where the hydrophone was on the B-mode image, which could be out by 2 mm. Another geometric misalignment that results in errors in the pressure profile is the orientation of the scan plane

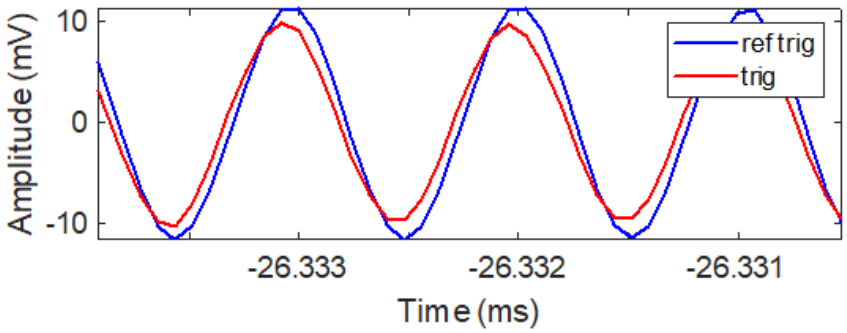

Figure 4.41: A zoomed in plot of two trigger signals from scan 1 at 150 W, which show that the time difference between the reference trigger signal and a trigger signal from another point on the scan after cross-correlation is less than one step size (80 ns).

relative to the beam axis. This was found to result in errors in the pressure profile of 10% at an misalignment of 0.4° [119]. For a 2D measurement plane the relative orientation of the measurement coordinates and the beam axis can be obtained from the position of the focus of the field projected from the measurement plane. When using a radial line measurement this is not possible since the 2D plane was derived by rotating this line to obtain a symmetric plane.

The time alignment for the scan lines was good at finding the overlap of the signals. However, due to the discrete time samples of the signals there could be a time difference of less than a sample (80 ns). This can be seen in figure 4.41. This could result in a phase error of up to 27° which would have an impact on the resulting pressure profile.

Also, the section selected from the recorded trigger signal did not provide a steady amplitude across the section for all recorded signals. Some lower amplitude signals showed oscillations. This was most likely due to noise or reflections.

In the future, as a means to improve the alignment for the focal point a small 2D plane around the focal point could be scanned. This would also help to determine if there was symmetry across the transducer's surface.

Discrepancies in the temperature recorded can also cause resulting pressure errors. A variation of ± 1°C was found to result in errors $< 1\%$. For the previous scans the variation in the temperature recorded did not exceed 1°C. A thermometer was used to record the temperature of the water manually at the start of the scans.

More accurate temperature acquisition could be undertaken with a thermocouple recording unit. Then the temperature could be recorded at the start and the end of the experiment from the Matlab script eliminating human error in forgetting to record the temperature immediately before or after the scan.

4.11 Conclusion

A transducer characterisation method was implemented that used measurements from only pre-focal radial scans of the transducer. The resulting radial scans were rotated to provide a 2D plane that was back propagated using ASM projection to create a source plane. This plane was used as a pressure source in k-Wave to simulate the pressure field for the transducer in a homogeneous non-attenuating medium.

The method was tested first on a smaller research transducer, the H102. The results obtained gave a pressure profile that followed the lateral and axial scans of the transducer. The focal pressure was 3.7% higher than the measured one.

The method was then used to obtain the pressure field for the JC-200 clinical transducer. The extracted amplitude and phase values across the radial scan had different shapes for each scan. This indicated that either the transducer was asymmetric or that there was a misalignment of the scan plane and the source's acoustic axis. The pressure profiles obtained for each simulated scan gave varying results for the maximum pressure at the focal point and its location. The position of the focal point for three scans was at a range between 161 mm - 162 mm. The other two scans resulted in values of 159 mm and 165 mm. Whereas, the expected value for the focal distance was 164 mm. These differing values for the JC-200 transducer was in contrast to validation studies carried out on the H102 transducer. This was attributed to the uncertainties associated with finding the focal point at the pre-focal plane, the quality of the pressure signal recorded by the hydrophone, uncertainties in the time alignment of the trigger signals and challenges in selecting the steady state section from the signal.

5 Patient-Specific Models

The aim of this chapter is to apply a computational model built with k-Wave to understand the outcomes from a clinical trial for HIFU ablation of kidney tumours. Linear simulations were conducted using 5 CT scans from patients who underwent HIFU treatment as part of a clinical trial run in the University of Oxford's Churchill Hospital. Thirteen patients were recruited to that trial with 10 treated [75]. Of the 9 CT scans found only 5 had the complete patient geometry out to the skin surface and these were used for the acoustic simulations. In what follows they are referred to by the simulation number shown in table 5.1. The table also details the outcome of the HIFU ablation for each patient using the percentage of tumour ablated, the state of the CT scan found and the position of the tumour.

5.1 Acoustic Simulations

The transducer used in the model was one used in the clinical HIFU system JC-200 (Haifu, China). It has an outside diameter of 200 mm, a circular cut-out with a 60 mm diameter and a radius of curvature of 145 mm. It was driven with a frequency of 0.95 MHz. A linear simulation was undertaken with a resolution of 6.3 PPW. The volume for the simulation was selected from the segmented CT scan and was a cube of 208 mm x 208 mm x 208 mm. The CT scan grid was usually anisotropic, with the

Simulation patient number	Trial ID	Trial ablation percentage	State of CT scan	Tumour location
1	5.39	70%	complete	Right, lower
2	5.13	<5%	complete	Left, interpolar
3	5.01	95%	complete	Left, upper
4	5.10	<5%	complete	Right, interpolar
5	5.29	0%	complete	Left, interpolar
N/A	5.16	95%	N/A	Right, lower
N/A	5.21	95%	truncated	Right, lower
N/A	5.23	60%	truncated	Right, lower
N/A	5.38	60%	truncated	Left, lower
N/A	5.03	0%	truncated	Left, interpolar

Table 5.1: The CTs of the patients treated on the kidney ablation clinical trial. The CT scan for patient 5.16 was not found.

slice thickness larger than the in-slice pixel spacing. The CT scan was interpolated, using nearest neighbour, onto an isometric grid for the simulation, with a spatial resolution of 246.7 μm. The resulting grid size was 864 x 864 x 864 voxels which includes 10 pixels of a perfectly matched layer (PML) around all boundaries.

For simulation 5 two CT scans were available with different pixel spacing and slice thickness. One had 0.625 mm pixel spacing and 0.625 mm slice thickness, but was truncated at the left side of the abdomen, while the other had 0.703 mm pixel spacing and a 5 mm slice thickness with a complete abdomen view. The finer resolution CT scan was truncated at the side of the abdomen with the treated kidney. Therefore, in order to use this finer resolution CT scan in the simulation the missing section was patched using the lower resolution CT scan. Figure 5.1 shows a slice at a corresponding location in both CT scans and the patched result. This patch was present in every 8^{th} slice of the composite 3D image. To create the full 3D volume a linear interpolation was used to complete the external surface for the remaining in-between slices.

Using a CFL value of 0.15 and a maximum speed of sound of 4080 m/s, the temporal resolution was 9 ns. The simulation length of 243.6 μs was chosen to cover the k-Wave grid diagonal length of 360.6 mm, resulting in 26,867 time steps. The simulations were run using the University of Oxford's Advanced Research

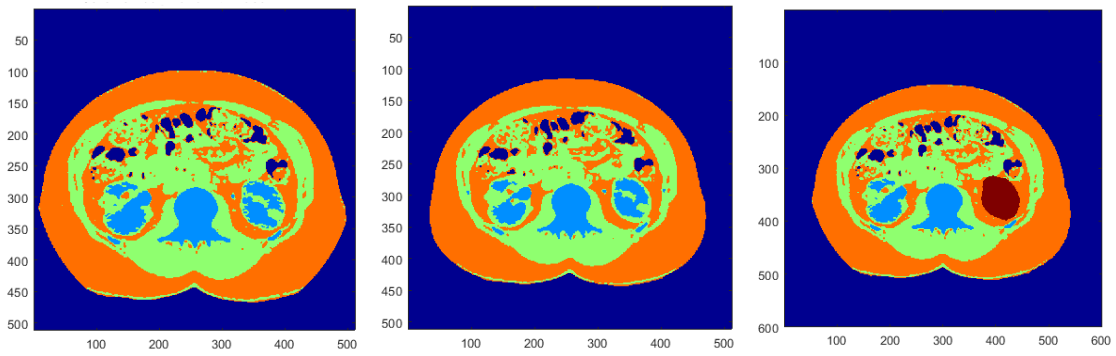

Figure 5.1: CT slices for simulation 5, (a) truncated slice from higher resolution CT scan, missing section of abdomen at the patient's left side (right on CT image) (b) complete slice from lower resolution CT scan, (c) higher resolution slice in (a) completed on the side of the treated kidney using slice in (b) shown with the kidney segmented

Computing (ARC) cluster, using the run environment setup by Visa Suomi. On average they took approximately 53 hours on 144 processors (9 cores x 16 tasks). For simulations 1, 2 and 4 the time-domain pressure waveforms were recorded for a volume of 34 mm x 26 mm x 20 mm around the focal point as well as for the axial, coronal and sagittal planes. For simulation 3 the maximum and minimum pressures were recorded over a bigger volume of 95.2 mm x 126.5 mm x 106.6 mm and for simulation 5 over a volume of 70 mm x 111.5 mm x 106.6 mm. A bigger volume was used in simulations 3 and 5 in order to record the pressure around the ribs which were in the HIFU beam path.

The method for positioning the transducer with respect to the tissue volume was through manually choosing the shortest acoustic path within the tissue. The chosen CT volume was rotated to enable the positioning of the focal point at the target tumour, the resulting position may not be the same as the patient's position during the clinical trial. For patients 3 and 5, whose rib cage lay in the ultrasound propagation path, the patient CT scans were rotated to a position where there would be a gap to enable B-mode imaging. Figure 5.2 shows the position of the transducer for the 5 patient models simulated, it was placed in the same location within the grid for all simulations.

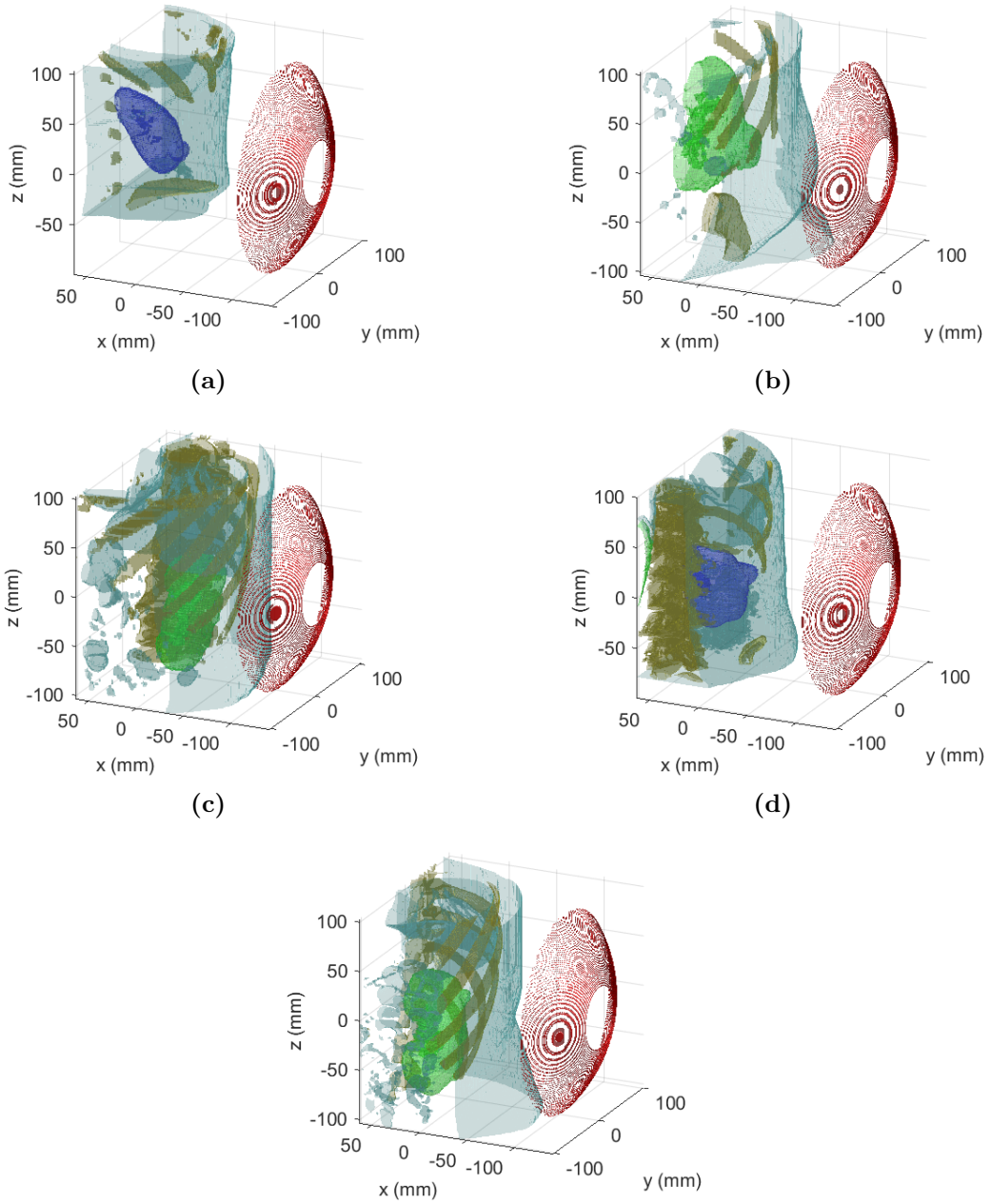

Figure 5.2: The CT transducer position relative to the medium derived from patient CT scans from a HIFU kidney ablation clinical trial [73]. Five patient simulations were undertaken. (a) Patient 1, tumour is on the right kidney, lower lobe, with a maximum dimension of 18 mm. (b) Patient 2, tumour is on the left kidney, interpolar, with a maximum dimension of 38 mm. (c) Patient 3, tumour is on the left kidney, upper lobe, with a maximum dimension of 15 mm. (d) Patient 4, tumour on the right kidney, interpolar, with a maximum dimention of 28 mm. (e) Patient 5, tumour is on the left kidney, upper lobe, with a maximum dimension of 30 mm

A second simulation was undertaken for patient 3 with the lung segmented. This was done because on viewing the results of the simulation it was apparent that the lungs were in the path of the ultrasound beam and the lungs had been given the properties of water in the first simulation. It is necessary to point out that the position of the lung in the CT scan is not necessarily where it was during the HIFU treatment. In order to reduce the respiratory movement on the kidney during the treatment endotracheal intubation was used to isolate the lung at the side of the targeted kidney tumour. Also, where necessary the isolated lung was either inflated or deflated to provide a window for the B-mode probe in-between the ribs [75]. For this specific patient it was not possible to find a record for the procedure followed during the treatment or any B-mode images. Also the CT scan was taken with the lungs in a natural state. Acoustic properties for the lung were obtained from Dunn [127] measured on a partially deflated lung, these were 976 m/s for speed of sound, 700 kg/m^3 for density and 13.9 dB/cm attenuation at 1 MHz. The deflated lung values were selected because they presented the best case scenario for ultrasound delivery through the lung. The grid step size of 246.7 μm was maintained resulting in a reduced points per wavelength value of 4.2 within the lung segment.

The k-Wave Matlab toolbox was used to provide the input file for the simulation that defines the source, sensor and time grids and the medium properties with the simulation carried out using the C++ k-Wave implementation on the ARC cluster.

5.1.1 Acoustic Simulation Results

A Matlab script was used to plot the pressure results for each patient simulation. The pressure from the simulation was normalised by the source pressure to find the pressure gain. Figure 5.3 displays the results of the pressure gain in the axial focal plane for all 5 patients. There are two results for patient 3, the second simulation result with the segmented lung is referred to as 3*. All patient results were overlaid on the CT patient geometry to show how well the focal point coincides with the tumour location.

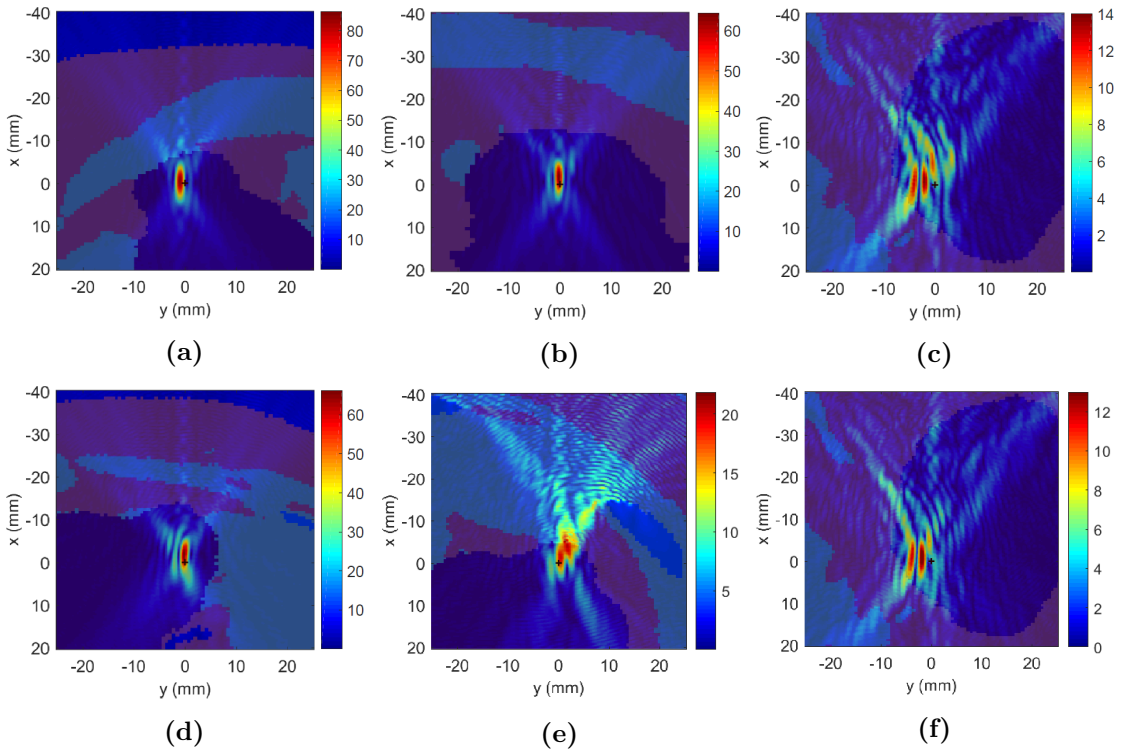

Figure 5.3: The axial plane showing the pressure gain overlaid on the tissue structure for each of the simulations on (a) Patient 1, (b) patient 2, (c) patient 3, (d) patient 4, (e) patient 5 and (f) patient 3* (with segmented lung). Tissue colours correspond to: dark red for kidney, red for fat, green for muscle and dark blue for water. The pressure gain is overlaid with the colour bar showing the value. The HIFU focal point target location is marked with a black cross

The focal point is within the targeted tumour in patients 1, 2 and 4 and the focus is well defined without apparent fragmentation. For simulation 3, 3* and 5 the situation is different with the focus fragmented. The fragmentation of the focus for patient 3 and 3* resulted in two focal spots approximately 4 mm apart.

The fragmentation of the focal region can be viewed better in figure 5.4 which shows the iso-surface for the half pressure (-6 dB) volume for all the patients. No fragmentation has occurred in the volumes from the patients 1, 2 and 4. However, for patient 3, 3* the fragmentation seen in the axial plane is more apparent with no main segment and numerous scattered smaller fragments. For patient 5 there is fragmentation mainly pre-focally with the furthest section forming a single volume.

Table 5.2 shows the effects of patient geometry on the pressure field. The parameters compared are the maximum gain (ratio of the highest pressure to the

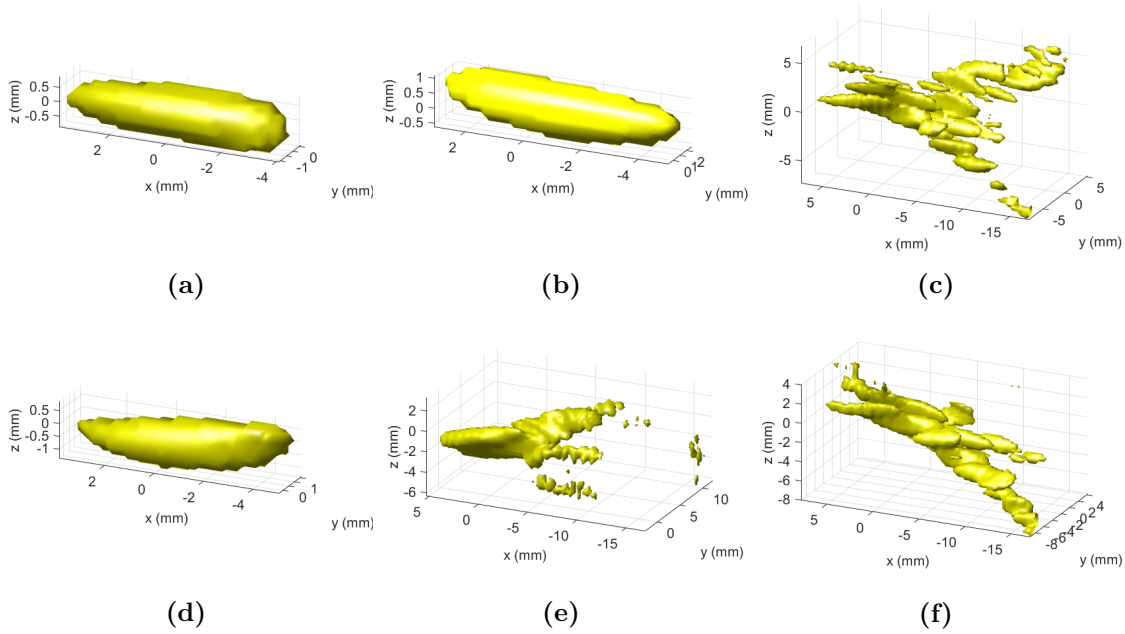

Figure 5.4: The iso-surface of -6 dB focal volume for the simulations of (a) patient 1, (b) patient 2, (c) patient 3, (d) patient 4, (e) patient 5 and (f) patient 3* (with lung segmented)

Simulation ID	Maximum Gain	Gain at Target	Shift (mm)				Width (mm)		
			x	y	z	R	x	y	z
1	86	52	-0.25	-0.74	0	0.78	7.89	1.73	1.73
2	68	58	-1.48	0	-0.25	1.5	8.14	1.73	1.73
3	17	5	-0.25	-1.73	-0.49	1.82	N/A	N/A	N/A
3*	15	4	-0.74	-1.97	-0.25	2.12	N/A	N/A	N/A
4	73	59	-0.99	0	0.49	1.10	7.89	1.73	1.97
5	29	16	-0.74	1.48	1.48	2.22	N/A	N/A	N/A

Table 5.2: The results of the simulations showing the pressure gain at the maximum pressure point in the simulation, the pressure gain at the target focal point, the shift from the target point to the maximum pressure point and the half pressure (-6 dB) volume width. x is the axial dimension, with y and z the lateral dimensions. R is the euclidean distance.

source pressure), gain at target (ratio of the pressure at the target to the source pressure), focal point shift (distance between the highest pressure and the target focal location) and the width of the half pressure (-6 dB) volume. Simulations 1, 2 and 4 have tight well-formed focal regions as seen in figure 5.4. These half pressure contours have widths that are very similar and are within 0.2 mm of each other. However, the peak pressure achieved in patient 1 is nearly 20% higher than that in

patients 2 or 4. There is an increased shift in the position of the achieved focal point for simulations 2 and 4, however, values of 1.5 mm and 1.10 mm are small with respect to the tumour dimension and the treatment would normally cover a margin of healthy tissue surrounding the tumour that is no less than 1 cm [66, 91, 128].

The fragmentation observed in the results for patients 3 and 5 can be explained by the fact that the HIFU is delivered through the ribs [129]. The rib cage is in-between the transducer and the kidney tumour being treated. As can be seen in figure 5.5 with a zoomed out image of the axial plane for both simulations, there is significant reflection at the tissue bone interface. However, there is less fragmentation in patient 5, since the propagation path is shorter and the area where there is rib interference is smaller.

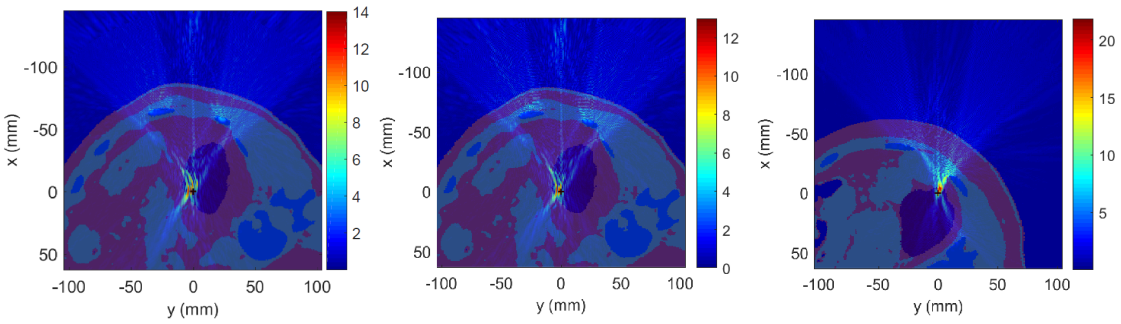

Figure 5.5: The axial focal plane for: (a) patient 3, (b) patient 3* (with segmented lung), and (c) patient 4. Tissue colours correspond to: dark red for kidney, red for fat, green for muscle, blue for bone and dark blue for water. The colour bar shows the pressure gain. The HIFU focal point target location is marked with a black cross

Simulation 3* using partially deflated lung properties resulted in a 12% reduction in maximum pressure from simulation 3. From figure 5.4(f) the fragmentation of the focal volume is still apparent. The effect of lung in the simulation for patient 3 can be viewed in another plane, the xz plane where the lung is visible as shown in figure 5.6. The result of simulation 3 shows the ultrasound beam passing through the material with water properties in figure 5.6(a). The effect of the lung as a barrier to transmission is apparent in figure 5.6(b).

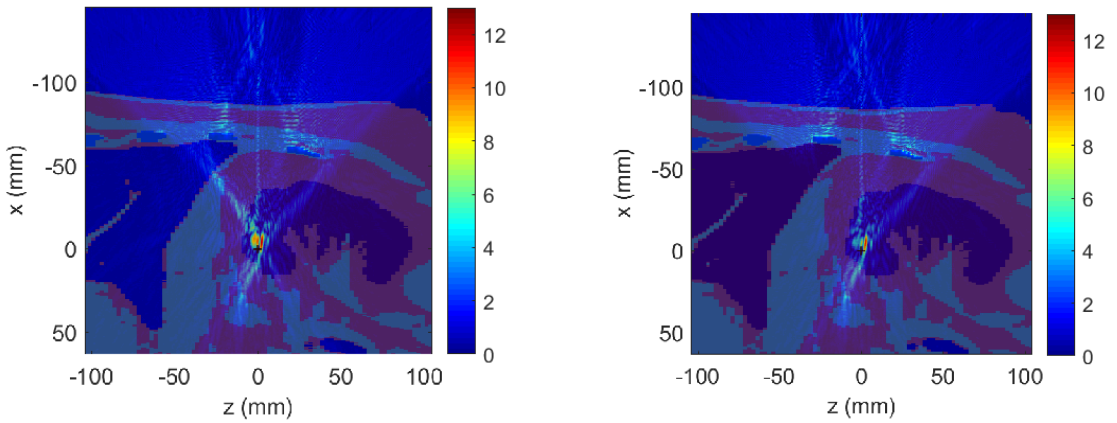

Figure 5.6: The lateral focal plane for: (a) patient 3, (b) patient 3* (with segmented lung). Tissue colours correspond to: dark red for kidney and lung, red for fat, green for muscle, blue for bone and dark blue for water. The colour bar shows the pressure gain. The HIFU focal point target location is marked with a black cross

5.1.2 Patient 1 transducer re-positioning

The transducer position used for patient 1 in the previous results was obtained by manually selecting a rotation that would give the ultrasound beam a short path within the tissue. However, this does not match the position at which the patient was treated. B-mode images were acquired during the treatment using the C5-2 probe, which is coaxially aligned with the HIFU transducer and located in the circular cutout. A B-mode image from which a transducer orientation could be estimated was identified and used to reposition the transducer in the simulation relative to the patient's CT scan. Figure 5.7 shows the B-mode image taken during the treatment along with a segmented CT slice that has been rotated to mimic the B-mode position. Another simulation is undertaken using this modified orientation.

This second simulation is referred to as $1^{\dagger}$ to differentiate it in subsequent analysis from the first one. The results show that the achieved peak pressure using this position is 24% lower than for the first one, with a resulting maximum pressure gain of 65. As can be seen from figure 5.8 there is partial fragmentation occurring in the -6 dB pressure iso-surface plot.

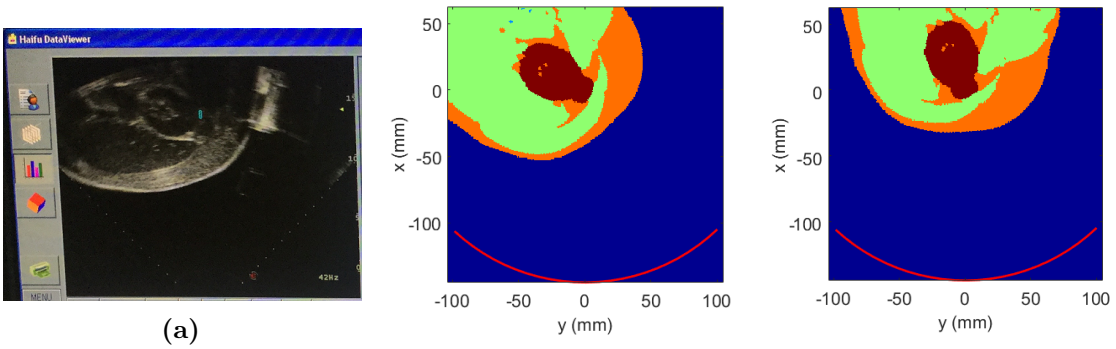

(a) (b) (c)

Figure 5.7: Images for the treated kidney in patient 1, (a) B-mode taken by the JC-200 B-mode probe during the ablation treatment, (b) CT scan slice rotated to follow the orientation shown in the B-mode image. (c) CT scan slice orientation used in simulation 1

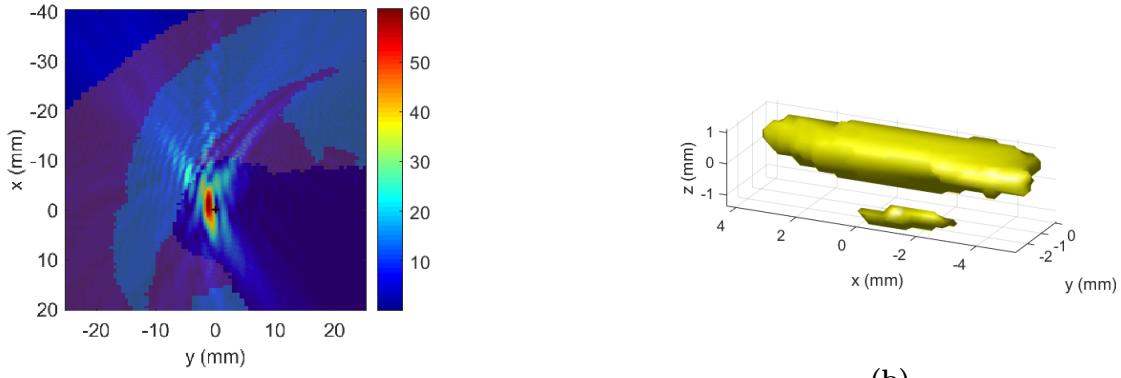

(a) (b)

Figure 5.8: Results for simulation $1^{\dagger}$, (a) axial focal plane with the pressure gain overlaid on the patient structure, the colours correspond to dark red for kidney, orange for fat, green for muscle and dark blue for water. (b) The iso-surface of the -6dB volume.

5.2 Thermal Simulations

Thermal simulations were conducted in order to investigate whether it would be possible to predict which patients would do best in the ablation treatment by comparing the size of the lesions created with a fixed source pressure. As well as to ascertain the source pressure required for lesion formation for each patient.

The thermal properties used in the thermal simulations are listed in Table 5.3. The thermal conductivity values used for tissue were obtained from measurements by Bowman [130]. A value of specific heat for the ribs was not found therefore a value for cranial bone was used instead [15]. It was assumed that the bone

composition for rib and bone would be similar since both are classified as "flat bone". Specific heat capacity values for muscle, fat and lung as well as perfusion values for bone and fat were obtained from Kok and Crezee [131] who reference the task group report from the European Society of Hyperthermic Oncology [132]. The perfusion value for kidney was obtained from Damianou and Hynynen [45]. The value for muscle was obtained from Cheng and Plewes [133] who referenced Feldman et al [134]. The perfusion value for the lung was calculated using the blood flow value of 400 mL/kg/min given by Williams and Leggett [135]. To calculate the perfusion rate in kg/m^3/s the blood flow rate was multiplied by the density of blood (1060 kg/m^3 [115]) and density of the partially deflated lung (700 kg/m^3 [127]), $\approx$ 5 kg/m^3/s. The conversion relationship was obtained from the National Council on Thermal Protection and Measurements, report number 113 [136].

Tissue types	Thermal conductivity (W/m/K)	Specific Heat (J/kg/K)	Perfusion (kg/m^3/s)
Bone	0.436	1590	0.12
Blood	-	3840	-
Fat	0.22	2387	1.1
Kidney	0.547	3890	70
Lung	0.478	3886	5
Muscle	0.508	3639	1.67

Table 5.3: The properties used in the thermal simulations.

The volume over which the thermal simulations were conducted were 34 mm x 26 mm x 20 mm around the focal point for simulations 1, 2 and 4, and 95.2 mm x 126.5 mm x 106.6 mm and 70 mm x 111.5 mm x 106.6 mm for simulations 3 and 5 respectively. The acoustic simulation's grid step of 246.7 μm was also used for the thermal simulations with a time step of 200 ms. The initial temperature was set as 37°C.

5.2.1 Thermal Simulation Results

A source pressure of 62 kPa was fixed for the first thermal simulations in order to compare the size of the lesion occurring across the different patient models.

A single sonication was simulated with a duration of 3 seconds, which was the duration used for the HIFU ablation treatment [75].

Table 5.4 details the maximum temperature and lesion size achieved for the five patient simulations. The highest temperature and biggest lesion occurred in simulation 1. Its size is almost double the size of the lesion created in simulation 4 and triple the lesion size in simulation 2. For simulations 3, 3* and 5 the maximum temperature in the kidney of 39.4°C, 39°C and 46.3°C respectively was not sufficient to cause a lesion. A higher source pressure is required for these three simulations. Simulation $1^{\dagger}$ which is a rotated version of simulation 1 resulted in a lesion less than half the size of the lesion generated in simulation 1 with a maximum temperature that is 25°C lower.

Simulation ID	Maximum Temperature (°C)	Lesion volume (mm^3)		
		Kidney	Muscle	Fat
1	99.1	20.1	0	0
$1^{\dagger}$	73.9	8.4	0	0
2	74.5	6.8	0	0
3	40.8 (in bone)	0	0	0
3*	40.9 (in bone)	0	0	0
4	80.3	11	0	0
5	46.3	0	0	0

Table 5.4: The maximum temperature achieved for the thermal simulations using a fixed source pressure of 62 kPa. The resulting volume for the thermal lesion created in the kidney, fat and muscle are also shown

For simulations $1^{\dagger}$, 2, 3, 4 and 5 the source pressure was increased until a lesion of approximately 27 mm^3 was achieved or a peak temperature of $\approx$ 100°C was reached. The source pressure at which this lesion was obtained is listed in table 5.5. For simulations 1, 2 and 4 in which tight focal regions were achieved, recall figure 5.4 and table 5.2, the maximum temperature was near or at 100°C at a smaller lesion size than for the other simulations. This is expected since the energy is deposited at a smaller volume and the source pressure required to form a lesion is lower. Figure 5.9 shows the position and shape of the resulting lesions. For simulations 3 and 5 significantly higher source pressures were required due to the fragmentation of the focal volume and the reflection of the acoustic energy at the rib interface.

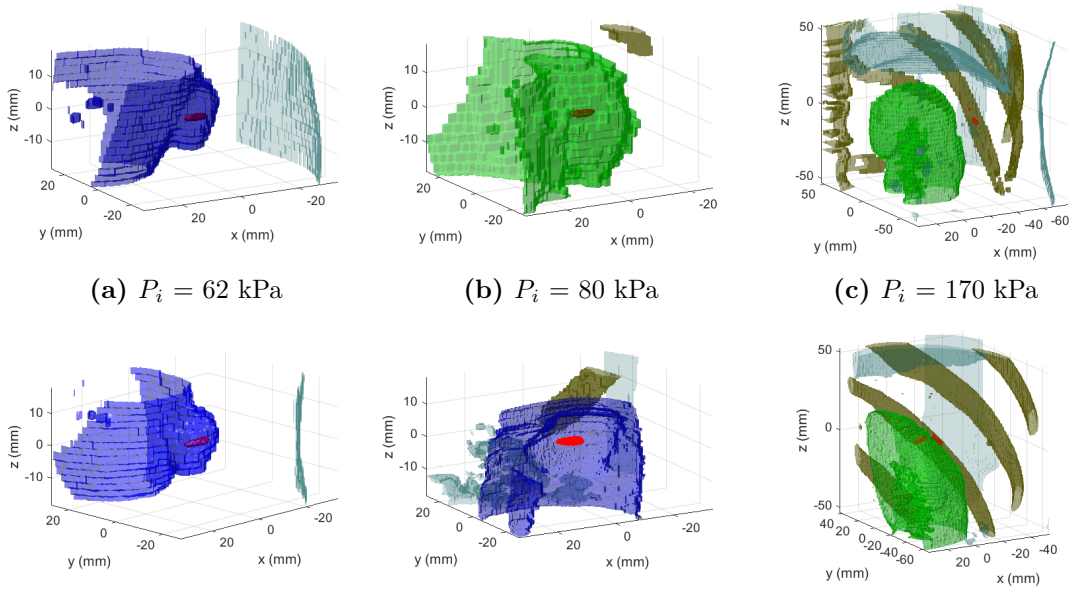

(a) $P_i = 62$ kPa **(b)** $P_i = 80$ kPa **(c)** $P_i = 170$ kPa

(d) $P_i = 80$ kPa **(e)** $P_i = 74$ kPa **(f)** $P_i = 130$ kPa

Figure 5.9: 3D plots of the resulting lesions with the patient geometry. The lesion is shown in red with right and left kidney geometry shown in blue and green respectively. The source pressure used for each simulation is defined. (a) Simulation 1, (b) simulation 2, (c) simulation 3, (d) simulation 1†, (e) simulation 4 and (f) simulation 5

Lesions were created in kidney for all simulations except for simulation 3 and 3*. Figure 5.9(c) shows that there was extensive heating in the rib bone. This was also the case for simulation 5. The maximum temperatures resulting in bone for simulations 3 and 5 were 65.5°C and 77.5°C respectively. When using properties for deflated lung in simulation 3* the maximum temperature at bone increased to 66.3°C. Table 5.5 shows that there was no lesion created for simulations 3 and 3* within kidney or the pre-focal tissue. Simulation 5 is the only simulation where a lesion was created in the pre-focal muscle layer.

5.3 Discussion

The results of the acoustic and thermal simulations can be compared with the outcome from the clinical trial. As part of the trial the kidney tumours were resected post HIFU treatment and tissue histology was used to determine the extent of the HIFU ablation achieved. These histology results provide a gold standard against which to compare the simulation results. The histology results

Simulation ID	Input Pressure (kPa)	Maximum Temperature (°C)	Lesion volume (mm^3)		
			Kidney	Muscle	Fat
1	62	99.1	20.0	0	0
1†	80	98.5	27.0	0	0
2	80	99.5	19.5	0	0
3	170	65.5 (in bone)	0	0	0
3*	170	66.3 (in bone)	0	0	0
4	74	98.7	21.9	0	0
5	130	77.8	29.2	1.2	0

Table 5.5: The source pressure at which a maximum temperature of $\approx$ 100°C was achieved or at which a kidney lesion of $>$ 27 mm^3 was achieved. Also listed are the resulting volumes for the thermal lesions created in fat and muscle.

showed that for patient 1 an ablation percentage of 70% was achieved. Whereas for patients 2 and 4 it was <5%, with the bulk of the tumour still viable [75]. These large differences between patient 1 on one hand and patient 2 and 4 were not captured in the simulations. There was a comparatively moderate reduction of peak pressure gain for simulations 2 and 4 from simulation 1 by 26% and 19% respectively. The three simulations showed no evidence of fragmentation with a well defined focal volume. The difference in peak pressure gain could be down solely to the increased acoustic path in attenuating tissue. The thermal simulations that used a fixed source pressure resulted in a lesion size in simulation 1 that was triple and nearly double that for simulations 2 and 4 respectively. Higher source pressure values were required for simulations 2 and 4 to achieve peak temperature and volume sizes comparable to simulation 1.

The results for patients 3 and 5 show severe fragmentation in the -6 dB iso-surface volume due to the ribcage. This is a result of the reflections that occur at the soft tissue bone interface due to the large difference in impedance between them. For simulation 3* the added impact of the reflection at the lung interface further reduced the pressure compared to simulation 3 where water properties were used.

The peak pressure gain value for both simulations 3 and 3* was less than 20% of that for simulation 1. Using the same source pressure of 62 kPa no lesion was created within simulation 3 and the maximum temperature rise within the kidney was only 1.4°C. In simulation 3 increasing the source pressure to 170 kPa did not

result in a lesion forming and the temperature recorded in bone for both simulations 3 and 3* was above 65°C which highlights the problem of delivering ultrasound through the rib cage. In contrast the clinical outcome for patient 3 was one of the best within the trial with 95% of the tumour volume successfully ablated - as found by histological results after tumour resection.

For simulation 5 the peak gain was nearly 34% that of simulation 1. Using the same source pressure of 62 kPa no lesion was created and the maximum temperature rise within the kidney was 9.3°C. A lesion of 29 mm^3 was created when the source pressure was increased to 130 kPa. But this came with a peak temperature of 77.5°C within the intervening rib. A small lesion of 1.2mm ^{3} was also created in the pre-focal muscle layer. The histology results for patient 5 are also not consistent with the simulation results and show no ablation within the kidney tumour and extensive ablation in the peri-nephric fat and normal renal parenchyma.

The MRI for patient 3 taken 12 days after the treatment did show evidence of extensive abdominal wall swelling [75]. This suggests that there was heating at the bone tissue interface. Within the simulation it is not possible to reflect the treatment procedure, since endotracheal intubation was used during the treatment to isolate the lung at the side of the kidney being ablated. The lung was also deflated or inflated to allow for better access for B-mode imaging [75]. Endotracheal intubation was mentioned as a means to inflate the lung in order to provide access to tumours behind ribs in another trial conducted by Wu et al [80]. However, they also used rib removal to provide an acoustic window for large tumour ablation.

The position of the transducer for all simulations was based on a manual selection of an appropriate acoustic window and did not follow the position of the patient during the treatment. A second simulation was undertaken for patient 1 with the transducer placed at a position that was determined from a B-mode image taken during the ablation treatment. For this simulation, $1^{\dagger}$, there was a 24% drop in pressure from the first simulation and the -6 dB iso-surface showed fragmentation. The subsequent thermal simulation showed a reduction in the lesion size by more than half. This result indicates that there could be a significant change in delivered

treatment due to the choice of the orientation of the transducer relative to the tissue layers. For the other 4 simulations it was not possible to find good quality B-mode images that showed the actual position for the transducer relative to the patient.

The significant effect that the transducer location had on the peak pressure gain and lesion formation motivated the investigation undertaken in Chapter 6. Simulations for three patient models were used to find the optimal position of the transducer for each.

The change in transducer position in simulation $1^{\dagger}$ resulted in a lesion size of 27 mm^3 before the temperature reached $\approx 100°C$. This is in contrast with a maximum lesion size of around 20 mm^3 that was achieved in simulation 1, 2, and 4 at a similar temperature. The lesion size in simulation 5 was 29 mm^3 when a source pressure of 130 kPa was used. Both simulations had fragmentation in the -6 dB focal volume. Defocussing can be advantageous in spreading the ultrasound energy to achieve a bigger ablation volume. However, this requires much higher source pressures and comes with a risk of an increase in pre-focal heating. For simulation 5 there was a significant increase in temperature in the rib bone.

The highly focussed fields in simulations 1, 2 and 4 can result in boiling, temperatures of 100°C or more, at lower source pressures compared to patients 3 and 5. The creation of bubbles in the ultrasound field would shield the targeted tumour and result in pre-focal heating. Also cavitation could occur at the pressures used in the thermal simulations. The pressure amplitude values obtained at the focus for simulations 1, $1^{\dagger}$, 2 and 4 are 5.3 MPa, 5.3 MPa, 5.4 MPa and 5.4 MPa respectively. These values are close to the 5.9 MPa which was found to be the cavitation threshold for dog's thigh tissue by in-vivo measurements for a 1 MHz source frequency [48]. Hynynen, therefore, suggested that in order to avoid cavitation the focal pressure value should not exceed 5 MPa [48].

The source pressures required to achieve lesions and temperatures up to 100°C that were obtained from the thermal simulation could be a guidance for identifying the transducer driving power required for the treatment. The transducers used here are different since the one simulated with the patient models had a 145 mm

radius of curvature and the one characterised in chapter 4 was a 164 mm transducer. However, an assumption could be made for the present that in the instance where the same transducer was used the focal pressure in water should be the same for both simulation and measurement. Using the focal gain from the simulation the source pressure from the thermal simulations could be translated into a required power level. The proportionality relationship of power to pressure squared can be written for the focal pressures in water from the simulation and calibration as follows:

$$\frac{P_{req}}{P_{cal}} = \left(\frac{p_{f,sim}}{p_{f,cal}}\right)^2 \tag{5.1}$$

where P_{req} is the required power, P_{cal} is the calibrated power, $p_{f,sim}$ is the required focal pressure from simulations in water and $p_{f,cal}$ the JC-200 calibrated focal pressure in water.

From chapter 4 the focal pressure obtained from radial scan 1 was 13.5 MPa at a power input of 150 W. Using the focal gain of 123 obtained from the simulation for the transducer in water will give a relationship of required power to source pressure $p_{src,sim}$

$$P_{req} = 150\text{W} \times \left(\frac{123 \times p_{src,sim}}{13.5\text{MPa}}\right)^2 \tag{5.2}$$

Substituting the source pressure values in equation 5.2 the patient models simulated here would give required powers of 48 W, 68 W, 80 W and 210 W corresponding to source pressures of 62 kPa, 74 kPa, 80 kPa and 130 kPa. The previous rough calculation indicates that powers of 275 W, which were used in the treatment [75], were much higher than required to generate focal lesions in patients 1, 2 and 4 and boiling would have likely occurred in the treatments. The method used to monitor the USgHIFU treatment in the clinical trial was B-mode hyperecho which is not efficient at detecting ablation [75]. Hyperecho could have been an indication of boiling or cavitation and may have failed to detect lesion formation when it occurred. Indeed evidence for boiling was seen in the resected specimens by Ritchie [75]. Figure 5.10 was copied from Ritchie's thesis and contains a histology result for an ablated tumour resected from a patient in the trial. It shows the presence of

cavities that result due to the formation of boiling bubbles [75]. The presence of boiling bubbles during the treatment would result in shielding of the acoustic energy from the focal point and reflection, which would cause increased pre-focal heating.

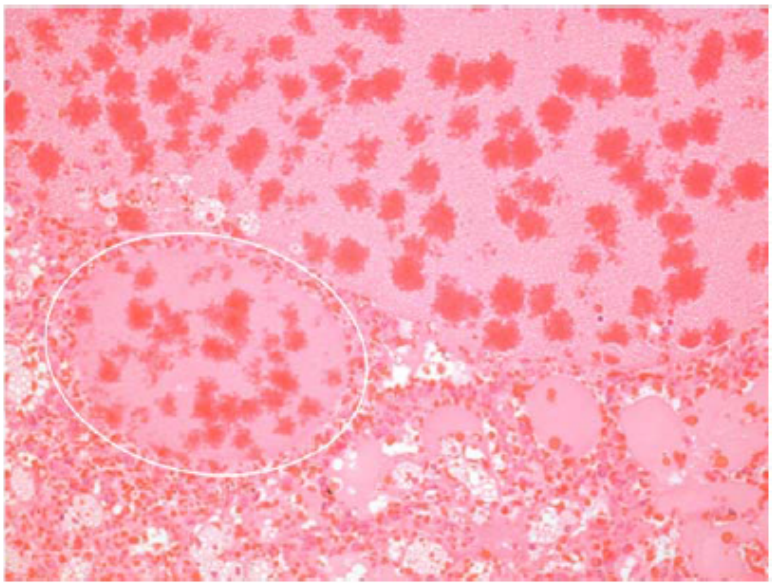

Figure 5.10: Histology result for one patient in the clinical trial. The circled area shows the formation of cavities that resulted from boiling, copied from [75]

Whereas the simulations described here did not result in pre-focal lesions in either simulations 1, 2, or 4, the presence of pre-focal heating was evident through contrast enhanced MRI in the clinical trial follow up. It showed pre-focal tissue swelling and peri-nephric fat ablation. Samples of peri-nephric fat were resected from all patients and all showed signs of ablation. The sample of peri-nephric fat from patient 4 had significant ablation.

In contrast to the simulations where the focus was not scanned the clinical trial used multiple sonications to form adjacent overlapping lesions [75]. The repetition of sonications passing through the pre-focal layers results in the accumulation of heating within them, which can lead to pre-focal tissue damage. This mechanism for pre-focal heating was not captured by the simulations.

Another limitation in the current model is that it is a linear model unable to describe the effects of the harmonics that are generated as the high pressure wave propagates through tissue nor the generation of cavitation activity as the

rarefaction pressures increase. The presence of nonlinear harmonics results in increased attenuation and thus heating present in pre-focal tissue, especially in fat which has a relatively high coefficient of nonlinearity. Cavitation also acts to enhance heating through broadband emissions that are readily absorbed by the surrounding tissue and through viscous damping due to the bubble oscillation within the ultrasound field.

From the previous discussion improvements to the prediction of HIFU treatment outcomes would be obtained by incorporating cavitation and boiling into the acoustic model. Also simulating multiple sonications would give a better understanding of the effect that the heating is having on the pre-focal tissue and the lesion boundary.

The simulation of the use of multiple sonications for lesion formation was studied by Fan et al [94]. The study highlighted the importance of allowing sufficient time between sonications to avoid damaging normal tissue. It also looked at the improvement in treatment time when a bigger lesion is formed and contrasted this with the use of a highly focussed spherical transducer in which energy is wasted delivering an excessive amount of thermal dose to the centre of the focus.

Other studies have incorporated cavitation in the acoustic or thermal models. Grisey et al incorporated cavitation as a local change in attenuation [137] based on a method by Chavrier et al. [138]. In their thermal model boiling and protein denaturation were incorporated as additional temperature dependent specific heat terms.

5.4 Conclusion

Acoustic and thermal 3D simulations were undertaken in patient derived models. The results for two patients showed the impact of the ribcage in reflection and attenuation of the acoustic energy resulting in fragmentation of the acoustic field. No fragmentation was observed in the focal point for the other three patient models indicating a sensitivity in results to transducer position. Indeed when a second simulation was undertaken for one of the patients at a changed transducer position fragmentation was seen in the -6 dB iso-surface volume.

The thermal simulations showed that when fixing the source pressure at a value that created thermal lesions in 3 patient models there was negligible temperature rise at the focus for the two patients in which there were severely fragmented focal volumes. The pressures had to be increased significantly to create thermal lesions within one of these patients. For the other patient an increase in pressure of nearly 3 times did not create a lesion within the kidney. The kidney lesions created in two simulations that had fragmentation in the half pressure volume resulted in a bigger lesion size compared to the 3 simulations with no fragmentation. Defocussing can provide bigger lesion sizes, but with an increased risk of pre-focal heating.

The thermal simulation results show that the pressures used could have resulted in boiling in the tissue during the treatment. Since boiling was not modelled this shows the difficulty in obtaining a correspondence with the experimental results using the current simulation model.

The results demonstrate patient to patient variability in the delivery of HIFU ablation treatments. The use of patient-specific computer models may be able to determine whether a patient is a good candidate for HIFU treatment. Knowing the possible placement of the transducer and its pressure field would aid the clinician in taking an informed decision about the power required to drive the transducer for a successful treatment. However, for the simulations here k-Wave took about 53 hours to run on 144 processors (the thermal simulations took about 10 minutes on a PC with 16 processor cores). Therefore even though k-Wave has been highly-optimised the simulation time means that treatment planning is only possible if imaging data is available a number of days in advance of treatment.

6

Transducer Position Optimisation

Specifying the position of the transducer with respect to the patient is an essential part of HIFU treatment. The tissue layers through which ultrasound energy is delivered can have a significant impact on the resulting pressure and fragmentation of the focal volume. Finding a position that results in the highest focal pressure and least fragmentation would be beneficial in improving treatment delivery. This chapter investigates, by the use of the computer model described earlier, how positioning the transducer at different locations surrounding the patient would have an impact on the resulting pressure and shape of the focal region. Back propagation from the target point to the transducer surface is used as a means to determine the best position to place the transducer for treatment delivery. The use of back propagation has been considered by Blackmore [139] who used the received phase and amplitude to guide the positioning of the focussed ultrasound transducer for use in brain stimulation. Gélat et al [140] used the inverse problem to deliver ultrasound through the ribs. The complex velocity for elements of a phased array were determined by setting the conditions that the pressure magnitude at the scatterer surface, ribs, should not exceed a maximum value and that the velocity amplitude at each array element should also be below a maximum value. The method used here is much simpler and is formulated for a single element transducer. It is based on the fact that the transducer can only be moved in the horizontal

plane of the patient around the abdomen after the target horizontal slice is selected. This creates a 1D problem based on the rotation angle for the transducer when the focal point is fixed within the tumour. The aim was to find the transducer location that would maximise the focal pressure delivered to the targeted tumour.

Computer models were generated using three patient CT scans from the kidney ablation clinical trial mentioned previously. The patient CT scans were chosen based on the location of the targeted kidney tumour. Figure 6.1 shows that in patient 1 the tumour was in the lower lobe with the ultrasound path clear from interference of ribs. For patient 2 a small section of the ribs was present between the transducer and the tumour, because the tumour was in an interpolar location. Whereas for patient 3 the rib cage was surrounding the tumour as it was located in the upper lobe of the left kidney.

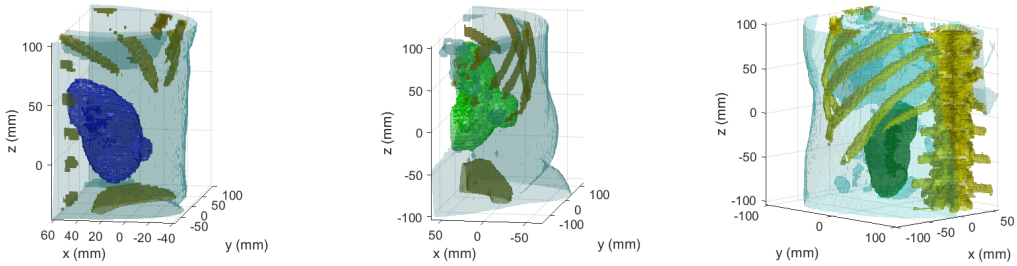

Figure 6.1: Three patient CT scans selected based on tumour location to test the ability of finding an optimal transducer position for HIFU ablation as a treatment planning step, (a) patient 1: the tumour is in the lower lobe of the right kidney, (b) patient 2: the tumour is in an interpolar location in the left kidney, (c) patient 3: the tumour is the upper lobe of the left kidney.

In order to define the best position for the transducer ultrasound wave back propagation is utilised. A point source was placed in the target tumour volume and the acoustic field was propagated onto a spherical surface with a radius of 145 mm, which corresponds to the radius of curvature of the JC-200 transducer. The sensor points at which to receive the propagated wave were specified over this surface which represents the possible placements for the transducer surrounding the abdomen for each patient. For patient 1 and patient 2 the sensors were defined as the points covering the transducer surface if it were placed over a 90° arc surrounding the

abdomen from -45° to +45° with a step size of 5 ° as shown in figure 6.2(a) and 6.2(b). For patient 3 the possible positions were restricted due to the transducer at the edge of the arc abutting on to the patient's body, as show in figure 6.2(c) the range was selected to be from -42.5° to 17.5° with a step size of 2.5°. These simulations will be referred to as back propagation simulations since the wave is travelling in the other direction from the target towards the transducer, unlike a forward simulation, which has the transducer as the source propagating into the medium and converging on the tumour target.

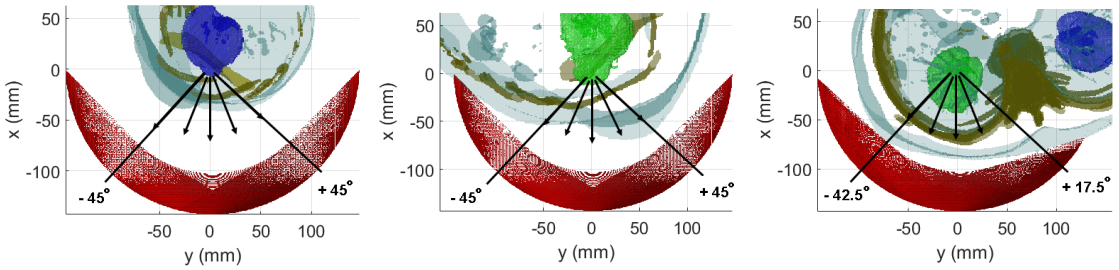

Figure 6.2: The configuration for the simulation showing the possible transducer positions as receiver points in red, (a) patient 1: the transducer surface is covering a 90° angle around the abdomen, (b) patient 2: same as in patient 1 the transducer placement is covering a 90°, (c) patient 3: a restricted placement limits the transducer to 60° surrounding the abdomen.

The back propagation simulations were undertaken using a k-Wave linear simulation with a resolution of 246.7 μm resulting in a grid size of 864 x 1296 x 864. The acoustic properties of the medium were defined as described in table 3.1. It took 63 hours to run one simulation on 144 processors on the University of Oxford's ARC computer cluster.

In order to have a comparison for the back propagation simulations for the optimal position of the transducer, forward linear simulations were undertaken at a lower resolution of 370 μm (4.2 PPW) at 9 different rotation angles between patient and transducer from -40° to 40° with a 10° step size. The lower resolution was used to reduce the simulation time. The position of the transducer was fixed within the k-Wave grid with the patient structure rotated as required. These forward simulations were run for patients 1 and 2. The 3D plots for the forward

simulations for patient 1 at -40°, 0° and 40° rotation angles are shown in figure 6.3. For all forward simulations two focal gains were calculated; one is the pressure gain obtained at the maximum pressure point from the simulation, the other is the pressure gain at the target focal point of the transducer. These will be referred to as the maximum pressure gain and the target focal gain respectively.

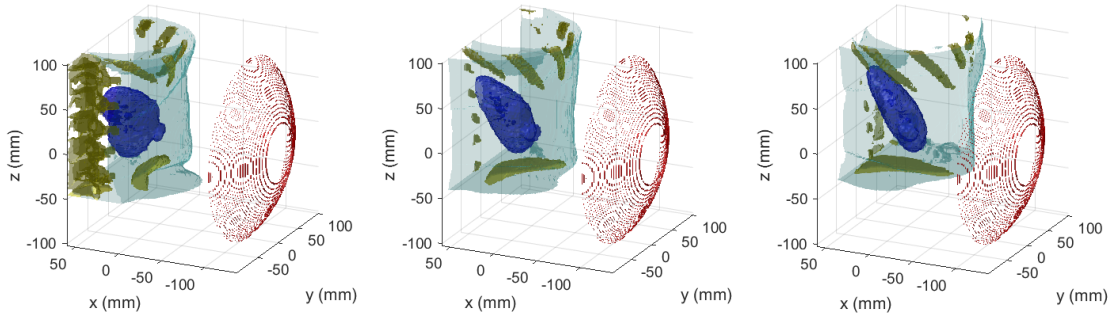

Figure 6.3: 3D plots from the forward simulations for patient 1 showing the patient CT rotated at different angles with respect to the transducer (a) at -40°, (b) at 0° and (c) at 40°

For back propagation simulations the time waveform of the pressure signal was recorded at the sensor points defined at the surface of the full arc representing the potential transducer locations. The phase and amplitude were extracted from the resulting time signal by applying the fast Fourier transform (FFT) to each signal. The arc that was used to receive the pressure signal suffers from staircasing effects because of the use of a discrete grid. Therefore, a reference back propagation simulation was undertaken using a uniform medium with the sound speed properties of water at 1500 m/s and no attenuation. Figure 6.4 shows the received amplitude and phase over the sensor arc for the back propagation simulation in water.

To select the position of the transducer from the sensor arc defined in the simulation the indices corresponding to a specific transducer location were chosen from the complete arc defined in the simulation. Figure 6.5 shows the selection of the transducer at three positions at angles -45°, 0° and 45° from the simulation in water.

Three metrics were investigated as a means to find an optimal placement for the transducer along the receiver's arc; one relating to the pressure amplitude received

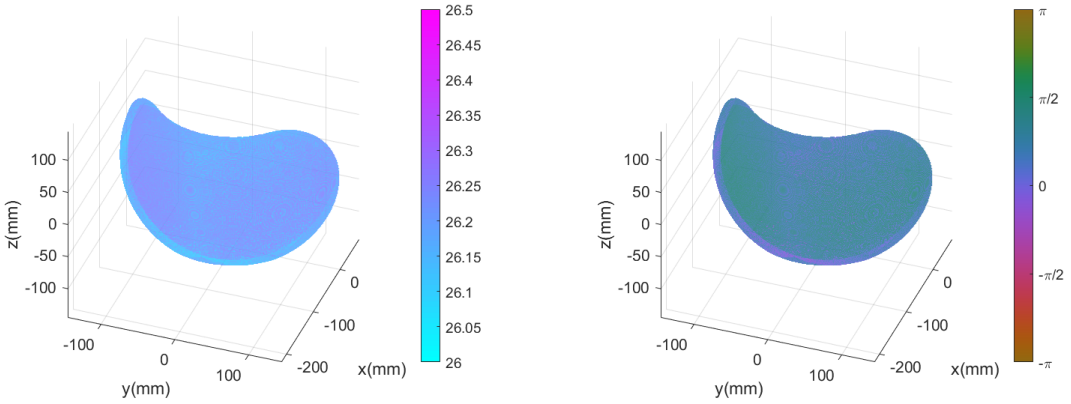

(a) **(b)**

Figure 6.4: The result of the back propagation simulation for water using a 100 kPa point source placed at the focal point of the transducer. (a) Received pressure amplitude and (b) Received phase.

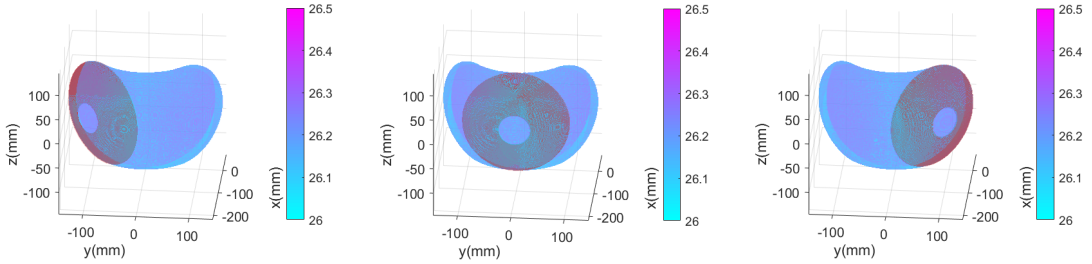

(a) **(b)** **(c)**

Figure 6.5: The selection for the transducer surface from the full receiver arc for the homogeneous medium back propagation simulation, showing the transducer highlighted on the received amplitude values at the rotation angles of (a) -45°, (b) 0° and (c) +45°

at the surface of the transducer and another relating to the phase of the pressure signal, with the third using the summation of the complex pressure amplitude on the transducer's surface. These were calculated over the face of the transducer position from the receiver's arc using a step size of 2.5°.

The back propagated average pressure (BPAP) is the average pressure of the signal received at the defined receiver points that represent the surface of the selected transducer.

$$BPAP = \frac{1}{N} \sum A_p \tag{6.1}$$

where A_p is the received pressure amplitude at the surface of the transducer, N

the number of points on the surface of the transducer.

The back propagated phase deviation ($BPPD$) is the root mean square deviation (RMSD) of the phase values of the received pressure signal.

$$BPPD = RMSD(\phi) = \sqrt{\frac{\sum (\phi - \bar{\phi})^2}{N}} \tag{6.2}$$

where ϕ is the phase value at the surface of the transducer, N the number of points representing the transducer, $\bar{\phi}$ is the mean phase value. The RMSD was chosen as the metric for the phase because a uniform phase is required over the face of the transducer for optimal focussing. A higher phase RMSD value would mean bigger phase deviation across the face of the transducer.

The summation of the complex pressure over the face of the transducer is calculated using the following equation and referred to as the back propagated complex pressure:

$$BPCP = \mid \sum A_p e^{j\phi} \mid \tag{6.3}$$

The calculated BPAP, BPPD and BPCP for the water simulation are shown in figure 6.6. They show an insignificant variation of 0.03% for the BPAP and variation over the range of 0.05 rad (2.9°) for the BPPD.

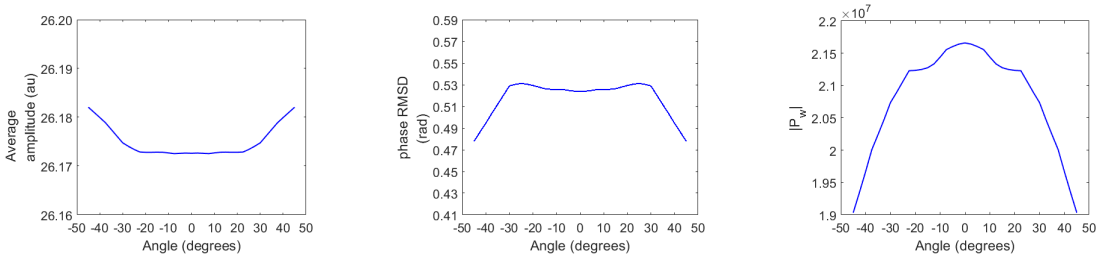

(a) **(b)** **(c)**

Figure 6.6: The results of the calculation for (a) BPAP, (b) BPPD and (c) BPCP over the face of the transducer for the water simulation
. The transducer is selected from the receiver surface at angles from -45° to 45° with a step size of 2.5°.

6.1 Patient 1 Results

The back propagation simulation for patient 1 resulted in the received signal amplitude and phase shown in figure 6.7. The amplitude plot shows that the values recorded at the surface of the transducer were in the range of 30 to 15 Pa. The phase plot shows a more uniform phase distribution to the left of the graph.

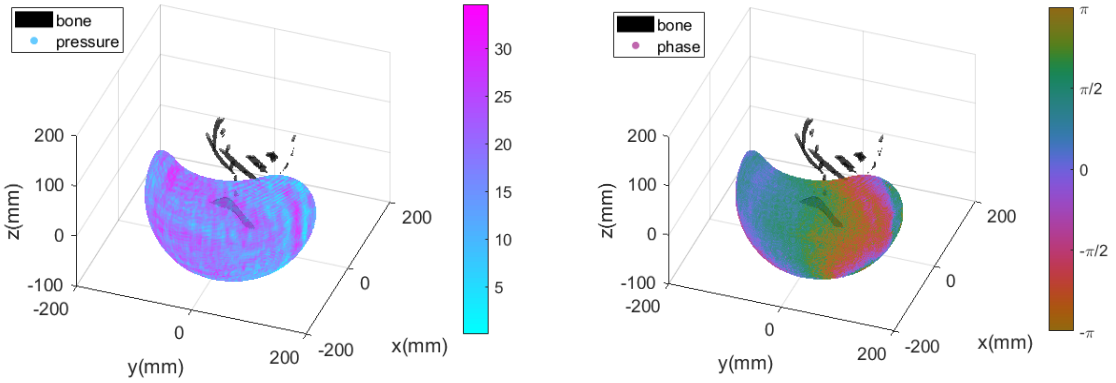

(a) (b)

Figure 6.7: The result of the back propagation simulation for patient 1 using a 100 kPa point source placed at the focal point of the transducer in the targeted tumour. (a) Received pressure amplitude and (b) Received phase.

To translate the previous graphs into numbers that can be used to select the best position, the BPAP and BPPD were calculated. Figure 6.8 shows the plots of the BPAP and BPPD plotted in relation to the transducer's angular position for patient 1. The values for BPAP and BPPD compensated for staircaising effects are overlaid with the non-compensated values.

Figure 6.9 compares the values for the maximum pressure from the forward simulations and BPAP from the back propagation simulation. The BPAP received at the transducer's surface is increasing towards the negative rotation angles, and has a maximum at -22.5°. When comparing the result of the back propagation simulation with the maximum pressure gain obtained from the forward simulations over the rotation angles specified, a similarity is seen with the BPAP graph.

Although not completely aligned the BPPD in figure 6.8 also shows the same trend as the BPAP. The lower values of BPPD are on the negative angle region of the graph coinciding with the higher BPAP values. This follows what would be

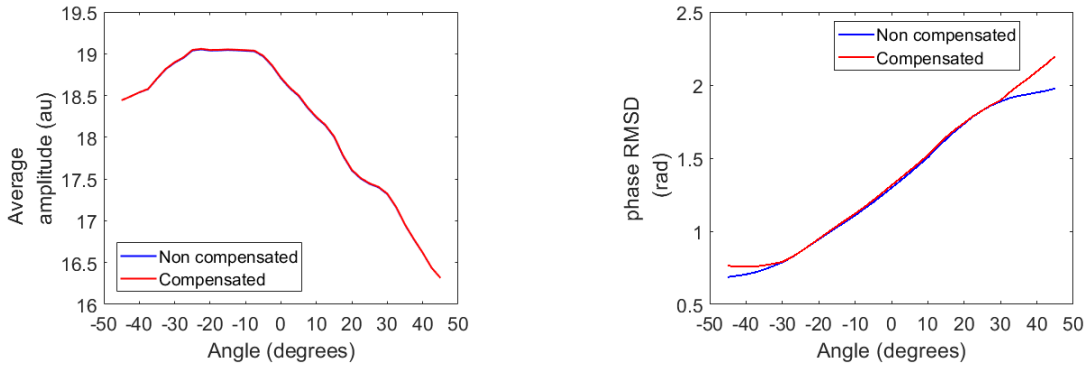

(a) (b)

Figure 6.8: The results of the calculation for received amplitude and phase over the face of the transducer for patient 1. The transducer is selected from the receiver surface at angles from -45° to 45° with a step size of 2.5°. (a) BPAP. (b) BPPD

expected from an optimal position which would have a more uniformly distributed phase over the surface of the transducer.

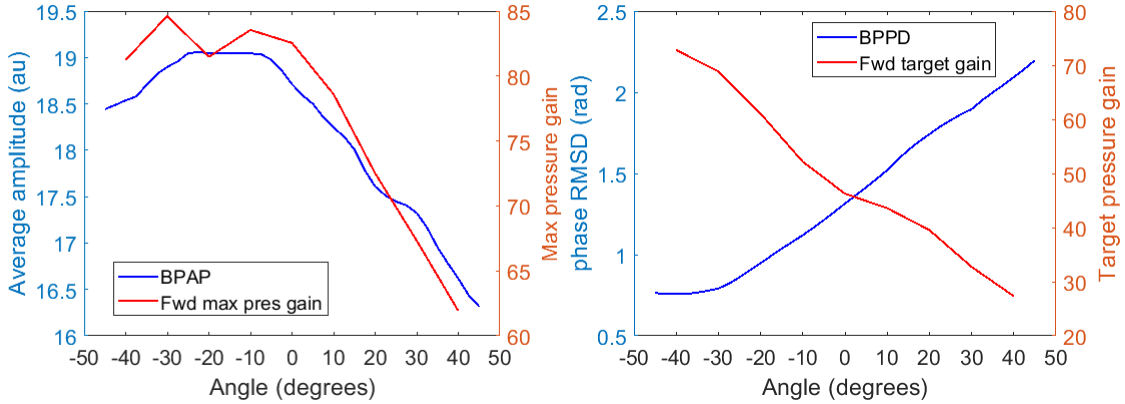

(a) (b)

Figure 6.9: Patient 1 results: (a) A graph showing the relationship of the forward simulations at 370 μm resolution and the BPAP relative to rotation angle. The graphs are overlaid to show the similarity of their maximum and minimum points.(b) The pressure gain at the target point for the forward simulations plotted with the BPPD.

The target focal gain calculated for the forward simulations for patient 1 is shown in figure 6.9(b). It is plotted with the BPPD graph and shows a similar trend for best location, since the maximum gain corresponds to the minimum BPPD value. The BPPD was used to indicate the positions at which the transducer would be more able to focus at the target, which indicates that it would agree with the graph representing the pressure at that target. The target gain graph shows that

the optimal location has shifted from that found for the maximum pressure gain in figure 6.9(a) and could be no longer within the range of angles simulated. The gain obtained at the target is lower than the maximum pressure gain, by up to 43% at an angle of 40°. The distance between the location of the maximum pressure gain and the target gain for all forward simulations of patient 1 is shown in table 6.1 and referred to as the focal point shift.

Rotation Angle	Focal point Shift (mm)			
	x	y	z	R
-40°	-0.74	-0.37	0.37	0.91
-30°	-0.74	-0.37	0.37	0.91
-20°	-0.74	-0.37	0.37	0.91
-10°	-0.37	-0.74	0	0.83
0°	0	-0.74	0	0.74
10°	0	-0.74	0	0.74
20°	-0.37	-0.74	0	0.83
30°	0	-0.74	0	0.74
40°	-0.74	-1.1	-0.37	1.38

Table 6.1: The shift in the focal point for the forward simulations for patient 1. x, y and z are the axial, lateral and elevational directions respectively, R the euclidean distance

The shift value for all rotation angles is less than 1 mm except at an angle of 40°. This distance is small considering the 10 mm treatment margin normally used. The maximum pressure gain would give a better indication of the optimal treatment location for the transducer, since it better reflects the potential efficacy of the treatment. It is nevertheless important that the position of the point of maximum focal pressure should be as close as possible to the target location. The observed discrepancy between the required target point and the point of maximum pressure highlights the importance of overlapping adjacent lesions.

In order to investigate whether the BPAP is a good metric for determining the optimal transducer position two simulations were undertaken for patient 1 using a resolution of 246.7 μm (6.3 PPW). One at the rotation angle of -22.5°, which corresponds to the maximum BPAP value and the other at an angle of 45°, which corresponds to the minimum BPAP. The results in table 6.2 show that the

maximum pressure gain was 28% lower for the simulation at the rotation angle that had the lowest value for the BPAP, 45°, in figure 6.8 than that which had the highest value, -22.5°. The pressure gain at the target point was 54% lower. The table also shows that the shift in the location of the maximum pressure is smaller for angle -22.5°, although only by 1 mm. Figure 6.10 also shows that the size of the focal region was less focussed for the simulation with the lower focal gain at 45°. The patient geometry shows that the structure of the tissue layers in figure 6.10(a), at -22.5°, was more aligned to the transducer, placed above, than the layers in figure 6.10(b), at an angle of 45°.

Rotation Angle	Maximum gain	Gain at target	Shift (mm)			
			x	y	z	R
-22.5°	90	66	-0.49	-0.49	0.25	0.74
45°	64	30	-1.5	-1	-0.25	1.82

Table 6.2: The results of the forward simulations for patient 1 at -22.5° and 45° showing the maximum pressure gain, the target focal gain, the difference in the location of the maximum pressure point from the target, where x,y and z are the axial, lateral and elevational dimensions respectively, R is the euclidean distance

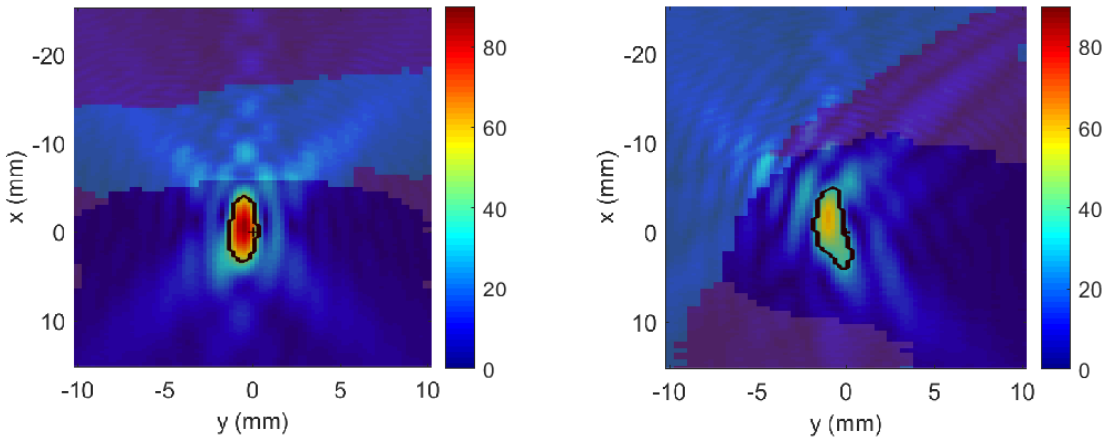

(a) -22.5° **(b)** 45°

Figure 6.10: The horizontal plane results for patient 1 for two simulations with the patient CT placed at different rotation angles relative to the transducer. (a) The simulation at -22.5° results in a higher gain than (b) the simulation at 45°. The tissue colours correspond to: dark red for kidney, red for fat, green for non-fatty tissue and dark blue for water. The colour bar shows the pressure gain and the HIFU focal point target location is marked with a black cross and the -6 dB contour is marked in black.

The values of the graph for forward target gain in figure 6.9(b) and its difference from the BPAP graph in figure 6.8(a), suggest a need to consider the complex

pressure received at the transducer's position in order to ascertain a location that would give a bigger target pressure than that obtained at the rotation angle of -22.5°. Figure 6.11 shows the BPCP normalised by the results in water. The maximum point for the BPCP graph is at an angle of -45° giving a different position for optimal transducer location.

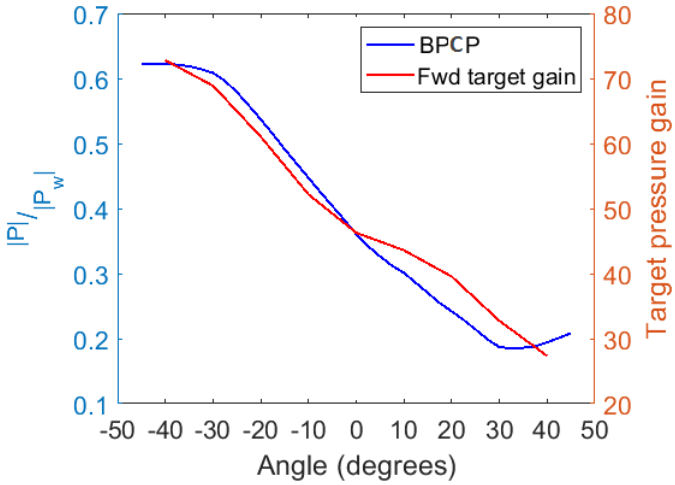

Figure 6.11: The BPCP for patient 1 normalised by the values from water compared to the pressure gain at the target point from the forward simulation, the graphs are overlaid to show their similarity.

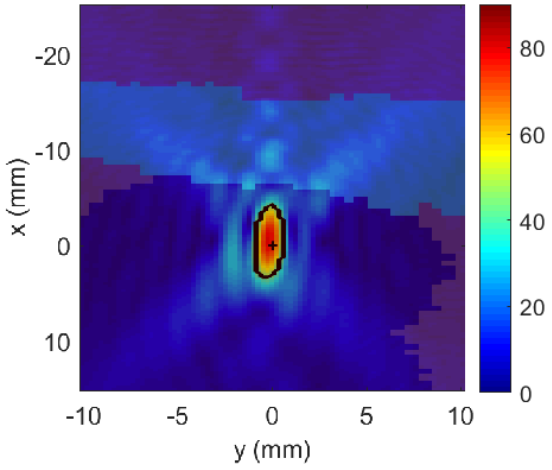

Figure 6.12: The horizontal plane result for patient 1 with the transducer placed at an angle of -45°. The tissue colours correspond to: dark red for kidney, red for fat, green for non-fatty tissue and dark blue for water. The colour bar shows the pressure gain and the HIFU focal point target location is marked with a black cross and the -6 dB contour is marked in black.

A forward simulation at a resolution of 246.7 μm was run at a rotation angle of -45°, at which the maximum BPCP graph was recorded. The maximum pressure gain achieved was 85 which is 5% lower than that obtained at -22.5°. However, the target gain was higher at a value of 76 which is 15% higher than for -22.5°. Figure 6.12 shows that the focal region is well formed with no apparent fragmentation. The tissue layers in this horizontal plane also appear to be aligned to the transducer, transmitting from above.

6.2 Patient 2 Results

The received amplitude and phase results for the back propagation simulation for patient 2 are shown in figure 6.13. The calculated values for BPAP and BPPD over the surface of the transducer from -45° to +45° give the graphs shown in figure 6.14. The graphs show the compensated values overlaid on the non-compensated values. The difference in the maximum and minimum BPPD values is 0.6 rad, therefore the BPPD graph shows a bigger sensitivity to compensation using water values to that seen from patient 1. The BPAP and BPPD graphs in figure 6.14 are comparable in their shape. With the higher BPPD values coinciding with the lower BPAP values. The BPPD graph has a minimum at an angle of 7.5° only 5° away from the maximum for the BPAP graph.

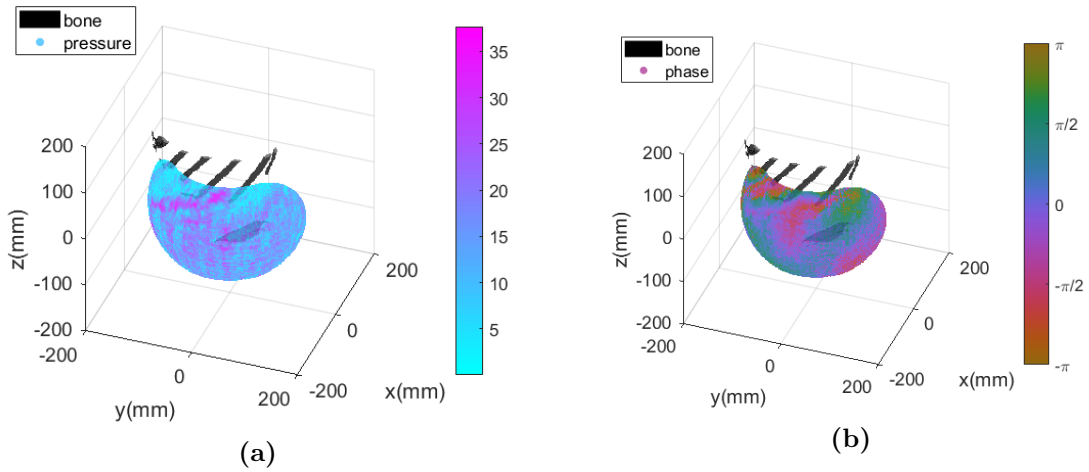

Figure 6.13: The result of the back propagation simulation for patient 2 using a 100 kPa point source placed at the focal point of the transducer in the target tumour. (a) Received pressure amplitude and (b) received phase.

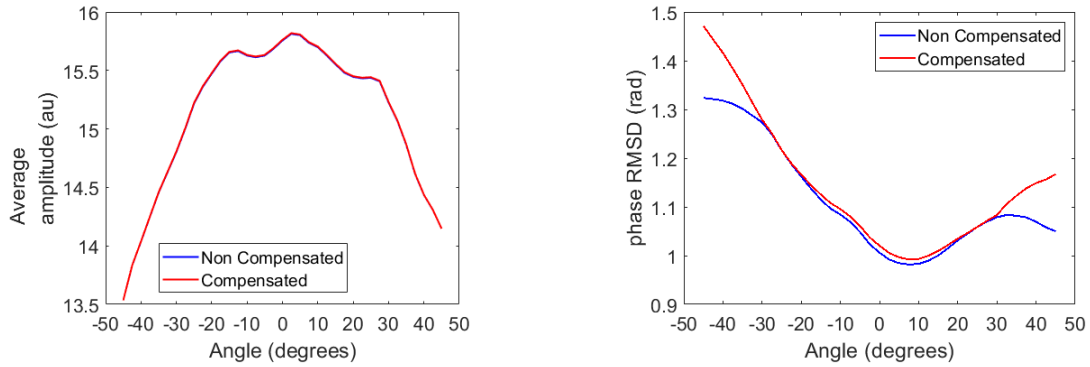

(a) (b)

Figure 6.14: The results of the calculation for received amplitude and phase over the face of the transducer for patient 2 after compensation with homogeneous medium values. The transducer is selected from the receiver surface at angles from -45° to 45° with a step size of 2.5°. (a) BPAP. (b) BPPD

Forward simulations were also undertaken for patient 2 with a resolution of 370 μm at rotation angles between patient and transducer of -40° to 40° with a 10° step size. The maximum pressure gain was plotted relative to the rotation angle. This maximum gain relationship had a similar trend to the BPAP value obtained from figure 6.14. The graphs are overlaid to show the similarity in the location of the maximum and minimum points, figure 6.15.

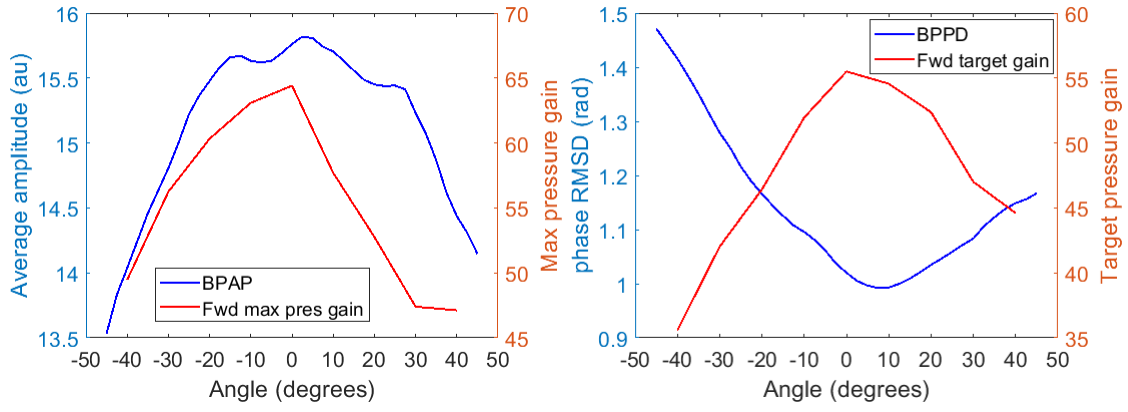

(a) (b)

Figure 6.15: A graph showing the relationship of the forward simulations and back propagation simulation relative to rotation angle, patient 2. The graphs are overlaid to show the similarity of their maximum and minimum points. (a) The maximum pressure gain for the forward simulations plotted with the BPAP graph. (b) The pressure gain at the target focal point for the forward simulations for patient 2 plotted with the BPPD graph.

The target focal gain was obtained for the forward simulations of patient 2 and is shown in figure 6.15(b) with the BPPD plot overlaid on it to show the similar trend in both. For patient 2 the target focal gain plot follows the same shape as the maximum pressure gain plot with the minimum value at the same rotation angle and a maximum value only 2.5° away.

The BPCP graph for patient 2 is shown in figure 6.16 and can be seen to follow the pressure gain at the target closely.

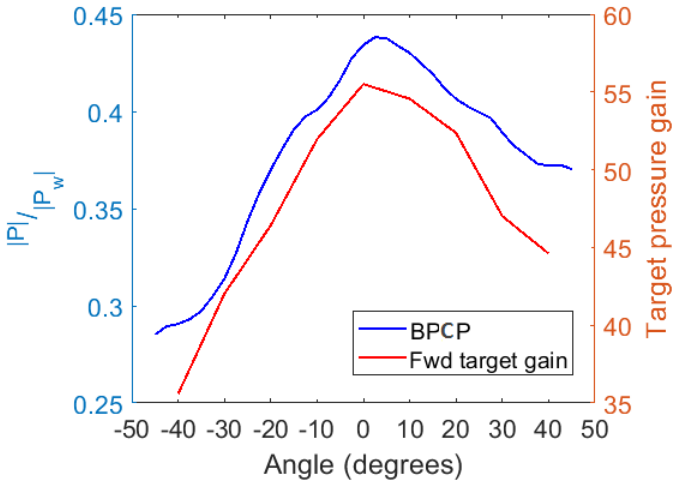

Figure 6.16: The BPCP for patient 2 normalised by the values from water compared to the pressure gain at the target point from the forward simulations, the graphs are overlaid to show their similarity.

The BPAP and BPCP for patient 2 agreed in the angle at which the minimum and maximum values were found and both showed similarity to the results from the forward simulations. Therefore, two simulations were undertaken at angles 2.5°, and -45°, where the maximum value and minimum value, respectively, of the BPAP and the BPCP were found. The results of pressure gain and focal shift are shown in table 6.3. The results show that at -45° the maximum gain is lower by 32% than at 2.5° and the pressure gain at the target drops by 37%. The shift in the maximum pressure point is higher at the 2.5° location, but it is 1.5 mm and predominantly in the axial direction, which is not significant for a focal volume with a -6 dB axial width of $\approx$ 6 mm. Figure 6.17 shows the horizontal plane for the simulation results with the pressure gain overlaid on the patient geometry. The

tissue layer structure in figure 6.17(a), at -2.5°, appears to be more aligned with the transducer, transmitting from above, than the structure in figure 6.17(b), at -45°.

Rotation Angle	Maximum gain	Gain at target	Shift (mm)			
			x	y	z	R
2.5°	69	59	-1.48	0	-0.25	1.5
-45°	47	37	-0.98	0.49	-0.25	1.12

Table 6.3: The results of the forward simulations for patient 2 at 2.5° and -45° showing the maximum pressure gain, the gain at the target point, the difference in the location of the maximum pressure point from the target, where x,y and z are the axial, lateral and elevational dimensions respectively, R is the euclidean distance

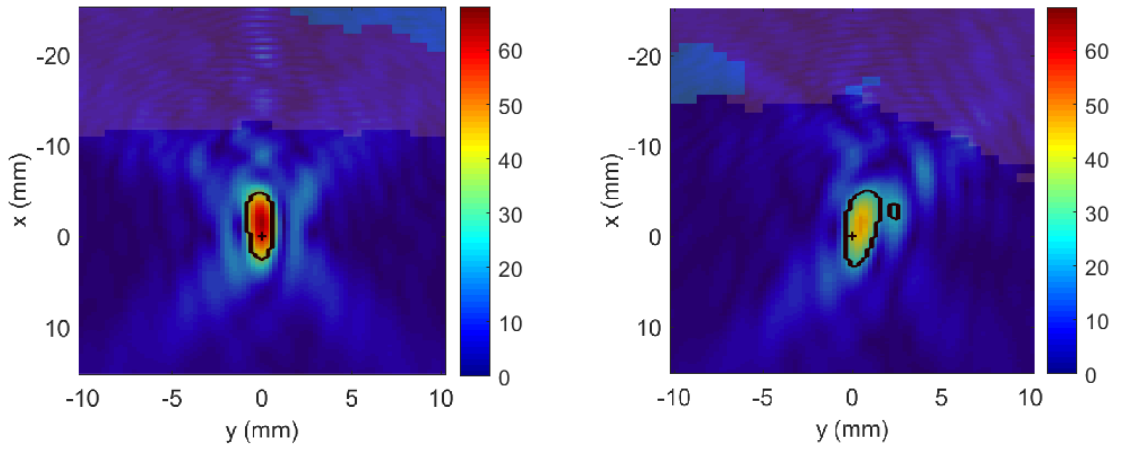

(a) 2.5° **(b)** -45°

Figure 6.17: The horizontal plane results for patient 2 for two simulations with the patient CT placed at different rotation angles relative to the transducer. (a) 2.5° results in a higher actual focal gain than (b) at -45°. The tissue colours correspond to: dark red for kidney, red for fat, green for non-fatty tissue and dark blue for water. The colour bar shows the focal gain and the HIFU focal point target location is marked with a black cross and the -6 dB contour is marked in black.

6.3 Patient 3 Results

The received amplitude and phase for patient 3 are shown in figure 6.18 on a surface representing the transducer in an arc from -42.5° to 17.5°. The pattern of the ribs is apparent on both plots.

The values for the BPAP and BPPD are shown as a function of possible angles for transducer placement in figure 6.19.

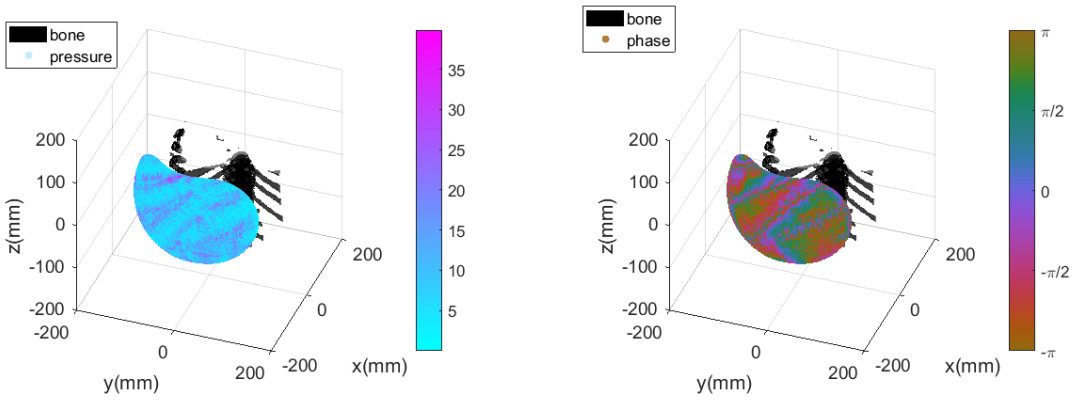

(a) (b)

Figure 6.18: The result of the back propagation simulation for patient 3 using a 100 kPa point source placed at the focal point of the transducer at the centre of the targeted tumour. (a) Received pressure amplitude and (b) received phase.

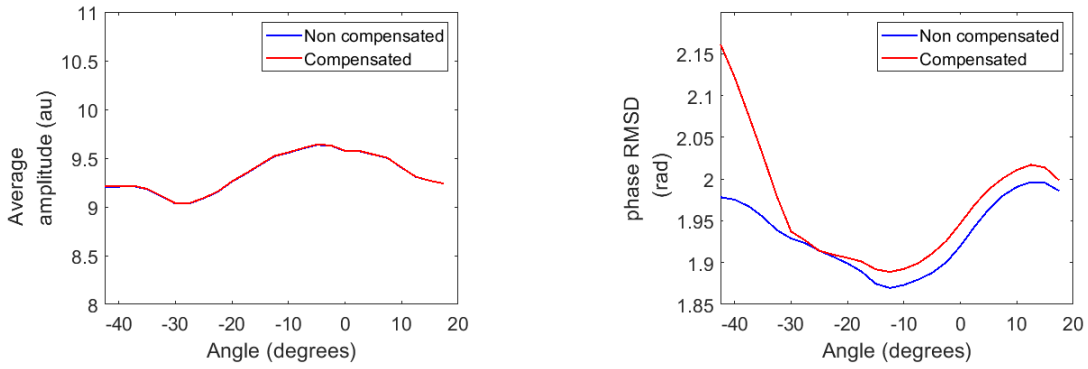

(a) (b)

Figure 6.19: The results of the calculation for received amplitude and phase over the face of the transducer for patient 3. The transducer is selected from the receiver surface at angles from -42.5° to 17.5° with a step size of 2.5°. (a) BPAP. (b) BPPD

The maximum value of 9.6 for the BPAP graph over the potential angle locations for patient 3 is nearly 50% lower than the maximum values obtained for patients 1 and 2. The reduction in received average pressure is due to the ribs blocking the signal propagation to the surface arc from the point source to the receiver surface.

The BPCP graph for patient 3 is shown in figure 6.20. It shows a maximum value at 12.5° and a minimum at -22.5° which are different to the maximum BPAP value recorded at an angle of -5° and the minimum at -30°. Forward linear simulations with 246.7 μm resolution were undertaken at 13°, -5° and -30° and a simulation at a resolution of 370 μm was conducted at angle -22.5°. This latter lower resolution

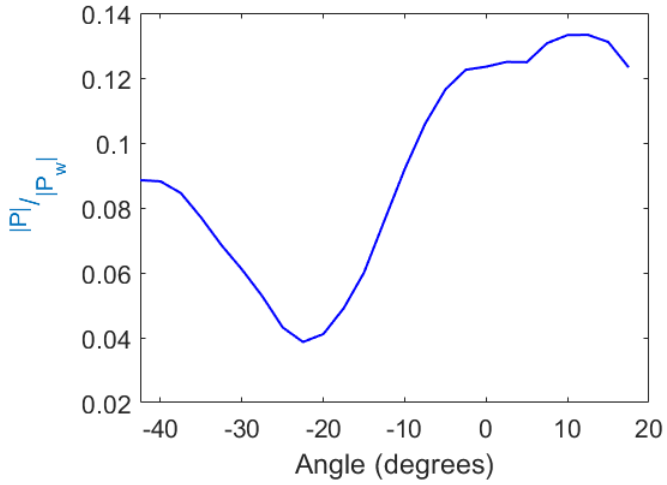

Figure 6.20: The BPCP for patient 3 normalised by the values from water.

was used for speed of execution due to time constraints.

Table 6.4 shows that the maximum focal gain of 16 resulting from the forward simulation at -30°, the angle with the smallest BPAP value, is 27% lower than the gain of 22 at -5°, the angle with the highest BPAP value. The target focal gain of 5, at -30° was also lower than at -5° where the value was 13. However, a maximum gain of 26, 15% higher than the gain at -5° was recorded at an angle of 13°, close to 12.5° where the peak BPCP value was obtained. The focal gain at the target point at both -5° and 13° was 13. The minimum BPCP value was at -22.5° at which the lowest maximum gain of 14 and lowest target gain of 3 was recorded. The low focal gain in all simulations and the shift of two millimetres in the lateral direction between the target focal point and the maximum pressure point shows that the presence of the ribs has had a significant impact on defocussing the ultrasound beam.

Rotation Angle	Maximum gain	Gain at target	Shift (mm)			
			x	y	z	R
-5°	22	13	-0.74	-1.73	-0.25	1.9
-30°	16	5	-0.49	-1.97	-0.49	2.1
13°	26	13	0.99	-1.73	-0.49	2.05
-22.5°	14	3	1.11	-2.22	-0.74	2.6

Table 6.4: The results of the forward simulations for patient 3 at -5°, -30°, 13° and -22.5° showing the maximum pressure gain, the gain at the target point, the difference in the location of the maximum pressure point from the target, where x,y and z are the axial, lateral and elevational dimensions respectively, R is the euclidean distance

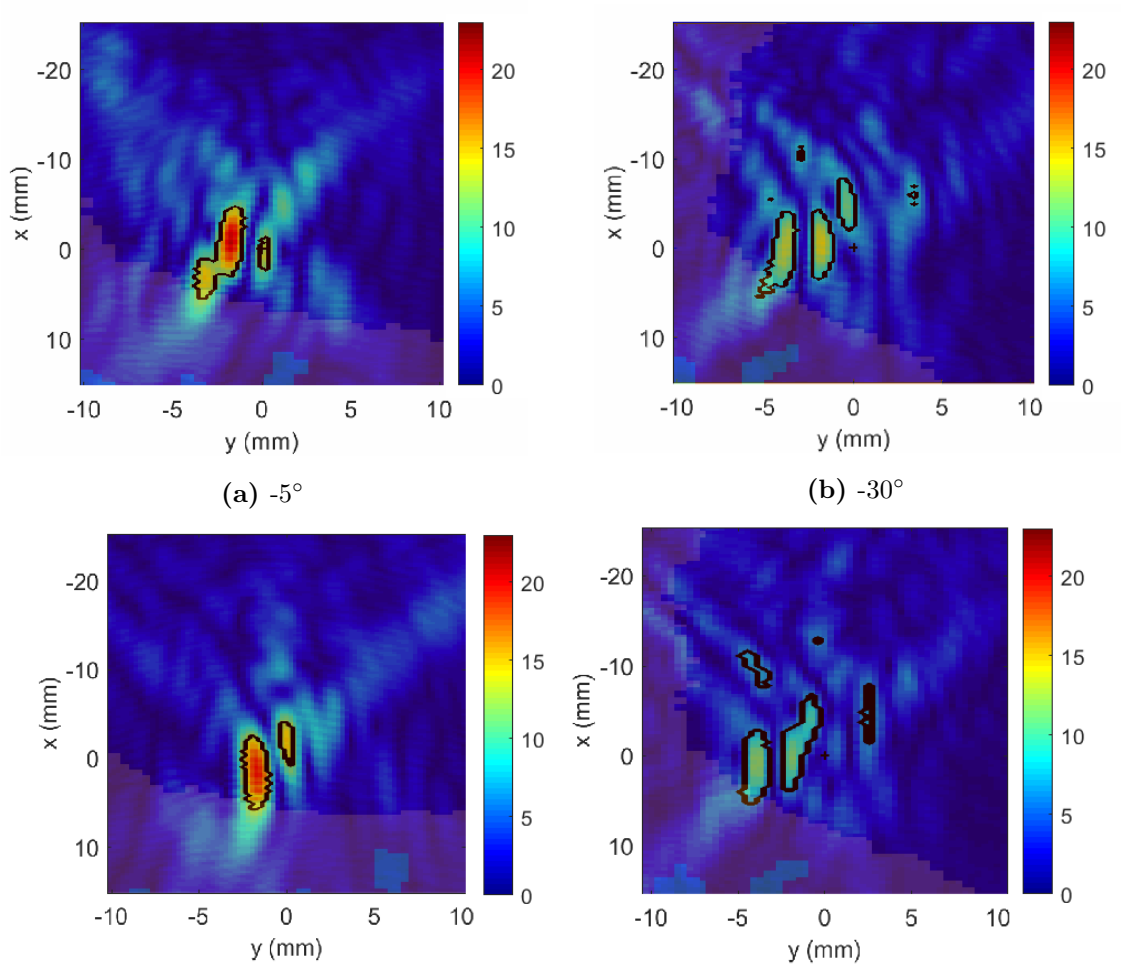

(a) -5° **(b)** -30°

(c) 13° **(d)** -22.5°

Figure 6.21: The horizontal plane results for patient 3 for two simulations with the patient CT placed at different rotation angles relative to the transducer. (a) -5°, maximum BPAP, (b) -30°, minimum BPAP, (c) 13°, maximum BPCP and (d) -22.5°, minimum BPCP. The tissue colours correspond to: dark red for kidney, red for fat, green for non-fatty tissue and dark blue for water. The colour bar shows the focal gain and the HIFU focal point target location is marked with a black cross and the -6 dB contour is marked in black.

A map of the focal pressure at the horizontal slice through the target focal point is shown in figures 6.21(a)-(d). The figures show significant fragmentation of the focus with the simulations at -30° and -22.5° evidently more affected. Figure 6.22(a) and (b) show the fragmentation on a 3D representation of the -6 dB iso-surface for the simulations at 13° and -5°. These figures display that the fragmentation is less at the former angle than at the latter. These results emphasise the importance of the position of the source in delivering the ultrasound energy to the target through

the intervening tissue layers, especially in the presence of intervening ribs.

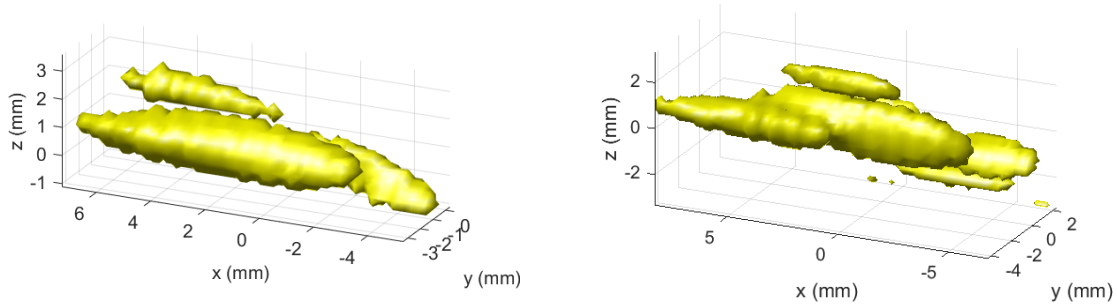

(a) 13° **(b)** -5°

Figure 6.22: The iso-surface of the -6 dB focal volume for the forward simulations of patient 3 at rotation angles of (a) 13°, (b) -5°

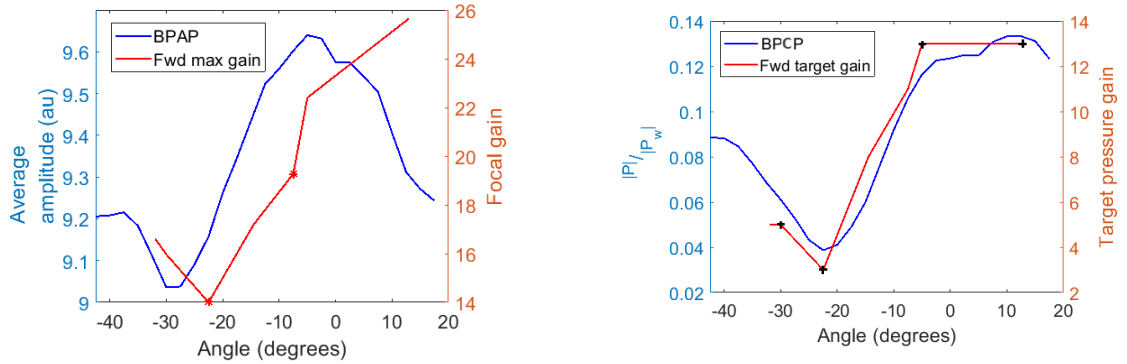

(a) **(b)**

Figure 6.23: (a) The BPAP graph for patient 3 is plotted with the maximum focal gain values obtained from forward simulations, the points with an asterisk were obtained from simulations with a spatial resolution of 370 μm. For all other simulations the resolution was 246.7 μm. (b) The BPCP for patient 3 normalised by water plotted with the pressure gain values at the target focal point from forward simulations, the black crosses mark the values of the BPAP at angles -30°, -22.5°, -5° and 13°.

Another two forward simulations for patient 3 were carried out at angles -12.5° and -7.5° in order to show the trend for maximum gain and focal target gain. The maximum pressure gain is plotted in figure 6.23(a) with the BPAP graph. The shape of the maximum pressure gain graph is different to that expected from the BPAP values with the maximum and minimum pressure gain points not at the angles chosen from the BPAP graph. The BPCP graph closely follows the target focal gain graph as shown in figures 6.23(b).

6.4 Discussion

The results that are obtained in this chapter show that the position of the transducer relative to the patient geometry can have a significant impact on the ability to focus ultrasound into the body and by extension the resulting HIFU treatment. The optimal position in both patients 1 and 2 was found to be when the transducer was placed in a plane that was parallel to the layered tissue geometry. The results are similar to findings by other groups who investigated the orientation of the transducer relative to the tissue geometry. Fan and Hynynen [71] studied the effect the beam entrance angle had on the resulting focus in heterogeneous layers using 2D simulations and experiments. They found that the focus can be shifted by several millimeters as the angle moves from the normal [71]. In a follow up [141] they modelled the effect of curved tissue by using a curved layer of polyethylene with either water alone or a combination of castor oil and water. They found a shift of a few millimeters in the position of the focus and a reduction in pressure when the position of the transducer was shifted laterally from the centre of the curved polyethylene layer [141]. Liu et al [72] also used 2D simulations based on patient MR data to test the effect the transducer phased array tilt would have on the resulting focus in uterine fibroids. Their results showed that phase correction on tilted angle sources resulted in a 16% increase of pressure compared to the non-corrected case [72].

These previous results make it relevant to determine a rotation angle for the transducer relative to the patient geometry that would deliver the best treatment. Using the back propagation simulations is suggested as a means to find this optimal location with a single simulation. The back propagation results for patient 1 and patient 2 showed that the shape of the phase BPPD followed the BPAP in identifying the region over which the best location would be found for the transducer's position. For patient 2 only 2.5° separates the optimal angle from the BPAP and BPPD graphs. This translated into the agreement of the BPCP graph and BPAP in the position of the optimal transducer placement, since the BPCP includes the effect of the phase variation with the pressure amplitude. The phase BPPD graph for patient 1 shows an optimal position at -40° which is 17.5° removed from the optimal

position from the BPAP graph. The BPCP graph and BPAP graph for patient 1 had differing maximum value locations. The simulation at the rotation angle at which BPCP was maximum resulted in the highest focal target gain but a lower overall maximum gain than for the angle at which the BPAP was maximum.

For patient 3 the ribs had a significant impact in lowering the average received amplitude over the surface of the potential transducer location. The BPAP maximum value was 50% less than that obtained from the simulations for patient 1 and patient 2. Another difference was that the variation in the BPAP across the angular locations was small; only 7% compared to 15% for patients 1 and 2. The transducer location chosen on the basis of maximising BPAP did not achieve the largest possible gain. Combining the effects of phase in the BPCP graph resulted in maximum and minimum values at rotation angles that were different from the BPAP graph. The forward simulations at corresponding angles to maximum and minimum BPCP, 13° and -22.5°, resulted in the highest and lowest pressure gains of all the forward simulations undertaken. However, the lower pressure values at -22.5° could also be attributed to the lower resolution of 370 μm used in the simulation. Another simulation using 246.7 μm would need to be conducted to verify this.

The back propagation from the point source at the focus is equivalent to the forward propagation from the transducer surface to the focal point based on the spatial reciprocity of the acoustic field [142]. The complex pressure received at the surface of the transducer reflects the forward propagation better than the average pressure amplitude, therefore, it is more likely to find an optimal location for the maximum pressure at the target point.

6.5 Conclusion

The simulations undertaken in this chapter show that there is a significant change in the pressure obtained at the target tumour when changing the position of the transducer around the patient. For patient 1 the reduction in target pressure between the simulation at the rotation angles of maximum BPCP and that at

minimum BPCP was nearly 61%, for patient 2 it was 37% and for patient 3 it was $> 60\%$. This would be significant when treating patients using HIFU ablation.

The presence of ribs in the beam path in patient 3 results in the fragmentation of the focal volume which reduced the focal pressure. The use of the complex pressure was successful in obtaining a position for the transducer that gave the least fragmentation among the tested forward simulations.

These results show that a treatment planning step that would determine the optimal position of the transducer could be implemented by undertaking a back propagation simulation. The complex pressure received at the surface of the transducer for various locations defined in the simulation can then be used to select the optimal position. This would enable the physician to select an appropriate acoustic window to target for the treatment.

7

Effects of Speed of Sound Variations

The acoustic properties for tissue can vary from one patient to another, therefore for any model to be used for treatment planning it is necessary to assess its sensitivity to the change in tissue properties. In a previous study by Suomi et al [100] the change of speed of sound was found to have the most impact on the resulting HIFU focal region, therefore for this study the speed of sound was selected as the property to be varied in the simulations. In this chapter the sensitivity of one of the patient models to changes in the speed of sound for three tissue types is first presented. Then a further simulation is undertaken with a 1% variation in speed of sound values for both fat and muscle. The last section compares the significance of refraction from fat to reflection effects from bone in the pressure results for a different patient model.

7.1 Speed of Sound Variations

An extensive literature search was carried out to identify a range of measured values for the speed of sound in bone, muscle and fat. The values considered were from measurements at 37°C or in-vivo for human tissue. Following Duck in assuming minimal dispersion in soft tissues in the ranges of 1-15 MHz [115], values for speed of sound for fat and muscle measured at 2.25 MHz and 5 MHz are used here for simulations conducted at 0.95 MHz. The speed of sound for kidney was fixed,

because a previous study found that varying the speed of sound in the kidney by ±10 m/s, which corresponds to ±2 standard deviations (SD) [143], did not result in a significant change in focal pressure within the kidney [100]. The speed of sound for fat was selected as a combination of subcutaneous and renal fat. The range of values for subcutaneous fat were obtained from measurements by Errabolu et al on 19 samples [144]. The values were read from a graph included in the publication. For renal fat two sources were used. One was from measurements by Ritchie et al [73] on 10 samples of excised fat which resulted in a value of 1461 ± 27 m/s; the other from Turnbull et al [143] with values of 1407 ± 13 from 25 samples. The values were pooled using the formulae below for mean and standard deviation respectively:

$$M_{pooled} = \frac{\sum_{i=1}^{N} n_i M_i}{\sum_{i=1}^{N} n_i} \tag{7.1}$$

where n_i and M_i are the sample size and the mean value of the i^{th} group.

$$SD_{pooled} = \frac{\sum_{i=1}^{N}((n_i - 1)SD_i{}^2)}{\sum_{i=1}^{N}(n_i - 1)} \tag{7.2}$$

where n_i and SD_i are the sample size and the standard deviation of the i^{th} group.

The result was a combined mean and standard deviation of 1425 ± 16 m/s. All values are shown in figure 7.1.

The values for muscle were found from the review by Goss et al [145] which references in-vivo measurements by Ludwig and Struthers [146] on human biceps with a range of 1515-1587 m/s from 5 subjects, calf muscle with a range of 1500-1610 m/s from 4 subjects and quad muscle with a range of 1504 - 1563 m/s from 4 subjects. The full range using the values from these three muscles was selected as 1500-1610 m/s.

The rib bones are classed as flat bones which have a different structure from long bones and a relatively thin cortical shell sandwiching the cancellous internal structure similar to skull bone. Therefore, for the sensitivity simulations the speed of sound values were changed to those obtained from skull bone measurements from Fry and Barger with a value of 2840 ± 158 [147].

The maximum and minimum values for the speed of sound for bone and fat were chosen to be at ±2 SD. The values for muscle were selected as the minimum and

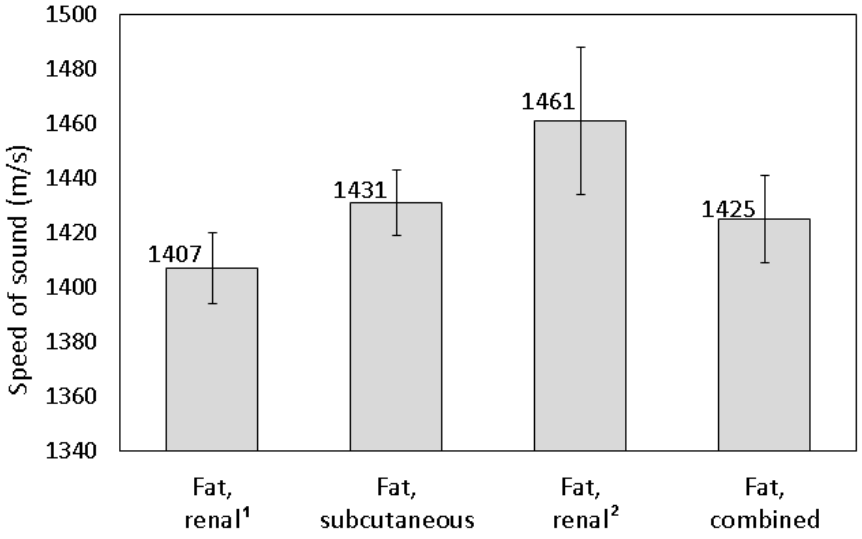

Figure 7.1: The calculation of the speed of sound for fat. The pooled speed of sound values for fat using renal fat[1] [143], subcutaneous fat [144] and renal fat[2] [73]

maximum values from the range of 1500-1610 m/s. Table 7.1 gives the values used in the simulations.

Medium	Speed of sound (m/s)			Density	Attenuation
	Min	Mean	Max	(kg/m^3)	(dB/cm @ 1 MHz)
Bone	2524	2840	3156	1908	20.00
Tissue (Muscle)	1500	1555	1610	1055	0.60
Fat	1393	1425	1458	950	0.48
Kidney	1560			1050	1.00
Water	1520			1000	0.00217

Table 7.1: Acoustic properties for different tissue types. Minimum, mean and maximum values are listed for human bone, muscle and fat.

7.2 Speed of Sound Sensitivity Simulations

The CT scan selected for the simulations was from patient 5.29, table 5.1. In order to maintain the 6 PPW resolution for the simulation a revised grid spacing was used based on the updated minimum and maximum speed of sound. The spatial resolution for the simulation was selected as 232.2 μm with a temporal resolution of 11 ns. The position of the transducer was the same as that used

in chapter 5. Figure 7.2 provides a 3D plot of the orientation of the transducer with respect to the patient CT scan.

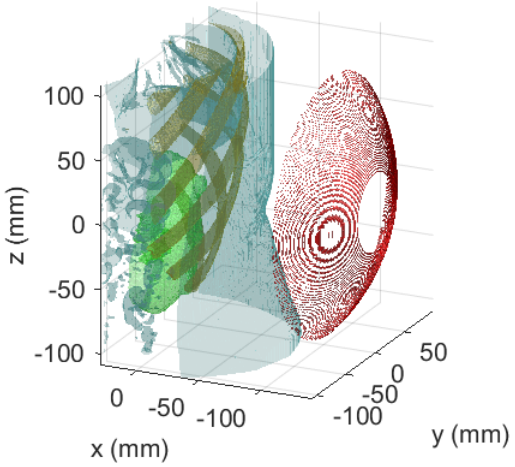

Figure 7.2: The transducer position relative to the medium derived from the CT scan for patient 5.29.

Seven simulations were undertaken using the speed of sound values shown in table 7.1. The mean speed of sound values for all tissue types were used for one simulation, then the speed of sound was varied for fat, muscle or bone individually in the other six simulations by using the minimum then the maximum values. These simulations will be described using the numbers from 1 to 7. For example simulation 2, uses the minimum speed of sound for muscle and mean speed of sound values for fat and bone.

The pressure gain obtained from the simulations in the horizontal focal plane is shown in figure 7.3. The plots show the pressure values overlaid on the CT scan structure with a fixed colour map for the pressure gain across the plots. The highest pressure values in this plane occur in the simulations that used the minimum muscle value and maximum fat value, simulations 2 and 5.

The simulation results for the pressure gain at the required focal point and at the highest pressure point are shown in table 7.2 along with the shift in the maximum pressure point within a volume of 30 mm x 26 mm x 20 mm around the target point. This smaller volume was selected because for simulations 1, 3, 4 and 7 the maximum pressure was recorded in muscle at the interface with the rib bone at a distance of 21 mm away from the focal target. The table shows that the pressure gain was

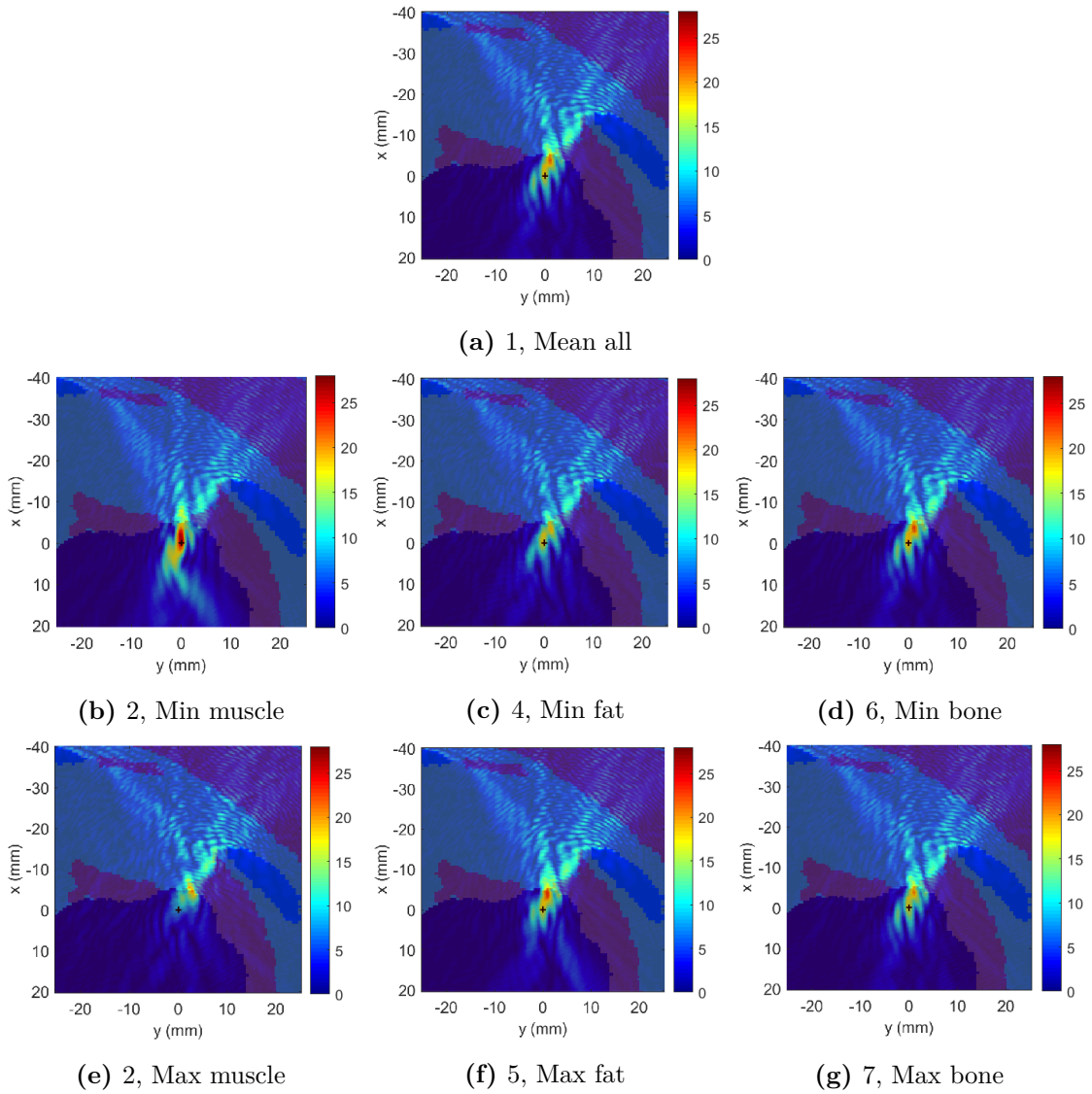

(a) 1, Mean all

(b) 2, Min muscle **(c)** 4, Min fat **(d)** 6, Min bone

(e) 2, Max muscle **(f)** 5, Max fat **(g)** 7, Max bone

Figure 7.3: The axial plane showing the pressure gain overlaid on the tissue structure for each of the simulations with different speed of sound settings. The simulations are referenced using simulation identifiers from 1 to 7. (a) Mean speed of sound values for all tissues, (b) minimum value for muscle, (c) minimum value for fat, (d) minimum value for bone, (e) maximum value for muscle, (f) maximum value for fat and (g) maximum value for bone. Tissue colours correspond to: dark red for kidney, red for fat, green for tissue and dark blue for water. The colour bar shows the pressure gain. The HIFU focal point target location is marked with a black cross

reduced by 29% to a value of 20 for simulations 3 and 4 with 'minimum fat' and 'maximum muscle' speed of sound compared to a pressure gain of 28 from simulation 2 with 'minimum muscle' speed of sound. The next highest maximum gain value is for simulation 5 with 'maximum fat' speed of sound. The two simulations with the

highest pressure gain, simulation 2, 'minimum muscle', and 5, 'maximum fat', are the ones with the smallest difference between the values of speed of sound for fat and muscle. The ratio for the speed of sound between muscle and fat for simulation 2 is 105% and for simulation 5 is 107%. This contrasts with the lowest in pressure gain, simulation 3, 'maximum muscle', and 4, 'minimum fat', where the ratio increases up to 113% and 112% respectively, which will result in the increased refraction of the ultrasound wave as it passes from one medium to the other. The shift in the position of the maximum pressure point agrees with the results for the highest pressure values with simulation 2, 'minimum muscle' giving the smallest shift and simulation 5, 'maximum fat', following it. Simulations 1, 'mean all', and simulation 6, 'maximum bone' were similar in shift and maximum gain values. Changing the speed of sound value for bone to a minimum of 2524 m/s in simulation 6 reduced the reflection at the bone interface, this caused the maximum pressure gain to occur nearer the target and not at the bone interface. However, within the smaller volume surrounding the target a bigger shift of 3.9 mm was recorded for simulation 6, 'minimum bone' compared to 2.7 mm from simulations 1, 'mean all' and simulation 7, 'maximum bone'. The worst performance with the highest shift values of 5.6 mm and 5.8 mm, was again recorded at simulations 3, 'maximum muscle', and 4, 'minimum fat'.

Simulation ID	Simulation condition	Max. gain	Gain at target	Max gain in volume	Shift (mm)			
					x	y	z	R
1[1]	Mean all	24	16	22	-2.1	1.2	1.2	2.7
2	Min muscle	28	26	28	0.5	0	0.7	0.9
3[1]	Max muscle	22	8	20	-4.7	3	-0.5	5.6
4[1]	Min fat	23	16	20	-5.3	1.6	-1.6	5.8
5	Max fat	27	17	27	-0.5	1.2	1.6	2.1
6	Min bone	22	18	22	-3.7	1.2	0	3.9
7[1]	Max bone	25	16	22	-2.1	1.2	1.2	2.7

Table 7.2: The results of the simulations showing the pressure gain at the maximum pressure point in the simulation, the pressure gain at the required focal point and the shift in the focal point. x is the axial axis, with y the lateral and z the elevation axes, R is the euclidean distance. Simulations marked [1] are ones where the maximum pressure gain was recorded in muscle at the rib bone interface, 21.0 mm away from the target. The shift value was calculated using the maximum pressure within a volume of 30 mm x 26 mm x 20 mm around the target point.

To observe the fragmentation of the focal volume the iso-surface at the half pressure value was plotted and can be seen in figure 7.4. It can be seen that in all plots the focal volume is fragmented. The least fragmented is the half pressure volume for simulation 2, the simulation that used the minimum speed of sound for muscle, shown in figure 7.4(b). The half pressure volume calculation used the maximum pressure value obtained from within a volume of 30 mm x 26 mm x 20 mm around the focal target.

In order to quantify the degree of variation in the focal volume three metrics were considered. The first looks at the second moment of the half pressure distribution around the target focal point normalised by that achieved from a simulation of a homogeneous non-attenuating medium. This method was used to capture the fragmentation and spread of the half pressure values. The reference simulation in the homogeneous medium used the speed of sound of water at 37°C, 1520 m/s and will be referred to as the water simulation. To do this the pressure values from the water simulation were interpolated into the grid of 232.2 μm resolution used in the sensitivity simulations. Figure 7.5 displays the -6 dB iso-surface volumes of the simulation in the water and the simulations using the maximum speed of sound for fat and muscle. The second moment of the half maximum pressure distribution around the target point were calculated for all the simulations. The value for the water simulation was used as a reference.

$$\mu_{(-6dB)} = \frac{\sum r^2 p(p > 0.5 \times p_{max}) dxdydz}{\sum r^2 p_w(p_w > 0.5 \times p_{w_{max}}) dxdydz} \tag{7.3}$$

where $r^2 = (x - x_f)^2 + (y - y_f)^2 + (z - z_f)^2$, x_f, y_f, z_f are the coordinates of the target focal point, p_w is the pressure resulting from the water simulation.

The other two metrics describe the spatial relationship of the -6 dB volumes obtained from the sensitivity simulations with the -6 dB target volume obtained from the water simulation. Figure 7.6 gives a representation of the possible configurations of the obtained half pressure volume relationship to the target volume V_T. The metrics used to define the efficiency of the pressure distribution in the focal volume were: the percentage of the target half pressure volume that is covered by the

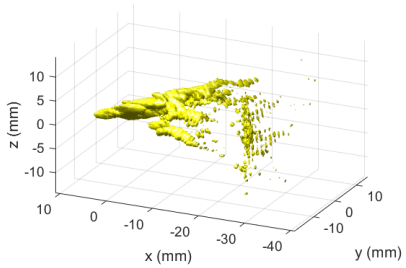

(a) 1, Mean all

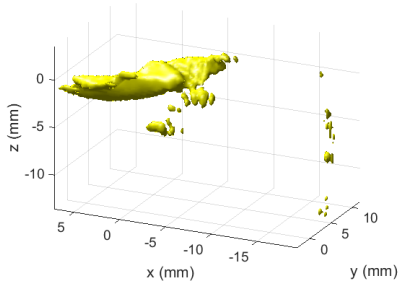

(b) 2, Min muscle

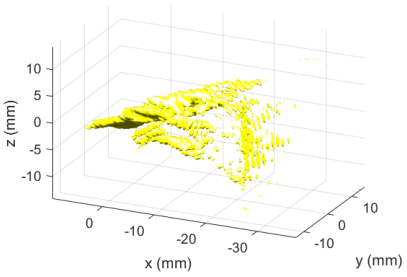

(c) 3, Max muscle

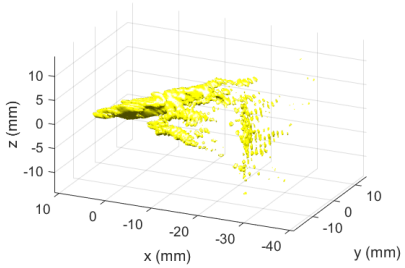

(d) 4, Min fat

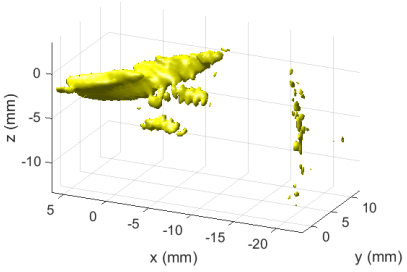

(e) 5, Max fat

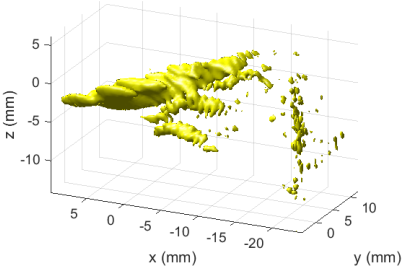

(f) 6, Min bone

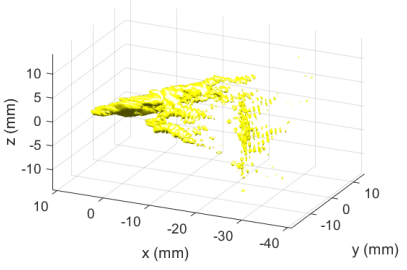

(g) 7,Max bone

Figure 7.4: The half pressure iso-surface, 61.5 mm x 111.9 mm x 106.8 mm volume, the simulations have different speed of sound values. (a) Mean speed of sound for all tissue, (b) minimum value for muscle, (c) minimum value for fat, (d) minimum value for bone, (e) maximum value for muscle, (f) maximum value for fat and (g) maximum value for bone. The -6 dB pressure for simulations 1, 3, 4 and 7 was calculated from a volume of 30 mm x 26 mm x 20 mm around the target.

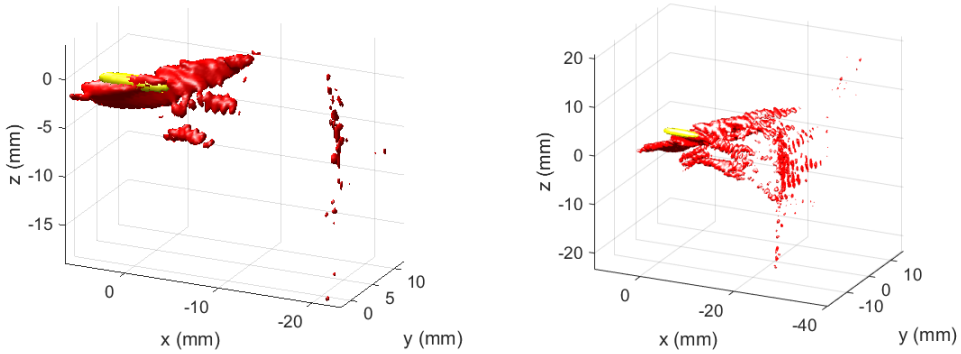

Figure 7.5: The -6 dB iso-surface for the JC-200 simulations over a volume of 70.1 mm x 111.9 mm x 106.8 mm. The yellow surface in both plots shows the -6 dB iso-surface of the simulation using a homogeneous non-attenuating medium with sound speed of 1480 m/s. The red surface is the volume for the simulation using (a) the maximum value for speed of sound for fat. (b) the maximum speed of sound for muscle. Speed of sound values are shown in table 7.1

half pressure volume from the simulation (V_{in}/V_T) and the percentage of the half pressure within the target volume compared to the total volume (V_{in}/V_{tot}).

Table 7.3 shows the second moment around the target for the simulations ($\mu_{(-6dB)}$), the -6 dB volume, the -6 dB volume of overlap V_{in}, the percentage of target covered (V_{in}/V_T), and finally the percentage of (V_{in}/V_{tot}). The high values of 200 mm^3 for the half pressure volume for simulations 1, 3, 4, 6 and 7 reflect the defocussing of the HIFU beam due to the presence of the bone in the ultrasound path and the refraction in the speed of sound between fat and muscle. For simulation 2, 'minimum muscle' and simulation 5, 'maximum fat' the smaller relative change in the speed of sound between fat and muscle reduced the refraction, which resulted in a tighter pressure distribution at the focal region with smaller volumes of 46 mm^3 and 104.7 mm^3 respectively. The smaller $\mu_{(-6dB)}$ value reflects that simulation 2, has a tighter distribution than simulation 5. Simulation 3, 'maximum muscle', shows the worst efficacy in the distribution of the pressure, since V_{in} is only 0.4% of V_{tot}. V_{in} covers only 13% of V_T by far the smallest overlap among the simulations. On the other hand simulation 2, 'minimum muscle', shows the smallest value of $\mu_{(-6dB)}$, which reflects the best focussing result among the simulations. It also records the highest percentage of V_{in} to V_{tot} ratio at 9.3%. Simulation 4, 'minimum

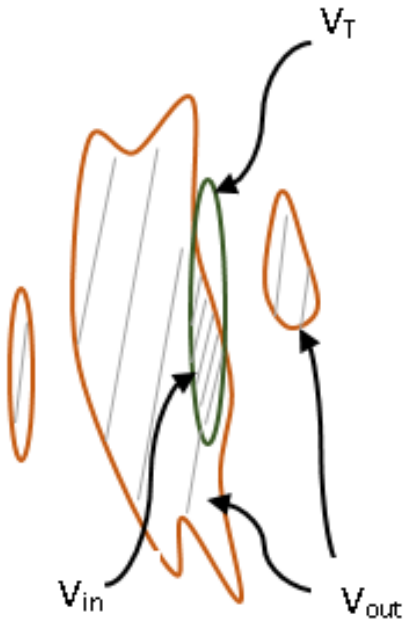

Figure 7.6: Diagram showing the volume configurations between the target -6 dB pressure volume obtained from the water simulation and the volume achieved from the patient model simulations. Where V_T is the target volume, V_{in} is the volume above -6dB that lies inside V_T, V_{out} is the volume that falls outside the target volume. The total volume $V_{tot} = V_{in} + V_{out}$

fat' recorded a higher overlap percentage of 87% compared to 69% for simulation 5, 'maximum fat'. However, it also shows a lower efficiency with a 3% ratio of (V_{in}/V_{tot}) compared to 5.8% for simulation 5. The higher overlap percentage is due to the bigger -6 dB volume in simulation 4 due to defocussing.

7.3 Thermal Simulations

Thermal simulations were undertaken using the acoustic simulation results for a source pressure of 120 kPa. The peak temperature value for all simulations was found to be at the muscle rib interface. The results displayed in table 7.4 show the absolute maximum temperature, the maximum temperature in the kidney, the temperature obtained at the target focal point and the size of the resulting lesion in kidney and muscle tissue.

The results show that for a source pressure of 120 kPa the only lesions created

Sim. ID	Simulation condition	Target Gain	$\mu_{(-6dB)}$	-6 dB (mm^3)	Overlap (mm^3)	Percent. (V_{in}/V_T)	Percent. (V_{in}/V_{tot})
1	Mean all	16	252	225.8	7.9	89%	3.4%
2	Min muscle	26	46	84.2	7.8	88%	9.3%
3	Max muscle	8	264	259.0	1.1	13%	0.4%
4	Min fat	16	272	257.0	7.8	87%	3.0%
5	Max fat	17	68	104.7	6.1	69%	5.8%
6	Min bone	18	200	197.9	7.9	89%	4.0%
7	Max bone	16	207	202.9	7.6	86%	3.8%

Table 7.3: The normalised second moment of the -6 dB pressure $\mu_{(-6dB)}$. The size of the -6 dB pressure volume, the volume V_{in}, the percentage overlap of V_{in} to V_T. The percentage of V_{in} to V_{tot}. The target volume was 8.9 mm^3. For all calculations of -6 dB pressure the maximum pressure recorded for simulations 1, 3, 4 and 7 was from a volume of 30 mm x 26 mm x 20 mm around the target point.

Sim. ID	Simulation condition	Maximum Temp (°C)	Max kidney Temp (°C)	Temperature @ target (°C)	Lesion volume (mm^3)	
					Kidney	Muscle
1	Mean all	70.3	56.2	49.2	0	0.2
2	Min muscle	68.8	68.4	62.5	12.3	0.1
3	Max muscle	71.4	51.0	40.2	0	0.3
4	Min fat	70.2	52.0	47.9	0	0.1
5	Max fat	71.0	66.9	49.8	10.6	0.3
6	Min bone	70.4	57.1	49.8	0	0.1
7	Max bone	70.5	56.4	48.6	0	0.2

Table 7.4: The maximum temperature achieved for the thermal simulations, the temperature at the required focal point and the resulting volume for the thermal lesion created in the kidney and muscle. No lesion was created in fat.

in the kidney were in simulation 2, minimum muscle and simulation 5, maximum fat. These are the two simulations with the smallest difference between the speed of sound for fat and muscle. The other lesions created in muscle for all the simulations are found near the bone of the rib cage. The change in the speed of sound for bone from minimum to maximum creates only a 1°C change in the resulting temperature.

The plots for the minimum, mean and maximum sound speed settings for muscle are shown in figure 7.7. The figure shows the horizontal slice through the required focal point. The plots show that the position of the maximum temperature in the focal plane is shifted towards the transducer when the maximum speed of sound for muscle was used. This follows the pressure distribution shown in figure 7.3. The

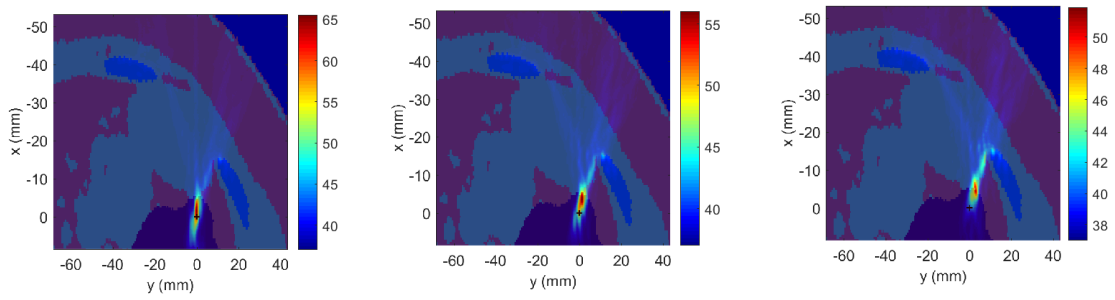

Figure 7.7: The temperature plots for the thermal simulation result, simulations at (a) minimum speed of sound for muscle, (b) mean speed of sound value for muscle, and (c) maximum speed of sound value for muscle

temperature achieved at this plane from simulation 2 (minimum speed of sound) is higher by 10°C than that achieved from simulation 3 (maximum speed of sound).

7.4 Effects of a 1% change in Speed of sound for Fat and Muscle Tissue

The change in the speed of sound for muscle based on its orientation was found to vary by up to 1% based on measurements by Goldman and Richards [148]. A simulation was undertaken to investigate the change in focal pressure resulting from a variation of 1% in the speed of sound for both fat and muscle. The simulation selected as the reference was simulation 5, maximum speed of sound for fat of 1458 m/s and mean speed of sound for muscle of 1555 m/s. Choosing the case giving the biggest relative difference in speed of sound between fat and muscle an increase of 1% for fat resulted in a value of 1444 m/s and a decrease of 1% for muscle resulted in 1572 m/s. This new simulation is referred to as simulation 8. The horizontal focal plane is shown in figure 7.8(a) with the -6 dB pressure volume in 7.8(b). The results for maximum pressure gain and focal gain are displayed in table 7.5.

The maximum pressure was recorded at the tissue interface with the bone at a distance of 21 mm from the target focal point, therefore the maximum gain in volume value listed in table 7.5 was obtained from a volume of 30 mm x 26 mm x 20 mm around the target point. This was the value used as a comparison to

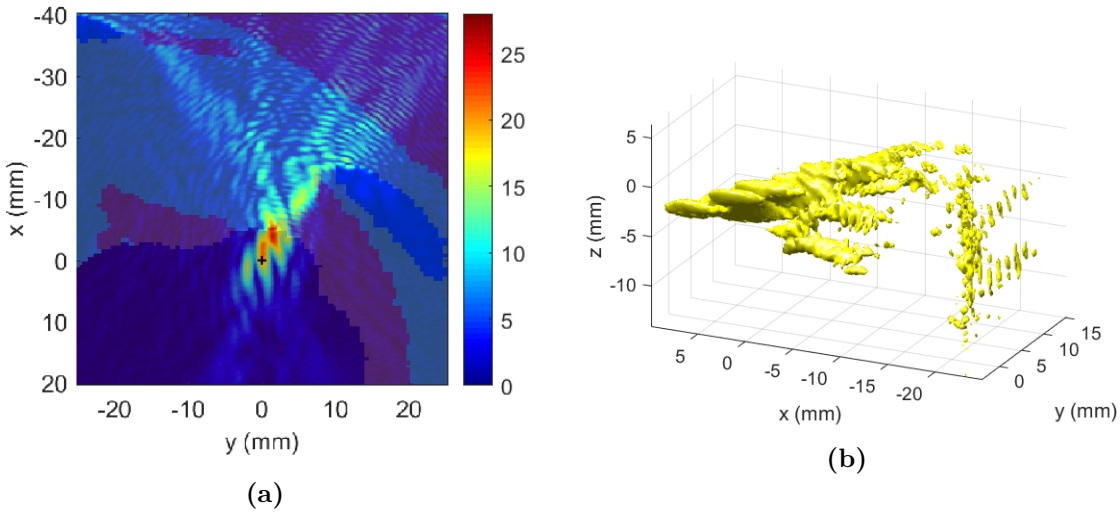

Figure 7.8: Results for simulation 8, (a) axial focal plane with the pressure gain overlaid on the patient structure, the colours correspond to dark red for kidney, orange for fat, green for muscle and blue for bone and dark blue for water. (b) The iso-surface of the -6 dB volume. The maximum pressure used for the -6 dB volume calculation was recorded within a volume of 30 mm x 26 mm x 20 mm around the target focal point.

Simulation ID	Maximum gain	Gain at target	Max gain in volume	Shift (mm)			
				x	y	z	R
8	29	19	25	-7.4	3.5	-1.4	8.3

Table 7.5: The results of the simulation showing the pressure gain at the maximum pressure point in the simulation, the pressure gain at the required focal point, and the maximum pressure gain in a volume of 30 mm x 26 mm x 20 mm around the target.The shift is the distance from the maximum pressure within the smaller volume to the target focal point, x is the axial axis, with y the lateral and z the elevation axes, R is the euclidean distance.

the maximum gain from simulation 5. The maximum gain of 25 represents an 8% reduction from the value in simulation 5. However, the shift in its position by 8.3 mm is significant in ablation treatments. The presence of the rib bone was again relevant in increasing the defocussing.

7.5 Effects of Fat on HIFU Focus compared to Bone in a Patient Model

Another patient model was used to test whether the effects due to speed of sound differences between fat and muscle can be as detrimental to the HIFU focal pressure as the reflections at the bone interface. In a previous study refraction was found to

have a significant impact on the defocussing of the HIFU beam when comparing simulations across 3 patient models [100]. In the present study one patient model was used for two simulations, one had the fat layer assigned the properties of muscle, the other had the bone layer defined as muscle. The patient model was based on the CT scan of patient 5.01 from the kidney ablation clinical trial [75]. The simulations used the acoustic properties in table 3.1 and the grid settings in chapter 5. The placement of the transducer in the simulation resulted in the beam passing through the patient's lung, however the lung was not given lung acoustic properties but assigned properties of water. This was done because undertaking an accurate representation of treatment delivery through lung was not the aim of the simulations, yet the goal was to provide a fixed condition to compare between the effects of bone and fat.

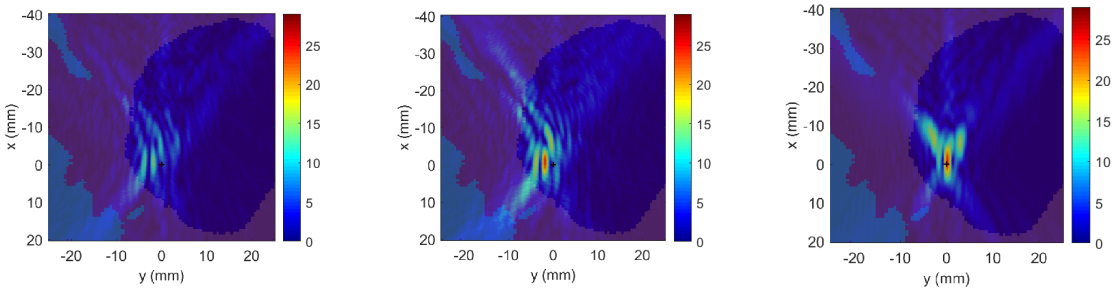

(a) **(b)** **(c)**

Figure 7.9: The horizontal focal plane showing the pressure gain overlaid on the tissue structure for each of the simulations using (a) Values for bone, fat and muscle. (b) Bone with properties of muscle. (c) Fat with properties of muscle. Tissue colours correspond to: dark red for kidney, red for fat, green for muscle and dark blue for water. The colour bar shows the pressure gain. The HIFU focal point target location is marked with a black cross.

The focal plane plots in figure 7.9 show the change in focal gain between three simulations using the patient CT scan for patient 5.01 with the tumour in the upper lobe of the left kidney. The lowest pressure value is seen in figure 7.9(a) which uses the relevant acoustic properties for fat, muscle and bone. Figures 7.9(b) and 7.9(c) show a significant increase in pressure gain for both the simulations where either bone or fat were replaced with muscle.

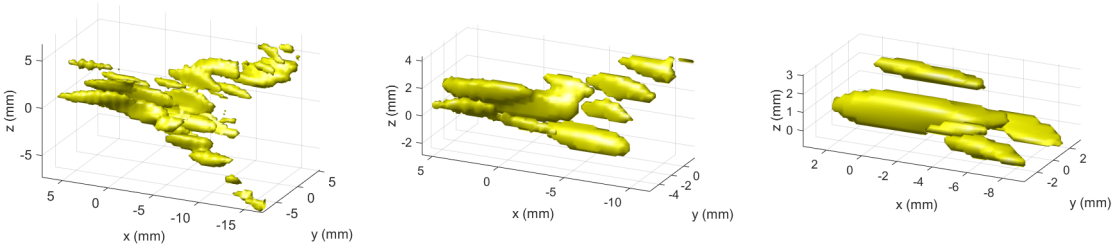

(a) **(b)** **(c)**

Figure 7.10: The half pressure (-6dB) iso-surface volume for the simulations of patient model 5.01. (a) Values for bone, fat and muscle. (b) Fat and muscle. (c) Bone and muscle.

The fragmentation seen in figure 7.10(a) is the result of the reflection at the bone interface and the refraction from the change in the speed of sound of muscle and fat. The fragmentation was markedly reduced in 7.10(b) and 7.10(c), which is evident in the increase in the maximum pressure gain given in table 7.6. For the simulation in which bone properties were replaced with muscle the maximum pressure increased by 70%, because reflection at the bone interface was effectively removed. The maximum pressure also increased when replacing fat with muscle by 59%, where the effects of refraction from fat were removed. This shows that the effect of refraction due to fat muscle interface is as significant as that of reflection at bone interfaces. The other interesting observation is that the gain at the required focal point is 3 times higher when the simulation is run with only bone and muscle compared to when using only fat and muscle. This is because the biggest shift in the maximum pressure of -1.23 mm is in the axial direction as compared to a shift of -1.73 mm occurring in the lateral direction with fat and muscle. This occurs because the axial beam length of the transducer is approximately 4 times higher than the lateral length. The axial shift value of -1.23 mm is within the -3 dB focal region of the transducer. The ratio of the values used for speed of sound of muscle to fat is 109% which results in a 5° refraction from the incidence beam at a 45° angle.

Simulation condition	Maximum gain	Gain at target	Shift(mm)			
			x	y	z	R
All tissue	17	5	-0.25	-1.73	-0.49	1.8
Fat and muscle	29	7	-0.25	-1.73	-0.49	1.8
Bone and muscle	27	22	-1.23	0.25	-0.49	1.3

Table 7.6: The results of the simulations showing the pressure gain at the maximum pressure point in the simulation, the pressure gain at the required focal point and the shift in the focal point. x is the axial axis, with y the lateral and z the elevation axes, R is the euclidean distance

7.6 Discussion

In the context of renal ablation, even relatively small changes in speed of sound have been found to have a significant impact in changing the resulting focal volume, pressure gain achieved and the position of the maximum pressure point.

The difference in speed of sound for fat from maximum to minimum is 4.4%, however the corresponding simulations using these values result in a pressure gain that is lower by 26% for the maximum speed of sound simulation compared to the minimum speed of sound simulation. For the simulations where the speed of sound of muscle is varied, an increase of 7% from a minimum of 1500 m/s to a maximum of 1610 m/s results in an decrease in the pressure gain of 29%. Differences in speed of sound from fat to muscle were critical in these simulations. The simulations with the best pressure gain and focal volume distribution are those with the smallest difference between the speed of sound of the fat layer and the muscle layer. These results highlight the importance of the relative difference of the speed of sound between tissues in the propagation path of ultrasound with refraction having a significant impact in defocussing of the beam as found by Suomi et al [100].

The model employed here was simplified by using the same acoustic properties for subcutaneous and peri-nephric fat. Other abdominal tissue was defined as muscle. This was also a simplification since other tissue types such as spleen and liver were not considered. However, the values selected for the range of the speed of sound for muscle are wide enough to include values for those tissue types.

CT scans obtained from patients before treatment could be processed to obtain patient-specific speed of sound values. In order to determine approximate values

for the patient some studies have been looking at extracting the speed of sound for the tissue from the CT scan using density values. The density can be determined from the Hounsfield Units (HU) knowing two reference values [149] or standard calibration phantoms for the HU-density relationship [150]. Mast was able to find a linear fit between the density and speed of sound for a range of soft tissues [111]. This has been tested for the aberration correction of ultrasound images of phantom and clinical images by Fontanarosa et al [150]. They used the CT image to extract the density and then used a linear fit to obtain the speed of sound corresponding to the density. However, this approach would need to be proceeded with updated measurements for various tissue types.

The results from simulation 8 show that a 1% change in speed of sound for fat and muscle results in an acceptable 8% decrease in maximum gain. However, the 8.3 mm shift in the position of the maximum gain obtained from the simulation would result in a significant shift in the lesion location. Therefore, a smaller speed of sound variation value would be required in this instance to obtain comparable ablation outcomes. In the present patient model the defocussing of the HIFU beam due to the presence of bone has contributed to increasing the shift value.

The results from section 7.5 show that even without the presence of bone in the ultrasound path a significant change in the focal pressure can occur due to the difference in speed of sound in soft tissue. Therefore, other simulations could be undertaken with more points for speed of sound variation using a patient model without bone in the ultrasound path to ascertain the sensitivity to soft tissue changes independent of bone interference.

These simulations captured the effects of the heterogeneity between the layers, but did not capture the heterogeneity within the layers. Fat and muscle layers are non-uniform, and other work has shown that single layers of muscle and fat cause aberrations in the focal plane [151]. There is anisotropy in the structure of the muscle fibres as well as the presence of fat infiltration and connective tissue. The speed of the sound wave within the muscle was found to be dependent on the orientation of the muscle fibres with respect to the ultrasound beam [115].

A variation of up to 1% was measured by Goldman and Richards [148]. In the abdominal wall muscle groups are varied and have different orientations depending on the position of the group surrounding the abdomen [151]. All these variations are complex and assuming uniform properties across the layers is a simplification that is required to enable the current simulation.

There is a need to perform more measurements for the speed of sound through different human tissue types. The values from literature used for the speed of sound in muscle were for leg and arm muscles. It was difficult to find a wide range of measurements for human tissue.

7.7 Conclusion

The sensitivity of acoustic simulations to the change in the speed of sound for bone, muscle and fat was studied using a patient model. The target focal point was placed at a tumour in the left kidney at an interpolar position. The model was found to be sensitive to the change in the speed of sound within the range studied. A decrease of 4% in the speed of sound for fat resulted in a 26% decrease in pressure gain. For an increase of 7% in speed of sound of muscle the pressure gain reduced by 29%. The most significant changes in the simulation results were found to be due to the divergence in the speed of sound of fat and muscle. The difference in speed of sound between fat and muscle of 175 m/s resulted in a 29% decrease in maximum focal pressure compared to the simulation where the difference in sound speed was 75 m/s. A change of 1% in speed of sound for fat and muscle resulted in an 8% decrease in maximum pressure and an 8 mm shift in its location.

Another patient model was used to compare the defocussing resulting from heterogeneity in soft tissue layers to that resulting from the presence of bone. Two simulations, one with bone assigned properties of muscle and the other with fat assigned the muscle properties were undertaken. The impact of the difference in the speed of sound of muscle and fat on the focal region was found to be comparable to reflection effects at the bone soft tissue interface. An increase of 59% in the focal

pressure resulted due to the replacement of fat with muscle properties compared to a 70% increase with bone replacement.

8 Conclusion and Future Work

8.1 Conclusion

The aim of the present thesis was to investigate the feasibility of developing a treatment planning methodology for HIFU renal tumour ablation using the open source software k-Wave. The findings show that a treatment planning tool could aid the clinician in choosing appropriate treatment power choices and enable the selection of an optimal position for the transducer to maximise treatment delivery. They also highlight the importance of using accurate speed of sound values for the tissue structures in the patient model.

The details of the model including the simulation tool used, k-Wave, is described in chapter 3 alongside tests to obtain a suitable resolution for the acoustic simulations. A method to characterise a transducer using pre-focal radial scans was undertaken in Chapter 4. It was tested first on a 1.1 MHz research transducer in the laboratory and resulted in a good match for the pressure profile compared to the direct scan of the focal region. This method was then used to characterise the 0.96 MHz transducer on the JC-200 (HAIFU) clinical system in the Churchill Hospital, University of Oxford. Multiple pre-focal radial scans were undertaken using three power settings. The simulations undertaken for six of the radial scans gave varying results for the

position of the peak focal pressure and the pressure value, which could be due to the approximations used when finding the focal position of the transducer.

In chapter 5 the patient specific computer model was used to predict the outcome of kidney tumour ablation for patients treated in a previously conducted clinical trial with known outcomes. The CT scans for the patients were used to define the medium in the model with the relevant acoustic characteristics assigned. The simulation results showed that the powers required to reach ablation temperatures in the tumour are different for each patient based on the tissue structure of each individual. The results showed some agreement with clinical outcomes with one of the patient models, patient one, but did not mirror the clinical trial outcomes completely, which was most pronounced in the results for patient 3 where ribs were in the ultrasound propagation path. Using similar values of power to source pressure as obtained for the transducer characterisation obtained in Chapter 4 and assuming linear propagation, the simulation results showed that some of the patients were treated using power levels that were too high for the targeted tumour. The simulations indicated that the heating would have resulted in boiling within the target. In the trial B-mode hyperecho was used as a means to detect the onset of HIFU ablation. Whereas, hyperecho is mostly an indication that boiling has started to occur at the target tissue [53, 54]. The presence of lesions indicating boiling was mentioned in the histology assessment of the resected tumours from the clinical trial [75]. The results of the simulations suggest that use of patient specific models would aid the clinician in choosing power levels and treatment times in order to achieve suitable ablation outcomes. However, this ideally should be implemented along with improved treatment monitoring techniques that enable the detection of the onset of ablation.

Chapter 6 used back propagation of the wave from the target location to a surface corresponding to a set of potential positions for the transducer around an arc in order to obtain an optimal position for its placement. The method was tested on three patient models and was able to determine the optimal placement to achieve a maximum target pressure using the summation of the complex pressure

values received on the surface of the transducer. The position of the transducer was found to be significant for maximising the target pressure. The target pressure more than doubled in the simulation results for two patient models when comparing the optimal and worst transducer locations for each.

To test the applicability of the model with varying tissue compositions, in chapter 7 the sensitivity of the model to changes in the speed of sound for muscle, fat and bone was investigated. It was found that a 29% decrease in maximum pressure gain resulted from a 7% increase in the speed of sound of muscle. A similar decrease of 26% occurred with a 4% decrease the in speed of sound of fat. This significant change in the focal pressure, which also had an impact on the temperature profile within the patient model, was attributed to the change in the relative speed of sound between muscle and fat. Within the patient model tested a speed of sound measurement accuracy of $< 1\%$ was found to be required for the simulation model to achieve $< 10\%$ change in maximum pressure.

8.2 Future Work

8.2.1 Acoustic Properties Extraction from CT and MR Images

Based on the preliminary data from this study speed of sound variations better than 1% could be required for accurate models, however available data cover a wider range, up to 7% for muscle speed of sound values. As well as the requirement for more measurements for tissue properties, extracting these values from medical imaging could be investigated.

In order to determine the acoustic properties for the individual patient, knowledge about the tissue composition could be extracted from the patient's CT or MR images. Automatic segmentation for relevant organs, fat and muscle should be implemented beforehand. High resolution CT scan images were used by Aubry et al [149] to extract density and speed of sound for skull bone using reference values for water and maximum values for bone. Calibration phantoms for HU to density were used

by Fontanarosa et al [150]. The application of similar methods could be investigated for soft tissue property determination on ex-vivo tissue samples.

For MRI, segmenting tissue and defining tissue types quantitatively has been undertaken for breast [152], abdominal fat tissue [153–155], and thigh muscle and muscle fat infiltration [155]. An investigation needs to be done to identify the calibration required to translate the outcomes of segmentation methods into acoustic properties.

The use of MRI scans imposes an added consideration related to the imaging sequence used. The sequence required for tissue characterisation is selected based on the requirement to enhance the tissue contrast for selected tissue types. This means that the sequence has to be incorporated into the MRI scans used for patient screening.

8.2.2 Nonlinear Simulations

The simulations used in this thesis did not include nonlinearity, because the required grid size would result in computational requirements that would make running the simulations resource intensive and excessively time consuming. Nonlinear simulations may be important to give a more accurate characterisation of the propagation of the ultrasound wave within the body. It is important for ablation treatments since the pressures used are high and nonlinearity can occur. In Chapter 5 the results of the simulations showed that the treatment power used during the clinical trial would have resulted in boiling with evidence from the histological samples consistent with this. The nonlinear simulations could result in a more realistic simulation prediction of the effects of pre-focal heating in the peri-nephric fat.

The use of linear simulations was beneficial in allowing the use of pressure gain as a means to change the source pressure without re-doing the simulation. It was then used to identify power levels best suited to treat the specific patient. A comparison of linear and nonlinear simulation would be a good means to understand

the effects that nonlinearity has on the change in pre-focal and focal heating to ascertain the level of accuracy for the linear simulations.

8.2.3 Sensitivity to lateral motion and effect on aberration correction

The treatment of a tumour using HIFU requires the focal region to be scanned through the entire tumour volume. The extent of the movement depends on the dimensions of the tumour and mostly covers tens of millimetres. Simulations should be conducted to test for the effect of the movement of the transducer in the lateral and the elevation directions to cover the entire treatment volume. These would indicate whether the treatment parameters are suitable for the full volume to be treated. Any aberration correction with the use of a lens or a phased array would need to consider this lateral and elevation movement of the transducer as well.

It would be beneficial to investigate the ability to design a single lens that can be steered with the transducer to cover the ablation of the tumour volume. The challenge in designing a single acoustic lens is in making it work for the shift in the target location and the potential deformation.

8.2.4 Sensitivity to material properties

The analysis in chapter 7 looked at the effects changes in the speed of sound had on the obtained pressure and focal region. The speed of sound is only one of the properties which contribute to the propagation of ultrasound in the tissue. Changes in attenuation along the propagation path can also result in a corresponding change in pressure depending on the depth of the target. Increasing the attenuation will result in a loss of pressure, however it will also result in an increase of absorption acting to increase the temperature rise. It would therefore be useful to observe the sensitivity of the model to this change especially its impact in pre-focal heating. The change in density was also found to have an impact on the change in the pressure field although to a lesser extend than the speed of sound in transcranial simulations [108].

In addition, tissue properties change with heating. Understanding the impact of these changes during the treatment would be a valuable addition to the assumptions for computer modelling and treatment planning.

8.2.5 Characterising Tissue Deformation due to the change in Patient's Position

The CT or MRI scan are the sources for the patient derived tissue geometry that is used to define the media within the computer models. However, CT or MRI scans are normally performed with the patient lying on their back, whereas for HIFU treatments the patient can be rolled over on to their side. This change in position will result in deformation of the soft tissue structures in the abdomen, because the weight of the tissue will be shifted towards a different side of the body.

Before HIFU treatment is undertaken initial screening is also undertaken using B-mode imaging to test for the ability to view the tumour in treatment-like conditions [75]. This B-mode image is performed with the patient placed in the same position as would be used for the treatment. A CT/MRI to ultrasound image registration would need to be performed to obtain the required deformation in the CT/MRI scan that would reflect the change in the patient's position. First the slices of the CT/MRI images corresponding to the ultrasound images have to be found using a metric that identifies the similarity between the images. Second, landmark identification has to be undertaken for use in the registration and deformation of CT/MRI image. Then a deformable transformation model has to be implemented to follow the shape of the ultrasound image. [156, 157] The limitation of this technique is that it requires good quality B-mode images otherwise the registration would fail.

8.2.6 Experiment to Test k-Wave Simulations on Heterogeneous Media

In order to test the ability of the k-Wave model to characterise thermal heating accurately in a heterogeneous medium an ex-vivo setup could be used to verify the results of the simulations. The simplest test would consist of a phantom composed of two materials with different speed of sound values. A phantom similar

to that used by Mougenot et al [158] could be assembled. It is composed of a 3% agar gel with speed of sound of 1485 m/s and a polymer material with a higher speed of sound of 1528 m/s. A recent study validated the k-Wave model using a glycerol filled phantom in a water bath [159]. The study used 13.5 PPW to obtain comparable results to acoustic measurements. Another study used rabbit carcasses to validate k-Wave simulation results [102]. The simulations employed a layered approach to the resolution in the field of the HIFU transducer with the resolution increased as the grid neared the HIFU focus [102]. This approach of segmenting the domain into different resolution layers could be beneficial for use with large transducers such as the JC-200.

Testing a two medium phantom with bone or a bone like phantom would be useful in validating the elastic k-Wave model for ultrasound delivery through the ribs.

8.2.7 Validation in a Perfused Organ

Verification of acoustic and thermal simulations can be undertaken using a perfused organ model. This would provide the closest representation of in-vivo conditions by providing a functioning organ. The extent of resulting ablation can then be assessed using histology.

8.2.8 Development of a Treatment Protocol for Renal Ablation

To develop a treatment planning tool the clinical work flow has to be considered. The type of diagnostic images, whether MR or CT, have an impact on the type of segmentation used. The computer modelling has to be undertaken within a time frame that fits into the duration between the patient's scan and scheduled treatment date.

A test for the speed of the scan and the power required would need to be undertaken for each patient model. A similar assessment was undertaken for patients treated with ThermoDox by Gray et al [101].

A major consideration for any HIFU treatment is the monitoring method used. As mentioned in chapter 5 using a patient model to define the treatment settings for the procedure is not sufficient to guarantee successful lesion creation. The development of a monitoring technique that can detect lesion onset is critical. However, the combination of a planning tool and an ultrasound based monitoring technique could provide an effective alternative to the relatively expensive MRI guided HIFU treatment.

References

[1] J. G. Lynn, R. L. Zwemer, A. J. Chick, and A. E. Miller. "A New Method for the Generation and Use of Focused Ultrasound in Experimental Biology". In: *The Journal of General Physiology* 26.2 (Nov. 1942), pp. 179–193. URL: https://doi.org/10.1085/jgp.26.2.179.

[2] W. J. Fry. "Intense Ultrasound - A New Tool for Neurological Research". In: *The British Journal of Psychiatry* 100.418 (Jan. 1954), pp. 85–96. URL: https://doi.org/10.1192/bjp.100.418.85.

[3] W. J. Fry, F. J. Fry, J. W. Barnard, R. F. Krumins, and J. F. Brennan. "Ultrasonic Lesions in the Mammalian Central Nervous System". In: *Science* 122.3168 (Sept. 1955), 517 LP –518. URL: https://doi.org/10.1126/science.122.3168.517.

[4] E. S. Ebbini, H. Wang, M. O'Donnell, and C. A. Cain. "Acoustic feedback for hyperthermia phased-array applicators: aberration correction, motion compensation and multiple focusing in the presence of tissue inhomogeneities". In: *IEEE 1991 Ultrasonics Symposium,* Dec. 1991, 1343–1346 vol.2.

[5] D. S.Shimm, K. H. Hynynen, D. P. Anhalt, R. B. Roemer, and J. R. Cassady. "Scanned focussed ultrasound hyperthermia: initial clinical results". In: *International Journal of Radiation Oncology, Biology, Physics* 15.5 (Nov. 1988), pp. 1203–1208. URL: https://doi.org/10.1016/0360-3016(88)90205-2.

[6] E. S. Ebbini and G. Ter Haar. "Ultrasound-guided therapeutic focused ultrasound: Current status and future directions". In: *International Journal of Hyperthermia* 31.2 (Feb. 2015), pp. 77–89. URL: https://doi.org/10.3109/02656736.2014.995238.

[7] F. Wu, W.-Z. Chen, J. Bai, J.-Z. Zou, Z.-L. Wang, H. Zhu, and Z.-B. Wang. "Pathological changes in human malignant carcinoma treated with high-intensity focused ultrasound". In: *Ultrasound in Medicine & Biology* 27.8 (Aug. 2001), pp. 1099–1106. URL: https://doi.org/10.1016/S0301-5629(01)00389-1.

[8] K. Hynynen and F. A. Jolesz. "Demonstration of potential noninvasive ultrasound brain therapy through an intact skull". In: *Ultrasound in Medicine and Biology* 24.2 (Feb. 1998), pp. 275–283. URL: http://doi.org/10.1016/S0301-5629(97)00269-X.

[9] R. W. Ritchie, T. Leslie, R. Phillips, F. Wu, R. Illing, G. Ter Haar, A. Protheroe, and D. Cranston. "Extracorporeal high intensity focused ultrasound for renal tumours: A 3-year follow-up". In: *BJU International* 106.7 (Oct. 2010), pp. 1004–1009. URL: http://dx.doi.org/10.1111/j.1464-410X.2010.09289.x.

[10] M. Marinova, M. Rauch, M. Mücke, R. Rolke, M. A. Gonzalez-Carmona, J. Henseler, H. Cuhls, L. Radbruch, C. P. Strassburg, L. Zhang, H. H. Schild, and H. M. Strunk. "High-intensity focused ultrasound (HIFU) for pancreatic carcinoma: evaluation of feasibility, reduction of tumour volume and pain intensity". In: *European Radiology* 26.11 (Nov. 2016), pp. 4047–4056. URL: https://doi.org/10.1007/s00330-016-4239-0.

[11] I. De Cock, E. Zagato, K. Braeckmans, Y. Luan, N. de Jong, S. C. De Smedt, and I. Lentacker. "Ultrasound and microbubble mediated drug delivery: acoustic pressure as determinant for uptake via membrane pores or endocytosis". In: *Journal of controlled release : official journal of the Controlled Release Society* 197 (Jan. 2015), pp. 20–28. URL: https://doi.org/10.1016/j.jconrel.2014.10.031.

[12] A. Yudina and C. Moonen. "Ultrasound-induced cell permeabilisation and hyperthermia: strategies for local delivery of compounds with intracellular mode of action." en. In: *International journal of hyperthermia : the official journal of European Society for Hyperthermic Oncology, North American Hyperthermia Group* 28.4 (Jan. 2012), pp. 311–9. URL: https://doi.org/10.3109/02656736.2012.664307.

[13] R. Magnin, F. Rabusseau, F. Salabartan, S. Mériaux, J.-F. Aubry, D. Le Bihan, E. Dumont, and B. Larrat. "Magnetic resonance-guided motorized transcranial ultrasound system for blood-brain barrier permeabilization along arbitrary trajectories in rodents". In: *Journal of Therapeutic Ultrasound* 3.1 (2015), pp. 1–11. URL: http://dx.doi.org/10.1186/s40349-015-0044-5.

[14] T. Kobus, N. Vykhodtseva, M. Pilatou, Y. Zhang, and N. McDannold. "Safety Validation of Repeated Blood-Brain Barrier Disruption Using Focused Ultrasound." In: *Ultrasound in medicine & biology* 42.2 (Feb. 2016), pp. 481–92. URL: https://doi.org/10.1016/j.ultrasmedbio.2015.10.009.

[15] V. Nahirnyak, T. D. Mast, and C. K. Holland. "Ultrasound-Induced Thermal Elevation in Clotted Blood and Cranial Bone". In: *Ultrasound in Medicine and Biology* 33.8 (Aug. 2007), pp. 1285–1295. URL: https://doi.org/10.1016/j.ultrasmedbio.2007.02.005.

[16] R. P. Engelberger and N. Kucher. "Ultrasound-assisted thrombolysis for acute pulmonary embolism: a systematic review". In: *European Heart Journal* 35.12 (Mar. 2014), pp. 758–764. URL: https://doi.org/10.1093/eurheartj/ehu029.

[17] M. de Saint Victor, L. C. Barnsley, D. Carugo, J. Owen, C. C. Coussios, and E. Stride. "Sonothrombolysis with Magnetically Targeted Microbubbles". In: *Ultrasound in Medicine and Biology* 45.5 (May 2019), pp. 1151–1163. URL: https://doi.org/10.1016/j.ultrasmedbio.2018.12.014.

[18] P. C. Lyon, M. D. Gray, C. Mannaris, L. K. Folkes, M. Stratford, L. Campo, D. Y. Chung, S. Scott, M. Anderson, R. Goldin, R. Carlisle, F. Wu, M. R. Middleton, F. V. Gleeson, and C. C. Coussios. "Safety and feasibility of ultrasound-triggered targeted drug delivery of doxorubicin from thermosensitive liposomes in liver tumours (TARDOX): a single-centre, open-label, phase 1 trial". In: *The Lancet Oncology* 19.8 (Aug. 2018), pp. 1027–1039. URL: https://doi.org/10.1016/S1470-2045(18)30332-2.

[19] R. M. Staruch, M. Ganguly, I. F. Tannock, K. Hynynen, and R. Chopra. "Enhanced drug delivery in rabbit VX2 tumours using thermosensitive liposomes and MRI-controlled focused ultrasound hyperthermia". In: *International Journal of Hyperthermia* 28.8 (Dec. 2012), pp. 776–787. URL: http://dx.doi.org/10.3109/02656736.2012.736670.

[20] R. M. Staruch, K. Hynynen, and R. Chopra. "Hyperthermia-mediated doxorubicin release from thermosensitive liposomes using MR-HIFU: Therapeutic effect in rabbit Vx2 tumours". In: *International Journal of Hyperthermia* 31.2 (2015), pp. 118–133. URL: https://doi.org/10.3109/02656736.2014.992483.

[21] M. De Smet, E. Heijman, S. Langereis, N. M. Hijnen, and H. Grüll. "Magnetic resonance imaging of high intensity focused ultrasound mediated drug delivery from temperature-sensitive liposomes: An in vivo proof-of-concept study". In: *Journal of Controlled Release* 150.1 (Feb. 2011), pp. 102–110. URL: https://doi.org/10.1016/j.jconrel.2010.10.036.

[22] World Health Organisation. *Cancer*. URL: https://www.who.int/news-room/fact-sheets/detail/cancer (visited on June 7, 2019).

[23] Cancer Research UK. *Cancer in the UK 2019*. 2019. URL: https://www.cancerresearchuk.org/health-professional/cancer-statistics-for-the-uk (visited on July 14, 2019).

[24] D. Hanahan and R. A. Weinberg. "The hallmarks of cancer." In: *Cell* 100.1 (Jan. 2000), pp. 57–70. URL: https://doi.org/10.1016/S0092-8674(00)81683-9.

[25] D. Hanahan and R. A. Weinberg. "Hallmarks of cancer: the next generation." In: *Cell* 144.5 (Mar. 2011), pp. 646–74. URL: http://doi.org/10.1016/j.cell.2011.02.013.

[26] K. D. Miller, R. L. Siegel, C. C. Lin, A. B. Mariotto, J. L. Kramer, J. H. Rowland, K. D. Stein, R. Alteri, and A. Jemal. "Cancer treatment and survivorship statistics, 2016". In: *CA: A Cancer Journal for Clinicians* 66.4 (2016), pp. 271–289. URL: https://doi.org/10.3322/caac.21349.

[27] F. Lordick, C. Mariette, K. Haustermans, R. Obermannová, D. Arnold, and o. b. o. t. E. G. Committee. "Oesophageal cancer: ESMO Clinical Practice Guidelines for diagnosis, treatment and follow-upâ€ ". In: *Annals of Oncology* 27.suppl_5 (2016), pp. v50–v57. URL: https://doi.org/10.1093/annonc/mdw329.

[28] R. Baskar, K. A. Lee, R. Yeo, and K.-W. Yeoh. "Cancer and radiation therapy: current advances and future directions". In: *International journal of medical sciences* 9.3 (Feb. 2012), pp. 193–199. URL: https://doi.org/10.7150/ijms.3635.

[29] A. A. Wright, K. Bohlke, D. K. Armstrong, M. A. Bookman, W. A. Cliby, R. L. Coleman, D. S. Dizon, J. J. Kash, L. A. Meyer, K. N. Moore, A. B. Olawaiye, J. Oldham, R. Salani, D. Sparacio, W. P. Tew, I. Vergote, and M. I. Edelson. "Neoadjuvant chemotherapy for newly diagnosed, advanced ovarian cancer: Society of Gynecologic Oncology and American Society of Clinical Oncology Clinical Practice Guideline". In: *Gynecologic Oncology* 143.1 (Oct. 2016), pp. 3–15. URL: https://doi.org/10.1016/j.ygyno.2016.05.022.

[30] J. W. Valle, D. Palmer, R. Jackson, T. Cox, J. P. Neoptolemos, P. Ghaneh, C. L. Rawcliffe, C. Bassi, D. D. Stocken, D. Cunningham, D. O'Reilly, D. Goldstein, B. A. Robinson, C. Karapetis, A. Scarfe, F. Lacaine, J. Sand, J. R. Izbicki, J. Mayerle, C. Dervenis, A. Oláh, G. Butturini, P. A. Lind, M. R. Middleton, A. Anthoney, K. Sumpter, R. Carter, and M. W. Büchler. "Optimal Duration and Timing of Adjuvant Chemotherapy After Definitive Surgery for Ductal Adenocarcinoma of the Pancreas: Ongoing Lessons From the ESPAC-3 Study". In: *Journal of Clinical Oncology* 32.6 (2014), pp. 504–512. URL: https://doi.org/10.1200/JCO.2013.50.7657.

[31] D. A. Kunkle and R. G. Uzzo. "Cryoablation or radiofrequency ablation of the small renal mass: A meta-analysis". In: *Cancer* 113.10 (Nov. 2008), pp. 2671–2680. URL: http://doi.wiley.com/10.1002/cncr.23896.

[32] X. Yan, M. Zhang, X. Chen, W. Wei, R. Yang, Y. Yang, W. Gan, H. Guo, Y. Wang, and G.-P. Shi. "Image-guided percutaneous renal cryoablation for stage 1 renal cell carcinoma with high surgical risk". In: *World Journal of Surgical Oncology* 13.200 (2015). URL: https://doi.org/10.1186/s12957-015-0610-x.

[33] P. Saccomandi, A. Lapergola, F. Longo, E. Schena, and G. Quero. "Thermal ablation of pancreatic cancer: A systematic literature review of clinical practice and pre-clinical studies". In: *International Journal of Hyperthermia* 35.1 (2018), pp. 398–418. URL: https://doi.org/10.1080/02656736.2018.1506165.

[34] R. Scipione, M. Anzidei, A. Bazzocchi, C. Gagliardo, C. Catalano, and A. Napoli. "HIFU for Bone Metastases and other Musculoskeletal Applications". In: *Seminars in interventional radiology*. Vol. 35. 04. Thieme Medical Publishers. 2018, pp. 261–267. URL: https://doi.org/10.1055/s-0038-1673363.

[35] INSIGHTEC. *MRgFUS Treatment of Painful Bone Metastases*. URL: https://www.insightec.com/clinical/oncology (visited on June 7, 2019).

[36] E. TMS. *Alatherm HIFU*. URL: https://www.edap-tms.com/en/products-services/prostate-cancer/ablatherm-hifu (visited on Aug. 21, 2019).

[37] S. Medical. *Sonablate HIFU*. URL: https://sonacaremedical.com/surgeons/our-products/sonablate (visited on Aug. 21, 2019).

[38] INSIGHTEC. *INSIGHTEC for Women's Health*. URL: https://www.insightec.com/clinical/womens-health (visited on June 7, 2019).

[39] INSIGHTEC. *INSIGHTEC Neurosurgery*. URL: https://www.insightec.com/us/clinical/neurosurgery (visited on June 7, 2019).

[40] INSIGHTEC. *First Parkinson's Patient Treated with Insightec's Incisionless Brain Therapy*. URL: https://parkinsonsnewstoday.com/2018/05/11/first-parkinsons-patient-treated-with-insightec-ultrasound-brain-therapy/ (visited on June 7, 2019).

[41] T. Leighton. *The acoustic bubble*. Academic press, 2012.

[42] T. Muir and E. Carstensen. "Prediction of nonlinear acoustic effects at biomedical frequencies and intensities". In: *Ultrasound in Medicine & Biology* 6.4 (Jan. 1980), pp. 345–357. URL: https://doi.org/10.1016/0301-5629(80)90004-6.

[43] D. Blackstock. *Fundamentals of physical acoustics*. Wiley-Interscience, 2000.

[44] M. F. Hamilton and D. T. Blackstock. *Nonlinear acoustics*. Vol. 427. Academic press San Diego, 1998.

[45] C. Damianou and K. Hynynen. "The effect of various physical parameters on the size and shape of necrosed tissue volume during ultrasound surgery". In: *The Journal of the Acoustical Society of America* 95.3 (1994), pp. 1641–1649. URL: https://doi.org/10.1121/1.408550.

[46] L. A. Frizzell. "Threshold dosages for damage to mammalian liver by high intensity focused ultrasound". In: *IEEE Transactions on Ultrasonics, Ferroelectrics, and Frequency Control* 35.5 (1988), pp. 578–581. URL: https://doi.org/10.1109/58.8036.

[47] F. J. Fry, G. Kossoff, R. C. Eggleton, and F. Dunn. "Threshold Ultrasonic Dosages for Structural Changes in the Mammalian Brain". In: *The Journal of the Acoustical Society of America* 48.6B (1970), pp. 1413–1417. URL: https://doi.org/10.1121/1.1912301.

[48] K. Hynynen. "The threshold for thermally significant cavitation in dog's thigh muscle in vivo." In: *Ultrasound in medicine & biology* 17.2 (1991), pp. 157–169. URL: https://doi.org/10.1016/0301-5629(91)90123-e.

[49] R. G. Holt and R. A. Roy. "Measurements of bubble-enhanced heating from focused, MHz-frequency ultrasound in a tissue-mimicking material". In: *Ultrasound in Medicine and Biology* 27.10 (Oct. 2001), pp. 1399–1412. URL: https://doi.org/10.1016/S0301-5629(01)00438-0.

[50] J. E. Kennedy. "High-intensity focused ultrasound in the treatment of solid tumours". In: *Nat Rev Cancer* 5 (2005). URL: http://dx.doi.org/10.1038/nrc1591.

[51] C. C. Coussios and R. A. Roy. "Applications of Acoustics and Cavitation to Noninvasive Therapy and Drug Delivery". In: *Annual Review of Fluid Mechanics* 40.1 (2008), pp. 395–420. URL: https://doi.org/10.1146/annurev.fluid.40.111406.102116.

[52] N. Ellens and K. Hynynen. "Frequency considerations for deep ablation with high-intensity focused ultrasound: A simulation study". In: *Medical Physics* 42.8 (July 2015), pp. 4896–4910. URL: http://doi.wiley.com/10.1118/1.4927060.

[53] V. A. Khokhlova, M. R. Bailey, J. A. Reed, B. W. Cunitz, P. J. Kaczkowski, and L. A. Crum. "Effects of nonlinear propagation, cavitation, and boiling in lesion formation by high intensity focused ultrasound in a gel phantom". In: *The Journal of the Acoustical Society of America* 119.3 (2006), pp. 1834–1848. URL: https://doi.org/10.1121/1.2161440.

[54] C. C. Coussios, C. H. Farny, G. T. Haar, and R. A. Roy. "Role of acoustic cavitation in the delivery and monitoring of cancer treatment by high-intensity focused ultrasound (HIFU)." In: *International journal of hyperthermia : the official journal of European Society for Hyperthermic Oncology, North American Hyperthermia Group* 23.2 (Mar. 2007), pp. 105–120. URL: https://doi.org/10.1080/02656730701194131.

[55] C. H. Farny, R. G. Holt, and R. A. Roy. "Temporal and Spatial Detection of HIFU-Induced Inertial and Hot-Vapor Cavitation with a Diagnostic Ultrasound System". In: *Ultrasound in Medicine and Biology* 35.4 (Apr. 2009), pp. 603–615. URL: https://doi.org/10.1016/j.ultrasmedbio.2008.09.025.

[56] J. Kolb and W. L. Nyborg. "Small-Scale Acoustic Streaming in Liquids". In: *The Journal of the Acoustical Society of America* 28.6 (Nov. 1956), pp. 1237–1242. URL: https://doi.org/10.1121/1.1908603.

[57] C. H. Farny, R. Glynn Holt, and R. A. Roy. "The Correlation Between Bubble-Enhanced HIFU Heating and Cavitation Power". In: *IEEE Transactions on Biomedical Engineering* 57.1 (Jan. 2010), pp. 175–184. URL: https://doi.org/10.1109/TBME.2009.2028133.

[58] E. M. Zilonova, M. Solovchuk, and T. W. Sheu. "Simulation of cavitation enhanced temperature elevation in a soft tissue during high-intensity focused ultrasound thermal therapy". In: *Ultrasonics Sonochemistry* 53 (May 2019), pp. 11–24. URL: https://doi.org/10.1016/j.ultsonch.2018.12.006.

[59] E. Beguin, S. Shrivastava, N. V. Dezhkunov, A. P. McHale, J. F. Callan, and E. Stride. "Direct Evidence of Multibubble Sonoluminescence Using Therapeutic Ultrasound and Microbubbles". In: *ACS Applied Materials & Interfaces* 11.22 (June 2019), pp. 19913–19919. URL: https://doi.org/10.1021/acsami.9b07084.

[60] A. Schroeder, J. Kost, and Y. Barenholz. "Ultrasound, liposomes, and drug delivery: principles for using ultrasound to control the release of drugs from liposomes". In: *Chemistry and Physics of Lipids* 162.1-2 (Nov. 2009), pp. 1–16. URL: https://doi.org/10.1016/j.chemphyslip.2009.08.003.

[61] S. Meairs. "Facilitation of Drug Transport across the Blood-Brain Barrier with Ultrasound and Microbubbles". eng. In: *Pharmaceutics* 7.3 (Aug. 2015), pp. 275–293. URL: https://doi.org/10.3390/pharmaceutics7030275.

[62] M. R. Bailey, R. O. Cleveland, T. Colonius, L. A. Crum, A. P. Evan, J. E. Lingeman, J. A. McAteer, O. A. Sapozhnikov, and J. C. Williams. "Cavitation in shock wave lithotripsy: the critical role of bubble activity in stone breakage and kidney trauma". In: *IEEE Symposium on Ultrasonics, 2003.* Vol. 1. Oct. 2003, pp. 724–727. URL: https://doi.org/10.1109/ULTSYM.2003.1293503.

[63] Y. A. Pishchalnikov, J. A. McAteer, J. C. Williams, I. V. Pishchalnikova, and R. J. Vonderhaar. "Why Stones Break Better at Slow Shockwave Rates Than at Fast Rates: In Vitro Study with a Research Electrohydraulic Lithotripter". In: *Journal of Endourology* 20.8 (2006), pp. 537–541. URL: https://doi.org/10.1089/end.2006.20.537.

[64] N. Sanghvi, F. Fry, R. Bihrle, R. Foster, M. Phillips, J. Syrus, A. Zaitsev, and C. Hennige. "Microbubbles during tissue treatment using high intensity focused ultrasound". In: *1995 IEEE Ultrasonics Symposium. Proceedings. An International Symposium*. Vol. 2. IEEE, 1995, pp. 1571–1574. URL: https://doi.org/10.1109/ULTSYM.1995.495855.

[65] G. Maimbourg, A. Houdouin, T. Deffieux, M. Tanter, and J. F. Aubry. "3D-printed adaptive acoustic lens as a disruptive technology for transcranial ultrasound therapy using single-element transducers". In: *Physics in Medicine and Biology* 63.2 (Jan. 2018), p. 025026. URL: http://doi.org/10.1088/1361-6560/aaa037.

[66] F. Wu, Z. B. Wang, W. Z. Chen, W. Wang, Y. Gui, M. Zhang, G. Zheng, Y. Zhou, G. Xu, M. Li, C. Zhang, H. Ye, and R. Feng. "Extracorporeal high intensity focused ultrasound ablation in the treatment of 1038 patients with solid carcinomas in China: An overview". In: *Ultrasonics Sonochemistry*. Vol. 11. 3-4. May 2004, pp. 149–154. URL: https://doi.org/10.1016/j.ultsonch.2004.01.011.

[67] J. F. Aubry, M. Pernot, F. Marquet, M. Tanter, and M. Fink. "Transcostal high-intensity-focused ultrasound: Ex vivo adaptive focusing feasibility study". In: *Physics in Medicine and Biology* 53.11 (June 2008), pp. 2937–2951. URL: https://doi.org/10.1088/0031-9155/53/11/012.

[68] D. A. Carpenter, G. Kossoff, and K. A. Griffiths. "Correction of distortion in US images caused by subcutaneous tissues: results in tissue phantoms and human subjects." In: *Radiology* 195.2 (1995), pp. 563–567. URL: https://doi.org/10.1148/radiology.195.2.7724784.

[69] G. Kossoff, K. A. Griffiths, and C. E. Dixon. "Is the quality of transvaginal images superior to transabdominal ones under matched conditions?" In: *Ultrasound in Obstetrics and Gynecology* 1.1 (1991), pp. 29–35. URL: https://doi.org/10.1046/j.1469-0705.1991.01010029.x.

[70] M. O'Donnell and S. W. Flax. "Phase-aberration correction using signals from point reflectors and diffuse scatterers: measurements". In: *IEEE Transactions on Ultrasonics, Ferroelectrics, and Frequency Control* 35.6 (Nov. 1988), pp. 768–774. URL: https://doi.org/10.1109/58.9334.

[71] X. Fan and K. Hynynen. "The effect of wave reflection and refraction at soft tissue interfaces during ultrasound hyperthermia treatments". In: *The Journal of the Acoustical Society of America* 91.3 (Mar. 1992), pp. 1727–1736. URL: http://dx.doi.org/10.1121/1.402452.

[72] H.-L. Liu, N. McDannold, and K. Hynynen. "Focal beam distortion and treatment planning in abdominal focused ultrasound surgery". In: *Medical Physics* 32.5 (May 2005), pp. 1270–1280. URL: http://dx.doi.org/10.1118/1.1895525.

[73] R. Ritchie, J. Collin, C. Coussios, and T. Leslie. "Attenuation and De-focusing During High-Intensity Focused Ultrasound Therapy Through Peri-nephric Fat". In: *Ultrasound in Medicine and Biology* 39.10 (Oct. 2013), pp. 1785–1793. URL: https://doi.org/10.1016/j.ultrasmedbio.2013.04.010.

[74] R. W. Ritchie, T. A. Leslie, G. D. H. Turner, I. S. D. Roberts, L. D'Urso, D. Collura, A. Demarchi, G. Muto, and M. E. Sullivan. "Laparoscopic high-intensity focused ultrasound for renal tumours: A proof of concept study". In: *BJU International* 107.8 (Apr. 2011), pp. 1290–1296. URL: http://doi.wiley.com/10.1111/j.1464-410X.2010.09620.x.

[75] R. W. Ritchie. "Improving clinical outcomes in High Intensity Focused Ultrasound [DPhil]". PhD thesis. University of Oxford, 2012. URL: http://www.ora.ox.ac.uk/.

[76] T. Leslie, R. Ritchie, R. Illing, G. Ter Haar, R. Phillips, M. Middleton, F. Wu, and D. Cranston. "High-intensity focused ultrasound treatment of liver tumours: Post-treatment MRI correlates well with intra-operative estimates of treatment volume". In: *British Journal of Radiology* 85.1018 (Oct. 2012), pp. 1363–1370. URL: https://doi.org/10.1259/bjr/56737365.

[77] Focused Ultrasound Foundation. *Diseases and Conditions: Overview.* URL: https://www.fusfoundation.org/diseases-and-conditions-all/overview (visited on June 2, 2019).

[78] J. Luo, X. Ren, and T. Yu. "Efficacy of extracorporeal ultrasound-guided high intensity focused ultrasound: An evaluation based on controlled trials in China". In: *International Journal of Radiation Biology* 91.6 (June 2015), pp. 480–485. URL: http://dx.doi.org/10.3109/09553002.2015.1021962.

[79] E. Maloney and J. H. Hwang. *Emerging HIFU applications in cancer therapy.* 2015. URL: https://doi.org/10.3109/02656736.2014.969789.

[80] F. Wu, Z.-B. Wang, W.-Z. Chen, H. Zhu, J. Bai, J.-Z. Zou, K.-Q. Li, C.-B. Jin, F.-L. Xie, and H.-B. Su. "Extracorporeal High Intensity Focused Ultrasound Ablation in the Treatment of Patients with Large Hepatocellular Carcinoma". In: *Annals of Surgical Oncology* 11.12 (Dec. 2004), pp. 1061–1069. URL: https://doi.org/10.1245/ASO.2004.02.026.

[81] J. Kim, D. J. Chung, S. E. Jung, S. H. Cho, S. T. Hahn, and J. M. Lee. "Therapeutic effect of high-intensity focused ultrasound combined with transarterial chemoembolisation for hepatocellular carcinoma <5 cm: Comparison with transarterial chemoembolisation monotherapy - Preliminary observations". In: *British Journal of Radiology* 85.1018 (Oct. 2012), e940–e946. URL: https://doi.org/10.1259/bjr/32750755.

[82] T. A. Leslie, J. E. Kennedy, R. O. Illing, G. R. ter Haar, F. Wu, R. R. Phillips, P. J. Friend, I. S. D. Roberts, D. W. Cranston, and M. R. Middleton. "High-intensity focused ultrasound ablation of liver tumours: can radiological assessment predict the histological response?" In: *The British Journal of Radiology* 81.967 (2008), pp. 564–571. URL: https://doi.org/10.1259/bjr/27118953.

[83] K. S. H. Chok, T. T. Cheung, R. C. L. Lo, F. S. K. Chu, S. H. Y. Tsang, A. C. Y. Chan, W. W. Sharr, J. Y. Y. Fung, W. C. Dai, S. C. Chan, S. T. Fan, and C. M. Lo. "Pilot study of high-intensity focused ultrasound ablation as a bridging therapy for hepatocellular carcinoma patients wait-listed for liver transplantation." In: *Liver transplantation : official publication of the American Association for the Study of Liver Diseases and the International Liver Transplantation Society* 20.8 (Aug. 2014), pp. 912–921. URL: https://doi.org/10.1002/lt.23892.

[84] M. Rabjerg, M. N. Mikkelsen, S. Walter, and N. Marcussen. "Incidental renal neoplasms: is there a need for routine screening? A Danish single-center epidemiological study". In: *APMIS* 122.8 (2014), pp. 708–714. URL: https://doi.org/10.1111/apm.12282.

[85] M. Jayson and H. Sanders. "Increased incidence of serendipitously discovered renal cell carcinoma." In: *Urology* 51.2 (Feb. 1998), pp. 203–205. URL: https://doi.org/10.1016/S0090-4295(97)00506-2.

[86] C. J. Kane, K. Mallin, J. Ritchey, M. R. Cooperberg, and P. R. Carroll. "Renal cell cancer stage migration: analysis of the National Cancer Data Base." In: *Cancer* 113.1 (July 2008), pp. 78–83. URL: https://doi.org/10.1002/cncr.23518.

[87] R. Heuer, I. S. Gill, G. Guazzoni, Z. Kirkali, M. Marberger, J. P. Richie, and J. J. M. C. H. de la Rosette. "A critical analysis of the actual role of minimally invasive surgery and active surveillance for kidney cancer." In: *European urology* 57.2 (Feb. 2010), pp. 223–232. URL: https://doi.org/10.1016/j.eururo.2009.10.023.

[88] B. Escudier, C. Porta, M. Schmidinger, N. Rioux-Leclercq, A. Bex, V. Khoo, V. Grünwald, S. Gillessen, A. Horwich, and E. G. Committee. "Renal cell carcinoma: ESMO Clinical Practice Guidelines for diagnosis, treatment and follow-up†". In: *Annals of Oncology* 30.5 (Feb. 2019), pp. 706–720. URL: https://doi.org/10.1093/annonc/mdz056.

[89] S. E. Abboud, T. Patel, S. Soriano, J. Giesler, N. Alvarado, and P. Kang. "Long-Term Clinical Outcomes Following Radiofrequency and Microwave Ablation of Renal Cell Carcinoma at a Single VA Medical Center". In: *Current Problems in Diagnostic Radiology* 47.2 (Mar. 2018), pp. 98–102. URL: https://www.sciencedirect.com/science/article/pii/S0363018816301554.

[90] J. D. Iannuccilli, D. E. Dupuy, M. D. Beland, J. T. Machan, D. J. Golijanin, and W. W. Mayo-Smith. "Effectiveness and safety of computed tomography-guided radiofrequency ablation of renal cancer: a 14-year single institution experience in 203 patients". In: *European Radiology* 26.6 (2016), pp. 1656–1664. URL: https://doi.org/10.1007/s00330-015-4006-7.

[91] F. Wu, Z.-B. Wang, W.-Z. Chen, J. Bai, H. Zhu, and T.-Y. Qiao. "Preliminary Experience Using High Intensity Focused Ultrasound for the Treatment of Patients With Advanced Stage Renal Malignancy". In: *The Journal of Urology* 170.6 (Dec. 2003), pp. 2237–2240. URL: https://doi.org/10.1097/01.ju.0000097123.34790.70.

[92] R. O. Illing, J. E. Kennedy, F. Wu, G. R. ter Haar, A. S. Protheroe, P. J. Friend, F. V. Gleeson, D. W. Cranston, R. R. Phillips, and M. R. Middleton. "The safety and feasibility of extracorporeal high-intensity focused ultrasound (HIFU) for the treatment of liver and kidney tumours in a Western population." In: *British journal of cancer* 93.8 (Oct. 2005), pp. 890–895. URL: https://doi.org/10.1038/sj.bjc.6602803.

[93] D. Cranston. "A review of High intensity focused ultrasound in relation to the treatment of renal tumors and other malignancies". In: *Ultrasonics Sonochemistry* 27 (May 2015), pp. 654–658. URL: https://doi.org/10.1016/j.ultsonch.2015.05.035.

[94] X. Fan and K. Hynynen. "Ultrasound surgery using multiple sonications - Treatment time considerations". In: *Ultrasound in Medicine and Biology* 22.4 (Jan. 1996), pp. 471–482. URL: https://doi.org/10.1016/0301-5629(96)00026-9.

[95] T. D. Mast, L. M. Hinkelman, M. J. Orr, V. W. Sparrow, and R. C. Waag. "Simulation of ultrasonic pulse propagation through the abdominal wall". In: *The Journal of the Acoustical Society of America* 102.2 (1997), pp. 1177–1190. URL: https://doi.org/10.1121/1.421015.

[96] R. J. McGough, M. L. Kessler, E. S. Ebbini, and C. A. Cain. "Treatment planning for hyperthermia with ultrasound phased arrays". In: *IEEE Transactions on Ultrasonics, Ferroelectrics, and Frequency Control* 43.6 (1996), pp. 1074–1084. URL: https://doi.org/10.1109/58.542051.

[97] R. J. McGough, E. S. Ebbini, and C. A. Cain. "Direct computation of ultrasound phased-array driving signals from a specified temperature distribution for hyperthermia". In: *IEEE Transactions on Biomedical Engineering* 39.8 (Aug. 1992), pp. 825–835. URL: https://doi.org/10.1109/10.148390.

[98] P. J. White, B. Andre, N. McDannold, and G. T. Clement. "A pre-treatment planning strategy for high-intensity focused ultrasound (HIFU) treatments". In: *2008 IEEE Ultrasonics Symposium*. 2008, pp. 2056–2058. URL: https://doi.org/10.1109/ULTSYM.2008.0507.

[99] M. M. Paulides, P. R. Stauffer, E. Neufeld, P. F. Maccarini, A. Kyriakou, R. A. Canters, C. J. Diederich, J. F.Bakker, and G. C. V. Rhoon. "Simulation techniques in hyperthermia treatment planning". In: *Int J Hyperth* 29.4 (2013), pp. 346–357. URL: http://dx.doi.org/10.3109/02656736.2013.790092.

[100] V. Suomi, J. Jaros, B. Treeby, and R. Cleveland. "Full Modelling of High-Intensity Focused Ultrasound and Thermal Heating in the Kidney using Realistic Patient Models". In: *IEEE Transactions on Biomedical Engineering* 65.5 (July 2018), pp. 969–979. URL: https://doi.org/10.1109/TBME.2017.2732684.

[101] M. D. Gray, P. C. Lyon, C. Mannaris, L. K. Folkes, M. Stratford, L. Campo, D. Y. F. Chung, S. Scott, M. Anderson, R. Goldin, R. Carlisle, F. Wu, M. R. Middleton, F. V. Gleeson, and C. C. Coussios. "Focused Ultrasound Hyperthermia for Targeted Drug Release from Thermosensitive Liposomes: Results from a Phase I Trial". In: *Radiology* 291.1 (2019), pp. 232–238. URL: https://doi.org/10.1148/radiol.2018181445.

[102] A. Grisey, M. Heidmann, V. Letort, P. Lafitte, and S. Yon. "Influence of Skin and Subcutaneous Tissue on High-Intensity Focused Ultrasound Beam: Experimental Quantification and Numerical Modeling". In: *Ultrasound in Medicine and Biology* 42.10 (Oct. 2016), pp. 2457–2465. URL: https://doi.org/10.1016/j.ultrasmedbio.2016.06.013.

[103] B. E. Treeby and B. T. Cox. "k-Wave: MATLAB toolbox for the simulation and reconstruction of photoacoustic wave fields." In: *Journal of biomedical optics* 15.2 (2010).

[104] B. E. Treeby, J. Jaros, A. P. Rendell, and B. T. Cox. "Modeling nonlinear ultrasound propagation in heterogeneous media with power law absorption using a k-space pseudospectral method". In: *The Journal of the Acoustical Society of America* 131.6 (June 2012), pp. 4324–4336. URL: http://dx.doi.org/10.1121/1.4712021.

[105] B. E. Treeby and B. T. Cox. "Modeling power law absorption and dispersion for acoustic propagation using the fractional Laplacian". In: *The Journal of the Acoustical Society of America* 127.5 (May 2010), pp. 2741–2748. URL: http://dx.doi.org/10.1121/1.3377056.

[106] B. Treeby, B. Cox, and J. Jaros. *K-Wave, a MATLAB toolbox for the time-domain simulation of acoustic wave fields*. 2012.

[107] M. Tabei, T. D. Mast, and R. C. Waag. "A k-space method for coupled first-order acoustic propagation equations". In: *The Journal of the Acoustical Society of America* 111.1 (Jan. 2002), pp. 53–63. URL: http://dx.doi.org/10.1121/1.1421344.

[108] J. L. Robertson, B. T. Cox, and B. E. Treeby. "Quantifying numerical errors in the simulation of transcranial ultrasound using pseudospectral methods". In: *Ultrasonics Symposium (IUS), 2014 IEEE International*. IEEE. 2014, pp. 2000–2003. URL: https://doi.org/10.1109/ULTSYM.2014.0498.

[109] E. Martin, Y. T. Ling, and B. E. Treeby. "Simulating Focused Ultrasound Transducers Using Discrete Sources on Regular Cartesian Grids". In: *IEEE Transactions on Ultrasonics, Ferroelectrics, and Frequency Control* 63.10 (Aug. 2016), pp. 1535–1542. URL: https://doi.org/10.1109/TUFFC.2016.2600862.

[110] J. L. B. Robertson, B. T. Cox, J. Jaros, and B. E. Treeby. "Accurate simulation of transcranial ultrasound propagation for ultrasonic neuromodulation and stimulation." In: *The Journal of the Acoustical Society of America* 141.3 (Mar. 2017), pp. 1726–1736. URL: http://dx.doi.org/10.1121/1.4976339.

[111] T. D. Mast. "Empirical relationships between acoustic parameters in human soft tissues". In: *Acoustics Research Letters Online* 1.2 (Oct. 2000), pp. 37–42. URL: http://dx.doi.org/10.1121/1.1336896.

[112] J. Jaros, A. P. Rendell, and B. E. Treeby. "Full-wave nonlinear ultrasound simulation on distributed clusters with applications in high-intensity focused ultrasound". In: *International Journal of High Performance Computing Applications* 30.2 (Aug. 2015), pp. 137–155. arXiv: arXiv:1408.4675v1. URL: https://doi.org/10.1177/1094342015581024.

[113] H. T. O'Neil. "Theory of Focusing Radiators". In: *The Journal of the Acoustical Society of America* 21.5 (Sept. 1949), pp. 516–526. URL: http://dx.doi.org/10.1121/1.1906542.

[114] H. H. Pennes. "Analysis of tissue and arterial blood temperatures in the resting human forearm". In: *J Appl Physiol* 1 (1948). URL: https://doi.org/10.1152/jappl.1948.1.2.93.

[115] F. A. Duck. "Chapter 4 – Acoustic Properties of Tissue at Ultrasonic Frequencies". In: *Physical Properties of Tissues-A Comprehensive Reference Book. San Diego, CA: Academic* (1990), pp. 73–135.

[116] S. A. Sapareto and W. C. Dewey. “Thermal dose determination in cancer therapy”. In: *International Journal of Radiation Oncology • Biology • Physics* 10.6 (June 1984), pp. 787–800. URL: http://dx.doi.org/10.1016/0360-3016(84)90379-1.

[117] M. W. Dewhirst, B. L. Viglianti, M. Lora-Michiels, M. Hanson, and P. J. Hoopes. “Basic principles of thermal dosimetry and thermal thresholds for tissue damage from hyperthermia”. In: *International Journal of Hyperthermia* 19.3 (Jan. 2003), pp. 267–294. URL: https://doi.org/10.1080/0265673031000119006.

[118] J. D. Maynard, E. G. Williams, and Y. Lee. “Nearfield acoustic holography: I. Theory of generalized holography and the development of NAH”. In: *The Journal of the Acoustical Society of America* 78.4 (Oct. 1985), pp. 1395–1413. URL: http://dx.doi.org/10.1121/1.392911.

[119] O. A. Sapozhnikov, S. A. Tsysar, V. A. Khokhlova, and W. Kreider. “Acoustic holography as a metrological tool for characterizing medical ultrasound sources and fields”. In: *The Journal of the Acoustical Society of America* 138.3 (Sept. 2015), pp. 1515–1532. URL: http://dx.doi.org/10.1121/1.4928396.

[120] J. Blackmore, R. O. Cleveland, and J. Mobley. “Spatial filters suppress ripple artifacts in the computation of acoustic fields with the angular spectrum method”. In: *The Journal of the Acoustical Society of America* 144.5 (2018), pp. 2947–2951. URL: https://doi.org/10.1121/1.5079637.

[121] D. P. Orofino and P. C. Pedersen. “Efficient angular spectrum decomposition of acoustic sources. I. Theory”. In: *IEEE Transactions on Ultrasonics, Ferroelectrics, and Frequency Control* 40.3 (May 1993), pp. 238–249. URL: https://doi.org/10.1109/58.216837.

[122] P. Wu, R. Kazys, and T. Stepinski. “Analysis of the numerically implemented angular spectrum approach based on the evaluation of two-dimensional acoustic fields. Part II. Characteristics as a function of angular range”. In: *The Journal of the Acoustical Society of America* 99.3 (Mar. 1996), pp. 1349–1359. URL: https://doi.org/10.1121/1.414713.

[123] B. Treeby, F. Lucka, E. Martin, and B. T. Cox. “Equivalent-Source Acoustic Holography for Projecting Measured Ultrasound Fields Through Complex Media”. In: *IEEE Transactions on Ultrasonics, Ferroelectrics, and Frequency Control* 65.10 (Oct. 2018), pp. 1857–1864. URL: https://doi.org/10.1109/TUFFC.2018.2861895.

[124] V. A. Del Grosso and C. W. Mader. “Speed of Sound in Pure Water”. In: *The Journal of the Acoustical Society of America* 52.5B (1972), pp. 1442–1446. URL: https://doi.org/10.1121/1.1913258.

[125] K. A. Wear, C. Baker, and P. Miloro. “Directivity and Frequency-Dependent Effective Sensitive Element Size of Needle Hydrophones: Predictions From Four Theoretical Forms Compared With Measurements”. eng. In: *IEEE transactions on ultrasonics, ferroelectrics, and frequency control* 65.10 (Oct. 2018), pp. 1781–1788. URL: https://www.ncbi.nlm.nih.gov/pubmed/30010557%20https://www.ncbi.nlm.nih.gov/pmc/articles/PMC6175646/.

[126] S. Zhang, X. Li, H. Jeong, S. Cho, and H. Hu. "Theoretical and experimental investigation of the pulse-echo nonlinearity acoustic sound fields of focused transducers". In: *Applied Acoustics* 117 (2016).

[127] F. Dunn. "Attenuation and speed of ultrasound in lung: Dependence upon frequency and inflation". In: *The Journal of the Acoustical Society of America* 80.4 (1986), pp. 1248–1250. URL: https://doi.org/10.1121/1.393818.

[128] Y.-F. Zhou. "High intensity focused ultrasound in clinical tumor ablation". In: *World journal of clinical oncology* 2.1 (Jan. 2011), pp. 8–27. URL: https://doi.org/10.5306/wjco.v2.i1.8.

[129] P. Gélat, G. Ter Haar, and N. Saffari. "Modelling of the acoustic field of a multi-element HIFU array scattered by human ribs". In: *Physics in Medicine and Biology* 56.17 (Sept. 2011), pp. 5553–5581. URL: http://doi.org/10.1088/0031-9155/56/17/007.

[130] H. F. Bowman. "Heat transfer and thermal dosimetry". In: *Journal of Microwave Power* 16.2 (Jan. 1981), pp. 121–133. URL: https://doi.org/10.1080/16070658.1981.11689231.

[131] H. P. Kok and J. Crezee. "A comparison of the heating characteristics of capacitive and radiative superficial hyperthermia". In: *International Journal of Hyperthermia* 33.4 (2017), pp. 378–386. URL: https://doi.org/10.1080/02656736.2016.1268726.

[132] J. Lagendijk, J. Hand, P. van den Berg, J. Anderson, F. Bardati, N. Uzunoglu, R. Sheppard, and J. Bolomey. *Treatment planning and modelling in hyperthermia: A task group report of the European Society for Hyperthermic Oncology.* 1992.

[133] H.-L. M. Cheng and D. B. Plewes. "Tissue thermal conductivity by magnetic resonance thermometry and focused ultrasound heating". In: *Journal of Magnetic Resonance Imaging: An Official Journal of the International Society for Magnetic Resonance in Medicine* 16.5 (2002), pp. 598–609. URL: https://doi.org/10.1002/jmri.10199.

[134] H. J. Feldmann, M. Molls, A. Hoederath, S. Krümpelmann, and H. Sack. "Blood flow and steady state temperatures in deep-seated tumors and normal tissues". In: *International Journal of Radiation Oncology, Biology, Physics* 23.5 (Jan. 1992), pp. 1003–1008. URL: https://doi.org/10.1016/0360-3016(92)90906-X.

[135] L. R. Williams and R. W. Leggett. *Reference values for resting blood flow to organs of man.* Aug. 1989. URL: http://doi.org/10.1088/0143-0815/10/3/001.

[136] NCRP. *Report No. 113: Exposure criteria for medical diagnostic ultrasound: I. Criteria based on thermal mechanisms.* Tech. rep. National Council on Thermal Protection and Measurements, Bethesda, MD, USA, 1992.

[137] A. Grisey, S. Yon, V. Letort, and P. Lafitte. "Simulation of high-intensity focused ultrasound lesions in presence of boiling". In: *Journal of Therapeutic Ultrasound* 4.1 (2016), pp. 1–14. URL: http://dx.doi.org/10.1186/s40349-016-0056-9.

[138] F. Chavrier, J. Y. Chapelon, A. Gelet, and D. Cathignol. "Modeling of high-intensity focused ultrasound-induced lesions in the presence of cavitation bubbles". In: *The Journal of the Acoustical Society of America* 108.1 (2000), pp. 432–440. URL: https://doi.org/10.1121/1.429476.

[139] J. Blackmore. "Focused ultrasound: a non-invasive brain stimulation modality [DPhil]". PhD thesis. University of Oxford, 2018.

[140] P. Gélat, G. ter Haar, and N. Saffari. "The optimization of acoustic fields for ablative therapies of tumours in the upper abdomen". In: *Physics in Medicine & Biology* 57.24 (2012), p. 8471. URL: http://stacks.iop.org/0031-9155/57/i=24/a=8471.

[141] X. Fan and K. Hynynen. "The effects of curved tissue layers on the power deposition patterns of therapeutic ultrasound beams." In: *Medical physics* 21.1 (Jan. 1994), pp. 25–34. URL: https://doi.org/10.1118/1.597250.

[142] M. Fink. "Time reversed acoustics". In: *Physics Today* 50.3 (Mar. 1997), pp. 34–40. URL: http://physicstoday.scitation.org/doi/10.1063/1.881692.

[143] D. H. Turnbull, S. R. Wilson, A. L. Hine, and F. S. Foster. "Ultrasonic characterization of selected renal tissues". In: *Ultrasound in Medicine and Biology* 15.3 (Jan. 1989), pp. 241–253. URL: https://doi.org/10.1016/0301-5629(89)90068-9.

[144] R. L. Errabolu, C. M. Sehgal, R. C. Bahn, and J. F. Greenleaf. "Measurement of ultrasonic nonlinear parameter in excised fat tissues". In: *Ultrasound in Medicine and Biology* 14.2 (Jan. 1988), pp. 137–146. URL: https://doi.org/10.1016/0301-5629(88)90181-0.

[145] S. A. Goss, R. L. Johnston, and F. Dunn. "Comprehensive compilation of empirical ultrasonic properties of mammalian tissues". In: *The Journal of the Acoustical Society of America* 64.2 (1978), pp. 423–457. URL: https://doi.org/10.1121/1.382016.

[146] G. D. Ludwig and F. W. Struthers. *Considerations underlying the use of ultrasound to detect gallstones and foreign bodies in tissue*. Tech. rep. NAVAL MEDICAL RESEARCH INST BETHESDA MD, 1949.

[147] F. J. Fry and J. E. Barger. "Acoustical properties of the human skull". In: *The Journal of the Acoustical Society of America* 63.5 (1978), pp. 1576–1590. URL: https://doi.org/10.1121/1.381852.

[148] D. E. Goldman and J. R. Richards. "Measurement of High-Frequency Sound Velocity in Mammalian Soft Tissues". In: *The Journal of the Acoustical Society of America* 26.6 (1954), pp. 981–983. URL: https://doi.org/10.1121/1.1907465.

[149] J.-F. Aubry, M. Tanter, M. Pernot, J.-L. Thomas, and M. Fink. "Experimental demonstration of noninvasive transskull adaptive focusing based on prior computed tomography scans". In: *The Journal of the Acoustical Society of America* 113.1 (2003), pp. 84–93. URL: https://doi.org/10.1121/1.1529663.

[150] D. Fontanarosa, S. van der Meer, E. Harris, and F. Verhaegen. "A CT based correction method for speed of sound aberration for ultrasound based image guided radiotherapy". In: *Medical Physics* 38.5 (2011), pp. 2665–2673. URL: https://aapm.onlinelibrary.wiley.com/doi/abs/10.1118/1.3583475.

[151] L. M. Hinkelman, T. D. Mast, L. A. Metlay, and R. C. Waag. "The effect of abdominal wall morphology on ultrasonic pulse distortion. Part I. Measurements". In: *The Journal of the Acoustical Society of America* 104.6 (Nov. 1998), pp. 3635–3649. URL: http://dx.doi.org/10.1121/1.423946.

[152] Y. Wang, G. Morrell, M. E. Heibrun, A. Payne, and D. L. Parker. "3D Multi-parametric Breast MRI Segmentation Using Hierarchical Support Vector Machine with Coil Sensitivity Correction". In: *Academic Radiology* 20.2 (Feb. 2013), pp. 137–147. URL: https://doi.org/10.1016/j.acra.2012.08.016.

[153] O. D. Leinhard, A. Johansson, J. Rydell, O. Smedby, F. Nystrom, P. Lundberg, and M. Borga. "Quantitative abdominal fat estimation using MRI". In: *2008 19th International Conference on Pattern Recognition*. Dec. 2008, pp. 1–4. URL: https://doi.org/10.1109/ICPR.2008.4761764.

[154] S. Hadjidemetriou, U. Ludwig, J. Hennig, and M. Buechert. "Analysis of abdominal fat tissue images acquired with continuously moving table MRI". In: *2012 9th IEEE International Symposium on Biomedical Imaging (ISBI)*. May 2012, pp. 1244–1247. URL: https://doi.org/10.1109/ISBI.2012.6235787.

[155] J. Linge, M. Borga, J. West, T. Tuthill, M. R. Miller, A. Dumitriu, E. L. Thomas, T. Romu, P. Tunón, J. D. Bell, and O. Dahlqvist Leinhard. "Body Composition Profiling in the UK Biobank Imaging Study". In: *Obesity* 26.11 (2018), pp. 1785–1795. URL: https://doi.org/10.1002/oby.22210.

[156] E. Ferrante and N. Paragios. "Slice-to-volume medical image registration: A survey". In: *Medical Image Analysis* 39 (July 2017), pp. 101–123. URL: https://doi.org/10.1016/j.media.2017.04.010.

[157] E. Ferrante and N. Paragios. "Graph-Based Slice-to-Volume Deformable Registration". In: *International Journal of Computer Vision* 126.1 (Jan. 2018), pp. 36–58. URL: https://doi.org/10.1007/s11263-017-1040-8.

[158] C. Mougenot, M. Tillander, J. Koskela, M. O. Köhler, C. Moonen, and M. Ries. "High intensity focused ultrasound with large aperture transducers: a MRI based focal point correction for tissue heterogeneity". In: *Medical physics* 39.4 (2012), pp. 1936–1945. URL: https://doi.org/10.1118/1.3693051.

[159] E. Martin, J. Jaros, and B. E. Treeby. "Experimental Validation of k-Wave: Nonlinear Wave Propagation in Layered, Absorbing Fluid Media". In: *IEEE Transactions on Ultrasonics, Ferroelectrics, and Frequency Control* 67.1 (2020), pp. 81–91. URL: https://doi.org/10.1109/TUFFC.2019.2941795.